

Turbidity Currents in Reservoirs

水庫異重流模擬與分析-以石門水庫為例

Master of Science Thesis
A.S. (Alwin) Commandeur
26th of June, 2015

Turbidity Currents in Reservoirs

by

ALWIN SEBASTIAAN COMMANDEUR

26th of June, 2015

in partial fulfilment of the requirements for the degree of

MASTER OF SCIENCE

in Civil Engineering.

DELFT UNIVERSITY OF TECHNOLOGY
Faculty of Civil Engineering and Geosciences
Department of Hydraulic Engineering

GRADUATION COMMITTEE

Prof. dr. ir. J. C. (Han) WINTERWERP	Delft University of Technology, chairman
Dr. ir. C. J. (Kees) SLOFF	Deltares & Delft University of Technology, daily supervisor
Dr. ir. M. M. (Martine) RUTTEN	Delft University of Technology, second reviewer
Prof. dr. J.C. (Jinn-Chuang) YANG	National Chiao Tung University, external member

KEYWORDS

Turbidity currents, stratified flows, density driven gravity currents, Delft3D, Shihmen Reservoir, Taiwan.

Preface

Worldwide reservoirs lose their performance due to sedimentation problems. In some reservoirs these problems are caused by turbidity currents. This Master of Science thesis was initiated to gain insight in the behaviour of turbidity currents in reservoirs and develop and test ideas on decreasing their impact on reservoir sedimentation. Of particular interest was the Shihmen Reservoir in Taiwan which suffers under the large amounts of sediments that are brought in by turbidity currents.

The research was supported and financed by Disaster Prevention & Water Environment Research Center (DPWE) at the National Chiao Tung University (NCTU) in Taiwan and Deltares in the Netherlands. Both DPWE and Deltares their support is hereby greatly acknowledged. Special thanks to my graduation committee for their helpful comments and recommendations along the way.

Abstract

Turbidity currents are major transport agents in reservoirs in which high concentrations of fine sediments flow in. Reservoir sedimentation due to turbidity currents is often severe in these cases. Turbidity currents are not well understood due to their complex turbulent flow structure, the interaction between the flow with the particles and the interaction between particles themselves. In this thesis the venting efficiency was determined for three reservoir implementations that might decrease sedimentation caused by turbidity currents. The three were: an additional sediment sluice, blocking a part of the reservoir and a deepened thalweg. Computations were done by means of a Reynolds averaged Navier Stokes (RANS) model. The Shihmen Reservoir in Taiwan was taken as a case study. In this particular reservoir suspended sediment concentrations are measured during the event of a turbidity current. According to the model results the additional sediment sluicing tunnel was the most effective solution. Results indicated that the location of such a tunnel and the reservoir operation method applied are thereby important to increase the venting efficiency. It was shown that a RANS model such as presented, is able to capture the complex behaviour of turbidity currents in reservoirs and is therefore a valuable tool for reservoir managers.

Contents

Abstract	v
List of figures	ix
List of tables	xi
1 Introduction	1
1.1 Background	1
1.2 Problem definition	2
1.3 Research objectives & methods	2
1.4 Thesis outline	3
2 Theory	5
2.1 Definition	5
2.2 Description of the flow structure	5
2.3 Reynolds averaging	7
2.4 Fluid mechanics	7
2.5 The boundary layer	9
2.6 Stratification effects	11
2.7 Reynolds-averaged Navier-Stokes	11
2.8 Transport by advection-diffusion	13
2.9 Settling velocity	14
3 Methods	17
3.1 Numerical approach: Delft3D, RANS solver	17
3.2 The Shihmen Reservoir in Taiwan	18
3.2.1 Background	18
3.2.2 Determining sediment characteristics	20
3.2.3 SSC monitoring using TDR	22
3.3 Model 1: 2DV following the thalweg	24
3.4 Model 2: 3D high resolution	25
3.5 Model experiments	25
3.5.1 2DV sensitivity analyses	25
3.5.2 3D simulations of Typhoon Soulik	27
3.5.3 Valuing three practical solutions	27
4 2DV Sensitivity Analyses	31
5 3D simulations of typhoon Soulik (2013)	37
5.1 Comparison with TDR	37
5.2 Behaviour of the turbidity current	40
5.3 Venting efficiency	40
5.4 Discussion	43
6 Increasing the venting efficiency	47
6.1 Scenario 1: Blockade	47
6.2 Scenario 2: Dawanping tunnel	47
6.3 Scenario 3: Optimised thalweg	49
6.4 Discussion	49
7 Conclusions	53
8 Recommendations	55

Appendices	57
A Principles of turbidity currents	57
A.1 Formation of a turbidity current: the plunge point	58
B 2DV Sensitivity analysis results	61
C Results Soulik (2013)	87
Nomenclature	95
References	99

List of Figures

1.1	Sketch of a reservoir in which a turbidity current is vented through the dam by a low-level outlet.	2
2.1	Sketch of a turbidity current advancing on a slope.	6
2.2	Instabilities of a gravity current head: (1) billows; (2) lobes and clefts.	7
2.3	Physical sub-frameworks defined by the flow field and volume fraction of solids within which fine sediment hydraulics is conventionally investigated (Mehta, 2014).	8
2.4	Relation between shear stress τ and rate of strain $\dot{\gamma}$ at steady state.	9
2.5	Shear stress τ over the depth in an open channel flow.	10
2.6	Schematic view of the three different processes in a sedimentation consolidation experiment.	14
2.7	Schematic view of the development of two (left) or one (right) interfaces in the Kynch sedimentation test depending on the initial concentration c_0	15
3.2	Mud accumulated in the penstock after typhoon Aere (2004).	18
3.1	The location of the Shihmen Reservoir in Taiwan and its watershed.	19
3.3	Volume reduction of the Shihmen Reservoir.	20
3.4	Mud concentrated flow from the silt-sluice and permanent river outlet (PRO) turbine outlets.	20
3.5	Bed topography of the Shihmen Reservoir.	21
3.6	Experiment set up in which the mud characteristics were determined.	22
3.7	Hindered regime measured for $c = 40 \text{ g l}^{-1}$	22
3.8	One of the floating platforms in the Shihmen Reservoir where a time domain reflectometry (TDR) device is placed on.	23
3.9	Typical set-up of a time domain reflectometry (TDR) system that can monitor suspended sediment concentrations (SSC).	24
3.10	The 2DV numerical grid set up based on the thalweg of the Shihmen Reservoir.	25
3.11	three-dimensional (3D) curvilinear grid for the Shihmen reservoir.	26
3.12	Three tested vertical profiles.	27
3.13	Scenario 1: top view of the grid with the weir blocking the arm.	28
3.14	Scenario 2: discharges set for the Dawanping tunnel.	29
3.15	Scenario 2: expected water levels computed beforehand.	29
3.16	Scenario 2: discharges set for the spillway.	29
3.17	Scenario 3: trench dredged.	30
4.1	Fine horizontal grid ($\Delta x = 10 \text{ m}$) with different vertical grids.	33
4.2	Non-hydrostatic pressure.	34
4.3	Coarse horizontal grid ($\Delta x = 100 \text{ m}$) without any additional eddy diffusivity (above) and the same grid with an applied Ozmidov length scale of 5 m (below).	35
5.1	Simulated concentrations in approximately the middle of the reservoir.	38
5.2	Simulated concentrations near the bed of the reservoir.	39
5.3	The σ -correction filter generated instabilities.	40
5.4	Measured suspended sediment concentrations (SSC) from the TDR at cross-section 7.	41
5.5	Simulated SSC by Delft3D at cross-section 7.	41

5.6	Water surface where the plunge point is visible as well as the return current.	42
5.7	Cross section 12: secondary flow in the turbidity current and possibly cross sectional mixing induced by the σ -grid.	42
5.8	Sediment mass near the bed after typhoon Soulik. These sediments might still be in the permeability regime and therefore mobile.	42
5.9	Delft3D SSC at the future Dawanping tunnel.	43
5.10	Low water levels (2015) in the Shihmen reservoir. The simulated accretion can be seen with Google maps.	45
5.11	Explanation of the 'buoyant flow zone'.	45
6.1	Difference of sediment mass near the bed between the Blocked arm till the elevation at 220 m, 225 m, 230 m and the original Soulik simulation.	48
6.2	Difference of sediment mass near the bed between the replace, constant and max cases and the original Soulik simulation.	50
6.3	Difference of sediment mass near the bed between the Trench with a depth of 2 m, 4 m, 6 m and the original Soulik simulation.	51
A.1	A control volume of (turbid) water under a slope.	58
A.2	Velocity and concentration profiles for a flow under air (left) and a turbidity current (right).	58
A.3	Transition from non-stratified to stratified flow.	58
C.1	TDR SSC versus SSC at the Power Plant out-take	87
C.2	TDR SSC versus SSC at the Sluicing Tunnel	87
C.3	TDR SSC versus SSC at the PRO	88
C.4	TDR SSC versus SSC at the water out-take	88
C.5	TDR SSC versus SSC at the Tunnel Spillway	88
C.6	TDR SSC versus SSC at the Spillway (left)	89
C.7	TDR SSC versus SSC at the Spillway (right)	89
C.8	Measured SSC from the TDR at cross-section 7.	90
C.9	Simulated SSC by at cross-section 7.	90
C.10	Measured SSC from the TDR at cross-section 15.	91
C.11	Simulated SSC by at cross-section 15.	91
C.12	Measured SSC from the TDR at cross-section 20 (left).	92
C.13	Simulated SSC by at cross-section 20 (left).	92
C.14	Measured SSC from the TDR at cross-section 20 (right).	93
C.15	Simulated SSC by at cross-section 20 (right).	93

List of Tables

2.1	Empirical coefficients for a standard $k - \epsilon$ model.	13
3.1	Overview of the hydraulic structures in the Shihmen Reservoir, based on Hsu (2013).	19
4.1	Reference models.	32
5.1	Computed venting efficiencies during typhoon Soulik (2013).	43
6.1	Scenario 1, blockade: venting efficiency results.	47
6.2	Scenario 2, Dawanping: venting efficiency results.	49
6.3	Scenario 3, thalweg: venting efficiency results.	49
B.1	Default settings for the two reference models in the 2DV sensitivity analyses.	62
B.2	2DV sensitivity analyses results.	63

Introduction

1.1 BACKGROUND

The first who reported turbidity currents was the Swiss scientist François-Alphonse Forel in the 1880s. Forel was a pioneer in studies after lakes and reservoirs and had described the physical behaviour of water temperature in Lake Geneva (Forel, 1880). He observed that turbid melting waters of the cold Rhone and Rhine plunged beneath the clear waters of Lake Geneva and Lake Constance (Forel, 1885). The plunging was attributed to both temperature and turbidity differences, although it was recognised that the density difference due to turbidity was the most important (Morris & Fan, 1998).

After a few decades, Daly (1936) questioned whether the velocities of density currents sufficed to have eroded submarine 'canyons' (trenches) on continental slopes. By questioning, the existence and the effect of turbidity currents on continental slopes in oceanic waters were further researched (e.g., Kuenen (1938); Heezen and Ewing (1952)). In oceanic waters, turbidity currents can grow to currents powerful enough to break submarine water cables (Middleton, 1993; Simpson, 1997). Grover and Howard (1938) observed and described turbidity currents in Lake Mead, in which currents were observed two months after the filling process of the lake began. Later, Gould (1951) stated that the turbid waters in Lake Mead deposited 50% of the two billion tons deposited material (an accumulation over 14 years) over the entire length of the lake (approximately 145 km). Turbidity currents appeared to be major agents of sediment transport in the lake. To reduce the rate of sedimentation in Lake Mead, Bell (1942) suggested that turbidity currents could be vented from the lake. Although Bell's suggestion was not implemented at Lake Mead, his idea was later applied to some reservoirs in Algeria and China (Morris & Fan, 1998).

Research after transport mechanisms, which are subsequently dependent on fluid dynamics of the currents, are *crucial* to come to a better understanding of turbidity currents themselves (Kneller & Buckee, 2000). Convenient is to conduct those studies in the laboratory, although recently measurement devices are being developed and turbidity currents are — little by little — measured in the field (e.g., Xu, Sequeiros, and Noble (2014)). Insight in turbidity currents is gained by numerical means as well. Here, the main limitation is the high Reynolds number involved which makes accurate solvers as Direct Numerical Solving (DNS) immensely time consuming. Even though efforts are made to increase the range of Reynolds numbers (e.g., Nasr-Azadani and Meiburg (2011)), simulating a complete reservoir is currently not possible. Therefore a less accurate turbulence solver such as in the Reynolds averaged Navier-Stokes (RANS) method is generally applied. This thesis will focus on such numerical modelling applied to a case study in which concentrations were measured in

the field.

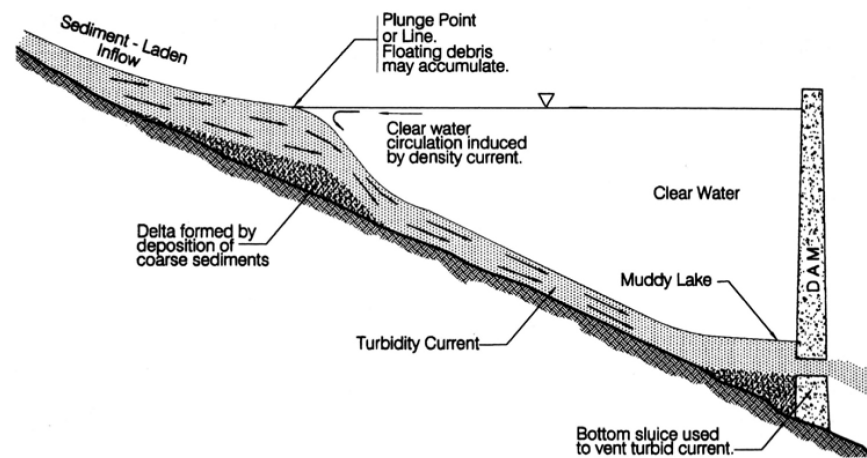


Figure 1.1: Sketch of a reservoir in which a turbidity current is vented through the dam by a low-level outlet, from Morris and Fan (1998).

1.2 PROBLEM DEFINITION

Turbidity currents are not well understood due to the complexity of the hydrodynamic flow and the interaction of sediment particles present in the flow (Kneller & Buckee, 2000). Yet, turbidity currents decrease the performance of the reservoir due to large volumes of sediment that they bring in (e.g. Morris and Fan (1998)). It is desired to predict the behaviour and movement of turbidity currents in order to implement sediment re-routing solutions in reservoir systems (Yang, Lin, Hsu, Chung, & Chang, 2014). In this way more sustainable water reservoirs are created which could serve not only our generation, but future generations as well.

1.3 RESEARCH OBJECTIVES & METHODS

In this thesis it was hypothesised that present day numerical software would be able to simulate turbidity currents in reservoirs. And that they would be sufficiently accurate in order to value of practical solutions against one and the other. Upon that, an overarching research question of this thesis was drawn up as:

“What practical solutions can be recommended to achieve a higher venting efficiency rate for turbidity currents in reservoirs?”

Related research questions (RQs) are:

- RQ1: What are the most important characteristics of the turbidity current in a reservoir?
- RQ2: How does a turbidity current propagate through a reservoir and in which areas do sediments deposit?
- RQ3: Would the RANS Delft3D be capable of simulating turbidity currents accurately?

To achieve the main objective, the Shihmen Reservoir in Taiwan was introduced as a study case. In this particular reservoir high sedimentation rates are observed

due to turbidity currents. The currents are formed during typhoon events. The sediments origin from landslides in the mountainous watershed (Yang, Huang, Tsai, & Chang, 2008) and consists of fine cohesive sediments (Wu, 2009).

Based on literature, present day theory behind hydrodynamic flow and sediment transport was studied. The theory is fundamental to understand the turbidity current. Upon that, a two-dimensional vertical (2DV) and a 3D numerical model were built to simulate turbidity currents in the reservoir. Here the *open-source* software suite called Delft3D was used — known for its wide range of application in hydraulic engineering. The simplified 2DV model was used for fast computations in order to do sensitivity analyses. Three practical solutions were valued with the 3D model. Their value was expressed as an increase (or decrease) of the venting efficiency rate V_{eff} of the reservoir (after Morris and Fan (1998)), given as

$$V_{\text{eff}} = \frac{c_{\text{out}} \cdot Q_{\text{out}}}{c_{\text{in}} \cdot Q_{\text{in}}}, \quad (1.1)$$

where c_{in} is the concentration flowing into the reservoir, c_{out} the concentration flowing out over spillways and through tunnels and $Q_{\text{in,out}}$ is the discharge flowing in and out the reservoir, respectively. A dataset of the typhoon event Soulik (2013) was used to set the flow conditions of the Shihmen reservoir and mud experiments were conducted in order to determine the characteristics of the (hindered) settling velocity.

1.4 THESIS OUTLINE

This thesis is starting with chapter 2 which deals with the present day theory on turbidity currents. A description on turbidity currents, turbulence and suspended fine sediments is given. Discussed in chapter 3 is the Shihmen Reservoir, its SSC monitoring system and the models set up. Chapters 4 to 6 treat the results gained from this thesis. Chapter 4 gives a brief summary of the 2DV sensitivity analyses outcome. In chapter 5 the simulations by the 3D model of typhoon Soulik (2013) are presented and discussed. Typhoon Soulik was re-simulated in chapter 6, only this time, three practical solutions were implemented in the model. The thesis ends with the conclusions and discussions in chapter 7 and, in line with those findings, recommendations are given in chapter 8. For those who are completely new to the subject of density currents, reference is made to appendix A. Other appendices include simulation results.

Theory

As introduced, turbidity currents are formed when a laden sediment flow dives under ambient fluid of the reservoir. This occurs at the so-called plunge point. Reference is made to appendix A that elaborates on the principles of plunging and density driven currents. The anatomy of turbidity currents and the transport mechanism due to turbulence and hindered settling are treated in this section.

2.1 DEFINITION

The name 'turbidity current' was first introduced by Johnson (1939)¹, as a synonym for a density current produced by sediments in suspension. Sediment in those currents were kept in suspension by the fluid turbulence. Kneller and Buckee (2000) wisely noted that the term 'turbidity current' presently stands for a natural phenomenon whose exact nature is unclear — pointing mainly to the several variations in how sediment is kept into suspension, the so-called sediment support mechanisms. Those mechanisms are, e.g., suspension due to turbulence, hindered settling or dispersive pressure owing to grain interactions. Besides, confusion with other (partially) related terms and the name 'turbidity current' is easily made; consider for instance the words: turbidites (i.e., bed deposits from turbidity currents), turbid (i.e., opaque with sediment), turbulence (i.e. disturbed by eddies) or the similarity with: particle-driven density currents, gravity currents or sediment gravity flow (Kneller & Buckee, 2000). In order to prevent confusion, this thesis follows the definition of Kneller and Buckee (2000) as stated below.

“A turbidity current is a suspension current in which the interstitial fluid is a liquid (generally water)...We define a suspension current as 'flow induced by the action of gravity upon a (fluidal) turbid mixture of fluid and (suspended) sediment, by virtue of the density difference between the mixture and the ambient fluid.”

2.2 DESCRIPTION OF THE FLOW STRUCTURE

A turbidity current typically has a distinct head (or front), body and occasionally a tail. Figure 2.1 shows a sketch of the head and body of the turbidity current and typical profiles for internal concentrations and velocities. The head is an important part of a turbidity current because it sets the base of the fluid dynamics for the following body and tail. Generally it holds that the turbulent

¹according to Gould (1951). The name was first implemented by Bell (1942).

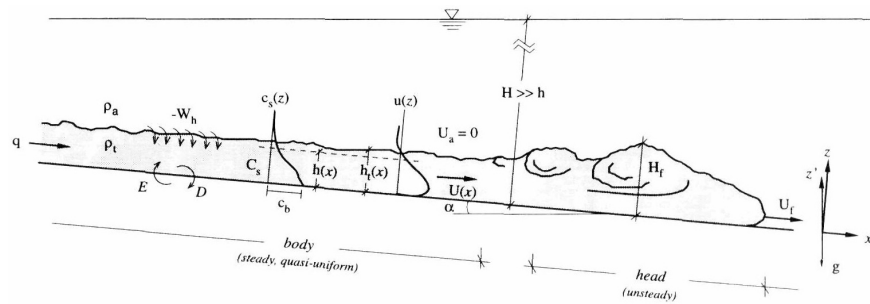


Figure 2.1: Sketch of a turbidity current advancing on a slope, from Altinakar et al. (1996).

energy generated in the head keeps particles in the complete turbidity current into suspension.

Only a few physical descriptions of the body of gravity currents exists in literature (Kneller & Buckee, 2000). Ellison and Turner (1959) described the body as a region of steady downstream velocity which has a thin, dense layer of fluid near the base of the current which, with increasing downstream velocity, mixes with the ambient fluid at the upper interface as an 'irregular succession of large eddies'.

The mass and momentum balance of the head differ significantly from those of the body and the tail. As the head wants to propagate, it has to displace the ambient fluid, which is in general at rest. The produced resistance by the ambient fluid to the head is larger than the resistance caused by bed friction and by the upper interface. Therefore the head has to have more potential energy (and is thus thicker) than the following body (where only frictional resistance plays a role).

In the head, mixing processes with the ambient fluid take place due to turbulence (Simpson & Britter, 1979). Two areas of high negative Reynolds stresses were identified by experiments: 1) at the top of the head, related to Kelvin-Helmholtz billows, and 2) beneath the nose of the current, attributed to the entrainment of over-riden ambient fluid which is buoyant within the current (Kneller, Bennett, & McCaffrey, 1999). It was concluded by Simpson and Britter (1979) that mixing at the nose accounted only for 1% of the total mixture, the rest occurred at the upper interfaces during their experiments. At the upper interface, mixing process is characterised by two types of turbulence structures:

- Kelvin-Helmholtz instabilities called billows, formed at the back of the head (see figure 2.2, part 1). Kelvin-Helmholtz instabilities increase when the bottom slope increases. However, the propagation of the front remains constant for increasing slopes because the large gravitational force is counterbalanced by the increased entrainment in the head and the flow behind it (Britter & Linden, 1980).
- Lobes and clefts (see figure 2.2, part 2), a complicated 3 dimensional form. The mechanism behind the initial formation of lobes and clefts is a buoyancy-induced instability that acts locally near the leading edge. Härtel, Meiburg, and Necker (2000) and Härtel, Carlsson, and Thunblom (2000) pointed out that the frontal instability is not caused by overrun light fluid, as assumed first; it is rather due to the unstable stratification that prevails at the leading edge between the nose and stagnation point of the front.

Overall, the vertical mean velocity profile can be distinguished in an inner and outer region. The inner region is similar to a conventional turbulent boundary-layer and has a positive velocity gradient. The outer region, i.e. the

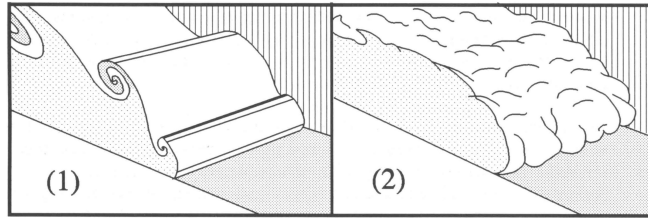


Figure 2.2: Instabilities of a gravity current head from Sloff (1997): (1) billows; 2) lobes and clefts.

shear layer, has a negative velocity gradient. Generally the outer region is 5 – 10 times thicker than the inner region (Meiburg & Kneller, 2010).

The shape of the velocity profiles are directly related to turbulence. Hence, turbulence generated in the head, which is driven by a density difference, is responsible for the mixing processes within the turbidity current and therefore determines the density difference. The amount of turbulence is affected by the presence of sediments. Velocity profiles (and underlying processes) are therefore important.

2.3 REYNOLDS AVERAGING

In analogy with numerous textbooks on turbulent flows, the velocities of the flow can be expressed as a mean velocity plus a turbulent fluctuation that accounts for turbulence. This is known as Reynolds averaging. Values of flow velocities for turbulent flow are time averaged with

$$u = \bar{u} + u', \quad (2.1)$$

wherein \bar{u} is the average flow velocity and u' the turbulent fluctuation. By time averaging, the random nature of the u' fluctuations have zero means. Therefore the root-mean-square of the velocities are introduced

$$u_{\text{rms}} = (\overline{u'^2})^{1/2}, \quad (2.2)$$

which refers to the mean intensity of turbulence. The Turbulent Kinetic Energy (TKE) k per unit mass of fluid is determined by time averaging the root-mean-squared velocities as

$$k \equiv \frac{1}{2} (\overline{u'^2} + \overline{v'^2} + \overline{w'^2}), \quad (2.3)$$

and is the quantitative expression for turbulent eddies.

2.4 FLUID MECHANICS

Understanding the transport mechanisms of turbidity currents is interlinked with the understanding of the turbulent structure within the current. Especially the role of turbulence in high concentration suspension currents is a source of considerable debate (Kneller & Buckee, 2000). In this thesis fine sediment sizes of a range approximately $0.1 \mu\text{m}$ to $62.5 \mu\text{m}$ are treated. In high concentrations these sediments react different on shear stresses than in dilute concentrations. Figure 2.3 gives an idea of how volumes of fine sediments act differently under laminar or turbulent conditions; i.e. the behaviour is either as particle mechanics, Newtonian mechanics, non-Newtonian mechanics or soil mechanics. Whether a flow is laminar or turbulent is determined according to the dimensionless Reynolds number,

$$\text{Re} = \frac{u \cdot l}{\nu}. \quad (2.4)$$

Re is a measure to express the ratio of inertia force to viscous force. It is also the ratio of the smallest turbulent length scale, i.e. the kinematic viscosity² of the fluid ν , to the largest possible length l , generally the depth of the fluid or in the case of turbidity currents, the height of the current limited by the stratification. A low Reynolds number indicates flows that are dominated by viscosity, i.e. laminar flow. High Reynolds numbers are said to be fully turbulent and considered where viscous forces have little effect. Typical values for the transition between laminar to turbulent flow are $Re = 1000$ to 2000 .

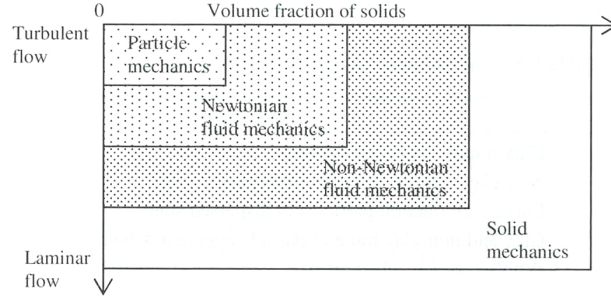


Figure 2.3: Physical sub-frameworks defined by the flow field and volume fraction of solids within which fine sediment hydraulics is conventionally investigated (Mehta, 2014).

The dynamic viscosity of the fluid mixture μ varies with temperature, density and mixture composition. Most fluids respond to the total fluid shear stress τ (in the x -direction) as follows:

$$\tau = \mu\gamma = \mu \frac{\partial u}{\partial z} \quad (2.5)$$

In Newtonian fluids ν is not dependent on the rate of strain γ , and thus the shear stresses τ are determined solely by³ μ . Examples of Newtonian and non-Newtonian fluid behaviour under Eq. 2.5 are plotted in figure 2.4.

The interaction between turbulence and sediment particles is in fact an exchange of momentum which is given by

$$\tau_{\text{turb}} = -\rho \overline{u'w'}. \quad (2.6)$$

The total fluid shear stress consists of the turbulent τ_{turb} and viscous τ_{visc} contributions

$$\tau = \tau_{\text{visc}} + \tau_{\text{turb}} = \rho\nu_T \frac{\partial \bar{u}}{\partial z} + \mu \frac{\partial \bar{u}}{\partial z} \quad (2.7)$$

in which ν_T is the kinematic turbulent viscosity which varies with the intensity of turbulence. In order to determine the turbulent viscosity ν_T , the eddy mixing length hypothesis is used (Prandtl, 1952; Liggett, 1994). Here the assumption is made that the shear flows of two directions are in the same order of magnitude. Thus, the anisotropic effects in the horizontal plane are ignored. Winterwerp and van Kesteren (2004) pointed out that the lateral and vertical turbulent fluctuations can be 30% and 45% smaller in reality, respectively. Even though isotropic turbulent models have been applied with great success in the shallow water environment. Thus:

$$O(\overline{|u'|}) = O(\overline{|w'|}) = l_t \left| \frac{\partial \bar{u}}{\partial z} \right| \quad (2.8)$$

²The kinematic viscosity is related to the dynamic viscosity of the fluid μ with $\nu = \mu/\rho$.

³This also holds that $\partial\tau/\partial z = \nu(\partial^2 u/\partial z^2)$.

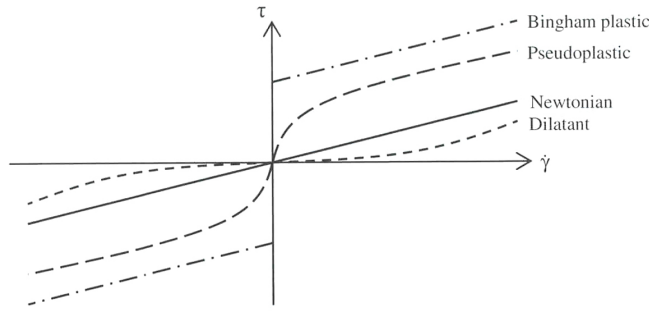


Figure 2.4: Relation between shear stress τ and rate of strain $\dot{\gamma}$ at steady state, from Mehta (2014).

Here is l_t the mixing length according to Prandtl's hypothesis, expressing the size of turbulent eddies. Substituting Eq. 2.8 into Eqs. 2.6 and 2.7 (neglecting the viscous component under the assumption of turbulent flow) gives the eddy viscosity

$$\nu_T = l_t^2 \left| \frac{\partial \bar{u}}{\partial z} \right|. \quad (2.9)$$

This equation is in line with the expression of the mixing length of von Kármán (Liggett, 1994):

$$l_t = \sqrt{\frac{\kappa}{\rho} \frac{d\bar{u}/dz}{\sqrt{d^2\bar{u}/dz^2}}}, \quad (2.10)$$

where κ is the Karman constant. With this equation the mixing length l_t can be determined once the flow velocity profile $u(z)$ is known. Generally accepted is $\kappa = 0.41$ for open waters.

2.5 THE BOUNDARY LAYER

Distinction can be made between near-wall turbulence and free turbulence. The near-wall shear stresses induced by the flow over the bed are treated here, i.e. τ_b . The shear stress at the bed is one of the two most important parameters for the transport of sediments. The other is the settling velocity of suspended particles.

In Eq. 2.7 the total fluid shear stress was the sum of both turbulent shear stresses and viscous shear stresses. To explain the velocity profile over the vertical z , consider a steady state open channel flow. In such a channel τ increases linearly over depth, with τ_b being the maximum at the bed and zero at the water surface. Figure 2.5 shows the turbulent boundary layer over the water depth h and the a schematic presentation of τ of the channel. It consists of a viscous boundary layer with thickness δ_1 and a log layer above. The viscous contribution τ_{visc} to Eq. 2.7 is often ignored, especially when δ_1 is smaller than the hydraulic roughness height of the bed. In case of a smooth bed this is not the case.

The bed shear stress is per definition:

$$\tau_b = \rho u_*^2, \quad (2.11)$$

where u_* is the friction velocity. This is a fictive velocity that cannot be measured in the field. We assume the mixing length to increase linearly with elevation z above the bed:

$$l_t = \kappa z. \quad (2.12)$$

Substituting in equation 2.7 and 2.9 gives:

$$\tau_b = \rho \kappa^2 z^2 \left| \frac{\partial \bar{u}}{\partial z} \right| \frac{\partial \bar{u}}{\partial z}, \quad (2.13)$$

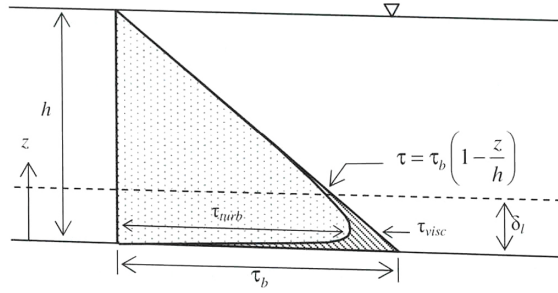


Figure 2.5: Shear stress τ over the depth in an open channel flow, from Mehta (2014).

or, under the definition of Eq. 2.11

$$\frac{\kappa z}{u_*} \frac{\partial \bar{u}}{\partial z} = 1 \quad (2.14)$$

In situations where stratification effects due to density gradients play a role, the right-hand side of Eq. 2.14 has to be defined with some kind of function dependent on the degree of stratification.

Integration of Eq. 2.14 yields:

$$\frac{\bar{u}}{u_*} = \frac{1}{\kappa} \ln z + C \quad (2.15)$$

where the constant C can be determined by taking $\bar{u}(z_0) = 0$. Hence:

$$\frac{\bar{u}}{u_*} = \frac{1}{\kappa} \ln \frac{z}{z_0} \quad (2.16)$$

The roughness height z_0 is the origin of the velocity profile. Eq. 2.16 is widely stated as:

$$\frac{\bar{u}}{u_*} = \frac{1}{\kappa} \ln \frac{z}{k_s} + B_s \quad (2.17)$$

with coefficient B_s depending on the turbulent Reynolds number Re_* , and the bed roughness length (or Nikuradse height) k_s [mm]. In case of turbulent situations (i.e. where the turbulent Reynolds number $Re_* = \sqrt{k}l/\nu > \approx 70$), commonly $B_s = 8.5$. The Manning roughness was used in this thesis, which is described by

$$n = 0.032 \cdot k_s^{1/6} \quad (2.18)$$

Based on the open channel flow assumed,

$$\tau = \tau_b \left(1 - \frac{z}{h}\right) \quad (2.19)$$

and the eddy diffusivity profile is found to be parabolic over the depth:

$$\nu_T(z) = \kappa u_* z \left(1 - \frac{z}{h}\right) \quad (2.20)$$

(under the assumption of $z_0^2 \ll 1$). This parabolic profile does not fully describes the data measured in laboratory flume experiments. And, under the assumption of Eq. 2.14, the profile is sensitive to stratification.

$$\frac{\bar{u}}{u_*} = \frac{z u_*}{\nu} < 5 \quad (2.21)$$

2.6 STRATIFICATION EFFECTS

Stable density gradients reduce vertical mixing processes. These density differences are induced by gradients in suspended sediment (among others). The damping involves reduction in mixing of both momentum and matter. As turbulence mixes in the vertical in a stably stratified flow, it must lift the heavier fluid up and move the lighter water down. The extra work involved acts damping the turbulence. This effect is known as buoyancy destruction.

The newly obtained velocity profile due to stratification can be described by replacing the 1 in Eq. 2.14 with a function f^n .

$$\frac{\kappa z}{u_*} \frac{d\bar{u}}{dz} = f^n \left(\frac{z}{L_m} \right) \quad (2.22)$$

L_m is the Monin-Obukhov turbulence length scale which depends on the degree of stratification. The latter can be expressed with the gradient Richardson number

$$Ri_g = \frac{-\frac{g}{\rho_0} \frac{\partial \rho}{\partial z}}{\rho \left[\left(\frac{\partial u}{\partial z} \right)^2 + \left(\frac{\partial v}{\partial z} \right)^2 \right]} \quad (2.23)$$

Generally accepted is that stable stratification occurs when $Ri_g > 0.25$ (Turner, 1973). Parker, Garcia, Fukushima, and Yu (1987) proposed an empirical based relation for the entrainment of ambient fluid into the suspension current

$$e_w = \frac{0.075}{(1 + 718 Ri^{2.4})^{0.5}} \quad (2.24)$$

in which e_w is the entrainment coefficient and where Ri is the (bulk) Richardson number. From Eq. 2.24 it can be seen that dilution due to entrainment through the stratification approximates zero if the Richardson numbers increase. Turbidity currents with low internal Froude numbers (the inverse of the Richardson number) therefore hardly entrain ambient water.

2.7 REYNOLDS-AVERAGED NAVIER-STOKES

To describe the water movement in the flow, the Navier-Stokes equations were used. Under the assumption of that the fluids are incompressible and the density differences are small (i.e. $\Delta \rho \ll \rho_0$ in which ρ_0 is a reference density), the 3D continuity equation written in Einstein's notation reads

$$\frac{\partial u_i}{\partial x_i} = 0 \quad (2.25)$$

and the 3D momentum equations read

$$\frac{\partial u_i}{\partial t} + u_i \frac{\partial u_j}{\partial x_i} + \epsilon_{ijk} 2\Omega_j u_k = -\frac{1}{\rho_0} \frac{\partial p}{\partial x_i} + \frac{1}{\rho_0} \frac{\partial \tau_{ij}}{\partial x_j} + \frac{\rho}{\rho_0} g \delta_{i3} \quad (2.26)$$

in which δ_{ij} is the Kronecker delta, ϵ_{ijk} is the cyclic permutation symbol, Ω_j is the planetary vorticity and τ_{ij} are the stresses in the fluid.

The pressure function p consists of a hydrostatic part and a hydrodynamic part. Generally, reservoirs are considered as shallow waters in which the flow can be assumed hydrostatic. However, in the head of the turbidity current and at the plunge point, relatively high vertical accelerations are expected which would violate the assumption. Therefore a hydrodynamic part q , which will be determined numerically, was included in p .

To account for misalignment in the pressure gradient in the hydrostatic part due to density gradients (i.e. baroclinity), the hydrostatic part of p consists

of a barotropic part (i.e. $p_{atm} + \rho gh$) plus density induced differences due to gradients in sediment concentration (i.e. $\rho = \rho(c)$).

$$p = p_{atm} + g \int_{x_3}^0 \rho dx'_3 + q \quad (2.27)$$

Here p_{atm} is the atmospheric pressure. In hydrostatic computations where $q = 0$, the pressure function equals the hydrostatic part. This implies that the momentum equations reduce to the shallow water equations. In that case the vertical momentum equation simply equals

$$\frac{\partial p}{\partial x_3} = -\rho g. \quad (2.28)$$

By introducing the Reynolds averaged stresses τ_{ij} a closure problem arises due to the non-linear term in Eq. 2.6. Yet, in order to solve the stresses the standard turbulent closure model $k - \epsilon$ was used including a buoyancy term. With this model, the mixing length l_t and the turbulent viscosity become a property of the flow and therefore no additional damping functions for the stratification would be necessary. The $k - \epsilon$ model presented in 2.29 is valid for high turbulent flows. In flows that exhibit laminar characteristics (e.g., high concentration mud flows in which the turbulence Reynolds number $Re_* \approx 2\nu_T/\nu < 70 - 100$), one should account for Low Reynolds-effects which are not treated here.

$$\begin{aligned} \frac{\partial k}{\partial t} + \frac{\partial u_i k}{\partial x_i} - \frac{\partial}{\partial x_i} \left(\nu + \frac{\nu_T}{\sigma_k} \right) \frac{\partial k}{\partial x_i} &= \nu_T \left(\frac{\partial u_i}{\partial x_j} + \frac{\partial u_j}{\partial x_i} \right) \frac{\partial u_i}{\partial x_j} \\ &+ \delta_{i3} \frac{g}{\rho} \frac{\nu_T}{\sigma_T} \frac{\partial \rho}{\partial x_i} - \epsilon \\ \frac{\partial \epsilon}{\partial t} + \frac{\partial u_i \epsilon}{\partial x_i} - \frac{\partial}{\partial x_i} \left(\nu + \frac{\nu_T}{\sigma_\epsilon} \right) \frac{\partial \epsilon}{\partial x_i} &= C_{1\epsilon} \nu_T \frac{\epsilon}{k} \left(\frac{\partial u_i}{\partial x_j} + \frac{\partial u_j}{\partial x_i} \right) \frac{\partial u_i}{\partial x_j} \\ &+ \delta_{i3} (1 - C_{3\epsilon}) \frac{\epsilon}{k} \frac{g}{\rho} \frac{\nu_T}{\sigma_T} \frac{\partial \rho}{\partial x_i} - C_{2\epsilon} \frac{\epsilon^2}{k} \end{aligned} \quad (2.29)$$

In Eqs. 2.29 k is the Turbulent Kinetic Energy (TKE) (here repeated for completeness) and ϵ is the turbulent dissipation rate per unit mass.

$$k \equiv \frac{1}{2} \overline{u'_i u'_i} \quad \text{and} \quad \epsilon \equiv \frac{1}{2} \nu \overline{\left(\frac{\partial u'_i}{\partial x_j} + \frac{\partial u'_j}{\partial x_i} \right)^2} \quad (2.30)$$

The first term in Eq. 2.29 represents the rate of change in either k or ϵ , the second term represents advection, the third term represents diffusion, the fourth term gives the turbulence production term, the fifth term holds damping by buoyancy and the sixth term is the dissipation. In the formula the Prandtl-Schmidt numbers σ_k , σ_ϵ and coefficients c_μ , $C_{1\epsilon}$, are $C_{2\epsilon}$, described in literature were found by calibration (e.g. Rodi (1984)) and given in table 2.1.

Once k and ϵ are known by means of numerical solving, the eddy viscosity can be determined with:

$$\nu_T = c_\mu \frac{k^2}{\epsilon} \quad (2.31)$$

In highly stratified conditions, internal waves may exchange vertical momentum but not mass. However, the standard $k - \epsilon$ model damps the vertical exchange due to an overestimation of the buoyancy term (Simonin, Uittenbogaard, Baron, & Viollet, 1989). Therefore Uittenbogaard and van Kester (1992) suggested to control the buoyancy term by the boolean coefficient $C_{3\epsilon}$ depending on the rate of stratification.

Table 2.1: Empirical coefficients for a standard $k - \epsilon$ model.

Prandtl-Schmidt numbers		Coefficients			Stratification	
			stable	unstable		
σ_k	σ_ϵ	C_μ	$C_{1\epsilon}$	$C_{2\epsilon}$	$C_{3\epsilon}$	$C_{3\epsilon}$
0.09	1.44	1.92	1.0	1.3	1	0

2.8 TRANSPORT BY ADVECTION-DIFFUSION

Sediments in suspension can be treated as a single phase fluid⁴. This means that turbulence in the flow effects the suspension of the sediments but not vice versa. Sediments follow the turbulent water movements with one exception: the settling velocity w_s . A function for w_s is given in the following section, first the transport mechanism itself is treated.

From a sediment mass balance the following 3D advection-diffusion equation can be derived

$$\begin{aligned} \frac{\partial c^{(i)}}{\partial t} + \frac{\partial}{\partial x_i} \left[(u_i - \delta_{i3} w_s^{(i)}) c^{(i)} \right] \\ - \frac{\partial}{\partial x_i} \left[(D_m + D_T) \frac{\partial c^{(i)}}{\partial x_i} \right] - \frac{\partial}{\partial x_i} \left(\overline{\delta_{i3} w_s' c^{(i)'}} \right) = 0 \end{aligned} \quad (2.32)$$

Here the superscript (i) identifies a specific fraction (in this thesis one single fraction is treated), D_m is the molecular diffusion coefficient and D_T the eddy diffusivity. The diffusion part of Eq. 2.32 is based on Fick's law for diffusion. The diffusion coefficient D_T is directional dependent on the anisotropy of the turbulence (i.e. taken isotropic in the $k - \epsilon$ model). As the eddy viscosity ν_T relates to the transport of momentum, the eddy diffusivity D_T relates to transport of a scalar, i.e. passive tracers such as heat, dye and mass. The ratio between the eddy viscosity and the eddy diffusivity is given by the turbulent Schmidt number for mass matter σ_{SC}

$$D_T = \frac{\nu_T}{\sigma_{SC}} \quad (2.33)$$

Since the transport of both momentum and scalars are linked to the fluctuating turbulent velocities, it is expected that the eddy viscosity and diffusivity will have the same value ($\sigma_{SC} \approx 1$). This is known as the Reynolds analogy. However, momentum is continuously affected by the ambient stresses and therefore its transport is less effective than the transport of a scalar. Thus the eddy viscosity should generally be smaller than the eddy diffusivity ($\sigma_{SC} < 1$). By coupling the eddy diffusivity profile to the parabolic eddy viscosity profile found in Eq. 2.20, one would obtain the the well-known Rouse concentration profile for sediments. Based on results from experiments with high initial sediment concentrations, Winterwerp (2006) indicated that possibly $\sigma_{SC} = 2$. This value alters the sediment concentration profile significantly and the agreement between predictions and observations improved considerably for the experiments under his consideration. During this study D_T was set equal to 1. Other eddy diffusivity tests were conducted to investigate the effect of the eddy diffusivity on the turbidity current.

⁴It is noted that the well-known Rouse number $= w_s / \kappa u_*$ appears to be an appropriate parameter to decide whether a sediment suspension may be treated as a single phase fluid, see e.g. Winterwerp and van Kesteren (2004).

2.9 SETTLING VELOCITY

A function for the settling velocity of sediments is important to describe the vertical movement of the particles. Toorman (1996) derived a general 1D equation for the complete settling regime given in Eq. 2.34. The settling regimes consists of a sedimentation regime and a consolidation regime. The first is of interest when the turbidity current is active. The second is of interest shortly after the turbidity current event. Assumptions made for this equation were: 1) solid particles are of the same size, shape and density, 2) the particles and fluid are incompressible, 3) the flow is one-dimensional and 4) the settling velocity can be determined by local concentration only.

$$\frac{\partial c}{\partial t} + \frac{\partial}{\partial z} [cW_{sk}(c)] + \frac{\partial}{\partial z} \left[D(c) \frac{\partial c}{\partial z} \right] = 0 \quad (2.34)$$

Here W_{sk} is the total settling velocity function including permeability effects and $D(c)$ is the total dissipation coefficient. The total dissipation coefficient is the sum of the turbulent eddy diffusivity effects (D_T), consolidation diffusion effects (D_c) and the molecular diffusion effects (D_m). D_m is generally negligible, and D_T as well if we consider an one-dimensional experiment wherein turbulence can be neglected (waves and currents are absent). The sedimentation consolidation in such an experiment is therefore dependent on three main regimes (Dankers & Winterwerp, 2007) which are shown in figure 2.6, knowing:

1. a hindered regime where the effective stress is zero ($\sigma' = 0$) and the settling velocity is dependent on the concentration of particles;
2. a permeable regime where physically compression and expulsion occurs ($\sigma' \approx 0$) and the settling velocity is thus dependent on the permeability;
3. an effective stress regime ($\sigma' > 0$) where compression is predominant.

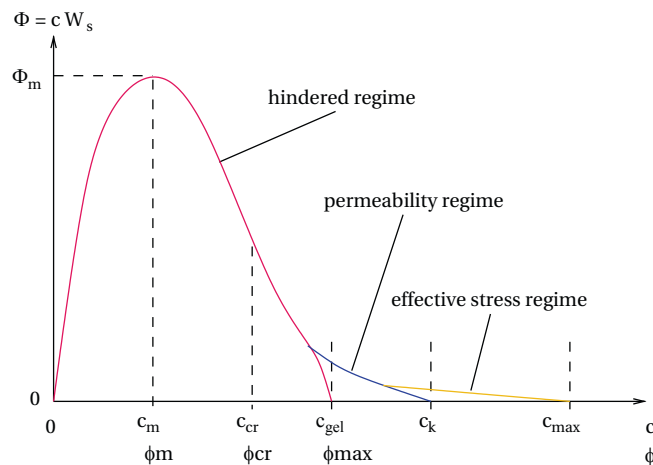


Figure 2.6: Schematic view of the three different processes in a sedimentation consolidation experiment from the flux curve ($\Phi = cW_{sk}$) as a function of concentration c . Plot from Camenen and van Bang (2011).

In order to determine a hindered settling function plus a part of the permeability regime, Kynch (1952) developed a theory on the so-called batch experiment. This experiment initially consists of a well-mixed, but uniformly distributed, suspension of particles which is subjected to gravity only. It will result in three different suspended phases, knowing a maximum concentration $c = c_{max}$ at the bottom, clear water at the top and a well-mixed suspension $c = c_0$ in between.

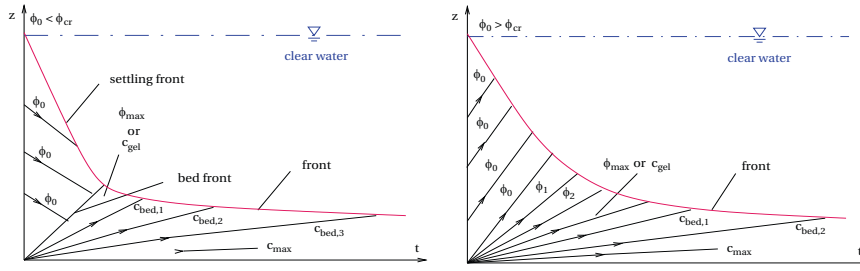


Figure 2.7: Schematic view of the development of two (left) or one (right) interfaces in the Kynch sedimentation test depending on the initial concentration c_0 . The lines with an arrow correspond to the iso-concentration lines with $\phi_0 < \phi_1 < \phi_2 < \phi_{\max}$ and $c_{\text{gel}} < c_{\text{bed},1} < c_{\text{bed},2} < c_{\text{bed},3} < c_{\max}$. Plots from Camenen and van Bang (2011).

Kynch (1952) developed a simple wave equation that describes the process, it reads

$$\frac{\partial c}{\partial t} + \frac{\partial \Phi}{\partial z} = 0 \quad (2.35)$$

where $\Phi = cw_{sh}$ the sediment flux, also known as the Kynch batch flux. $w_{sh} = w_{s0}f(c)$ is the hindered settling velocity which is assumed to be a function of concentration c and the settling velocity of one single particle w_{s0} . The batch theory is, however, not directly applicable to cohesive matter because these are sediments with varying size, density and shapes. Moreover, cohesive sediment particles come in flocs and are not fixed Euclidean; cohesive particles are deformable. Larger flocs may form due to presence of salinity, low pH-values, strong turbulence and possibly other mechanisms. Therefore, instead of the concentration c for non-cohesives, Kranenburg (1992) introduced the volumetric concentration of flocs ϕ ($\phi = (\rho_s - \rho)/(\rho_f - \rho) \cdot c$, with ρ , ρ_s and ρ_f are the water, sediment and flocs density, respectively). Eq. 2.35 (or Eq. 2.34 with $D(c) = 0$) may then be rewritten as

$$\frac{\partial \phi}{\partial t} + W_{s0}F(\phi)\frac{\partial \phi}{\partial z} = 0 \quad (2.36)$$

$$F(\phi) = \frac{\partial [\phi f(\phi)]}{\partial \phi} \quad (2.37)$$

with $f(\phi) = w_{sh}/w_{s0}$. Eq. 2.36 is a convection equation which can be solved by the method of characteristics with $dz/dt = w_{s0}F(c)$, see figure 2.7.

Hindered regime

The choice of the hindered settling formulas may significantly influence the results for the Kynch theory, even if the formulas yield similar prediction for the settling velocity (Camenen & van Bang, 2011). In this thesis the formula of Richardson and Zaki (1954) was used. They suggested:

$$f = (1 - \phi)^m \quad (2.38)$$

with m experimentally determined as $m = 4.65$. The formula was used as it was by default implemented in the software (to be exact, Delft3D uses $m = 5$). A more physically sound hindered settling velocity was presented by Winterwerp (1999).

$$f = \frac{(1 - \phi)(1 - c)}{1 + 2.5\phi} \quad (2.39)$$

He reasoned that, as each floc within a suspension can be considered to settle in the remainder of the suspension, three hindering effects could be distinguished:

1. Return flow and wake formation caused by the particles that settle. Neighbouring particles will be influenced by this effect and their effective settling velocity will be decreased by a factor $(\phi - 1)$.
2. Increased viscosity in which the flocs settle. In the remainder of the suspension the viscosity increased with $\mu_{\text{eff}} = \mu_{\text{mol}}(1 + 2.5\phi)$ (following the classical formula of Einstein) in which μ_{eff} is the effective viscosity and μ_{mol} is the molecular viscosity.
3. Buoyancy or reduced gravity due to an increased bulk density in which the flocs settle. The effective settling velocity is therefore decreased by a factor $(1 - c)$.

To include possible non-linear effects, an exponent m was added (Dankers & Winterwerp, 2007) to the formula.

$$f = \frac{(1 - \phi)^m (1 - c)}{1 + 2.5\phi} \quad (2.40)$$

In case the sediment is settling in a liquid, the return flow should be linear (i.e. $m = 1$). Otherwise, the downward flux of settling sediments induce an equal upward flux of water (or sediment-water) and non-linearity should be taken into account ($m \neq 1$). This means that hydrodynamic effects generated by the settling particle (for example acceleration and deceleration of flow, and the curvature of streamlines) are taken into account (Dankers, 2006).

Permeable regime & total settling function

With respect to the movement of the turbidity current and the sediment dynamics within that suspension, the permeable regime and the effective stress regime is less of interest. If relatively large volumes of sediments are in the permeability regime, the sediments have settled near the bed and the turbidity current died. Reference is made to Merckelbach and Kranenburg (2004) and Winterwerp (1999) who suggested a function for the permeable regime and a total settling function W_{sk} , respectively.

Methods

This chapter gives a description on the software used, the two models built and the data acquired. The case study 'Shihmen Reservoir' is introduced briefly and the method on how SSC are determined in the reservoir is elaborated. Upon that, the 2DV sensitivity analyses and the 3D simulations of the typhoon event Soulik (2013) are given and the three practical implementations for the Shihmen Reservoir are introduced.

3.1 NUMERICAL APPROACH: DELFT3D, RANS SOLVER

Delft3D is an open-source solver for the RANS set of equations and the sediment transport formula presented earlier. The most important aspects about Delft3D are presented in this section. For additional information reference is made to the of the software (Deltares, 2014) or in Lesser, Roelvink, van Kester, and Stelling (2004).

The discretisation is done by Delft3D over a curvilinear grid horizontally and a either a σ -grid or z -grid vertically. Here the σ -grid is an dynamic grid that is fitted between the bed level ($\sigma = -1$) and the water level ($\sigma = 0$). The z -grid is a fixed grid defined between z_{bot} and z_{top} . Non-hydrostatic computations are possible only with the z -grid.

In stratified environments the σ -grid is known to introduce numerical diffusion with horizontal gradients both in the baroclinic pressure term and in the horizontal diffusion term. Especially near steep bottom gradients where the grid is no longer parallel to the stratification. In order to reduce numerical mixing a so-called σ -correction was implemented (i.e. an anti-creep approach). The corrector interlinks neighbouring cells that have the same elevation with each other and is based on a finite volume approach. In steep slopes it is expected to improve results gained from the advection-diffusion equations for transport of sediments.

The $k - \varepsilon$ model discussed earlier is implemented in the software. In Delft3D so-called *background* eddy viscosities v_T^{back} are available to add a constant amount of ambient turbulence to the eddy viscosity v_T which is computed by the $k - \varepsilon$ model. These background values are user defined for the horizontal eddy viscosity v_T^H and the vertical eddy viscosity v_T^V .

$$v_T^V = \max(v_T, v_T^{V;\text{back}}) \quad (3.1)$$

$$v_T^H = v_T^V + v_T^{H;\text{back}} \quad (3.2)$$

A similar procedure is followed for the eddy diffusivity with inclusion of the

Brunt-Väisälä frequency of internal waves

$$D_T^{D3D} = \max \left(D_T, 0.2L_{oz}^2 \sqrt{-\frac{g}{\rho} \frac{\partial \rho}{\partial z}} \right) \quad (3.3)$$

Here L_{oz} is the Ozmidov length scale which is mostly known from oceanography studies. The Delft3D eddy diffusivities read

$$D_T^V = \max \left(D_T^{D3D}, D_T^{V;back} \right) \quad (3.4)$$

$$D_T^H = D_T^V + D_T^{H;back} \quad (3.5)$$

To be clear, the Delft3D eddy viscosities and eddy diffusivities are used in the momentum equations given in Eq. 2.26 only and not in the $k - \epsilon$ turbulence model given by Eq. 2.29.

3.2 THE SHIHMEN RESERVOIR IN TAIWAN

3.2.1 Background

Every summer Taiwan is hit by typhoons that origin from the pacific ocean. The average annual rainfall is about 2350 mm per year, the variation is, however, extreme with intense rainfalls of over 1000 mm per day. This results in severe floods during typhoon period and draughts throughout the rest of the year. For flood protection, water storage and generation of electricity, Taiwan has constructed several water reservoirs in the past century. After completion of these reservoirs, sedimentation problems arose.

The Shihmen Reservoir is located in the mid north of Taiwan (see figure 3.1) and its watershed is approximately 763 km². The severe rainfall in the mountainous watershed of the Shihmen Reservoir weakens the soil drastically. Eventually landslides fall in the upstream reaches of the Shihmen Reservoir. Water from upstream laden with high concentrations of sediments enter the reservoir and generate turbidity currents. The capacity of the Shihmen Reservoir is decreasing rapidly since the moment of construction. Currently, more than one-third of the reservoir has silted up resulting in a decrease of the reservoir its performance; the effective storage capacity decreased from 309×10^6 m³ in 1964 to 219×10^6 m³ in 2007 (Yang et al., 2014). In order to prevent further decrease, the NCTU-DPWE research centre conducts studies. Relevant results gained so far are given below.

Yang et al. (2008) concluded that landslide mass is the most important source of sediment that flow into the Shihmen Reservoir, far ahead of the share due to river erosion. To quantify the inflow of sediments in the reservoir per year or per typhoon event, NCTU-DPWE set up a landslide model which can map potential landslide locations and predict volumes that drain into the river under several rainfall scenarios.

Once the sediment is in the river system, the key-issue is to understand the transport of it in order to prevent sedimentation. Therefore NCTU-DPWE developed and tested a monitoring device based on TDR to measure the SSC. These studies were carried out by Chung and Lin (2011) and the technique is elaborated in the following section. This thesis will validate against the measured data from the TDR-monitoring system.

Based on observations from the field and the monitoring system it appeared that in severe typhoon events, the turbidity current reaches all the way to the dam, see figure 3.2. These observations eventually led to the transformation of one of the hydro-power turbines in the dam. In 2010 the turbine and its propeller were decoupled and a sediment sluice was created to release sediments. Its



Figure 3.2: Mud accumulated in the penstock after typhoon Aere (2004). Courtesy of Hsu (2013)

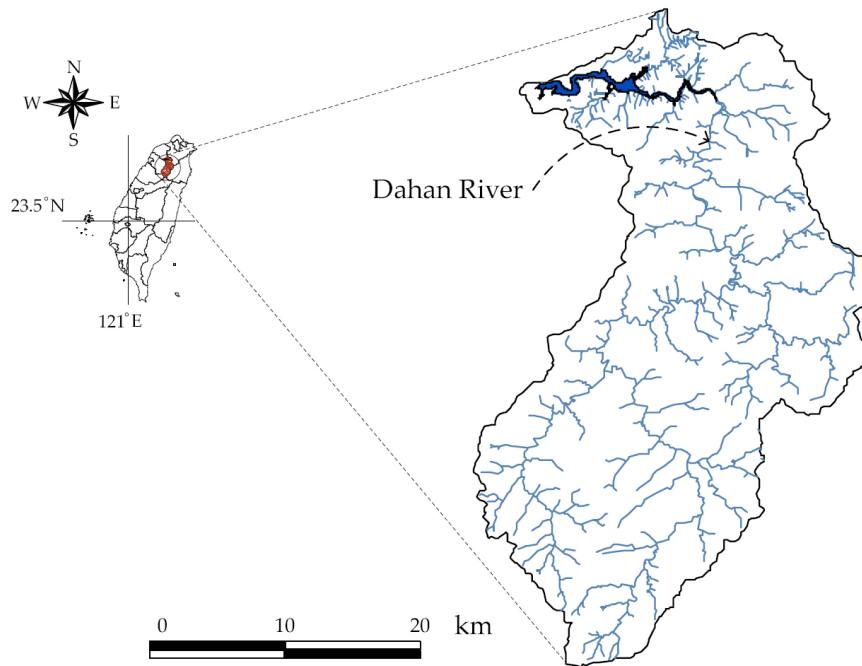


Figure 3.1: The location of the Shihmen Reservoir in Taiwan and its watershed, from Yang et al. (2014).

effectiveness has been reported by Yang et al. (2014) and is visually shown in figure 3.4. Figure 3.5 displays the ideas to implement two other sediment sluicing tunnels to the Shihmen Reservoir. An overview of all hydraulic structures that release water (possibly with suspended sediments) is given in table 3.1. Besides sluicing sediments, dredging is done on a daily base. Generally in reservoirs efforts to remove sediments from reservoirs are time consuming and dredging rates are low. It is an expensive option due to the special equipment that has to be acquired (as the reservoir is remote) and since the sediments are located deep under water. Furthermore, the soil of the Shihmen Reservoir consists mainly of silt and clay, which results in low dredging rates and fast wearing of the equipment.

The method of how the reservoir is operated determines the effectiveness of the sediment sluicing (Yang et al., 2014). The operations of the gate rely on the real-time SSC measurements by the TDR-monitoring system. At present the gates of the dam open once the turbidity current is recorded by the first TDR station, i.e. at cross section 32.

Table 3.1: Overview of the hydraulic structures in the Shihmen Reservoir, based on Hsu (2013).

Structure	Status	Diameter m	Elevation m	Capacity $\text{m}^3 \text{s}^{-1}$
PRO	Operational	1.3	174	33
Silt-sluice	Operational	3.6	174	300
Dawanping	Design phase	11	195	1600
Amuping	Feasibility study completed	8	236	
Spillway	Operational		235	11 400
Tunnel Spillway	Operational		220	1500
Water outtake	Operational		192.3	60

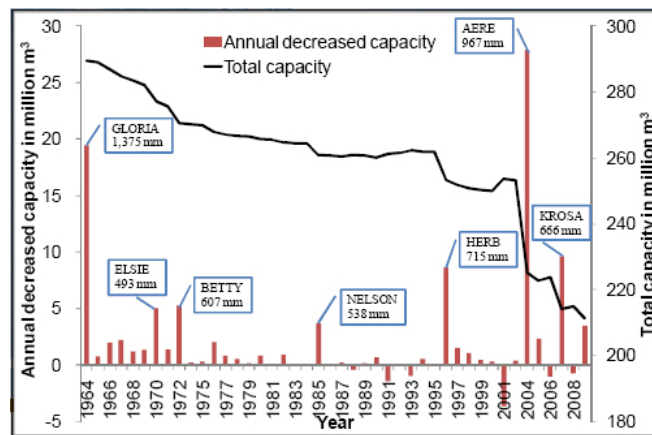


Figure 3.3: The total volume capacity of the Shihmen Reservoir versus several typhoons that generated turbidity currents which deposited material, from Hsu (2013).



Figure 3.4: Mud concentrated flow from the silt-slucice and PRO turbine outlets, photo taken from the top of the spillway. Courtesy of <http://www.wra.gov.tw/>.

3.2.2 Determining sediment characteristics

To parametrise the behaviour of the sediments found in the Shihmen Reservoir, three mud experiments were conducted. The set up used consisted of two 23.5 cm high water columns with a diameter of 50 mm, see figure 3.6. Mud samples from the bed of the Shihmen Reservoir were prepared with concentrations of 20 g l^{-1} , 40 g l^{-1} and 60 g l^{-1} . By gently mixing, the concentration was approximately uniformly distributed over the water column. With a photo-camera and back-light the settling of the front was recorded. The location of the front is shown in figure 3.7 for the hindered regime with a concentration of 40 g l^{-1} . Through the formula of Winterwerp (1999) (thus $m = 1$ in Eq. 2.40) the settling velocity w_{s0} and the volumetric concentration of flocs $\phi = c/c_{\text{gel}}$ were fitted

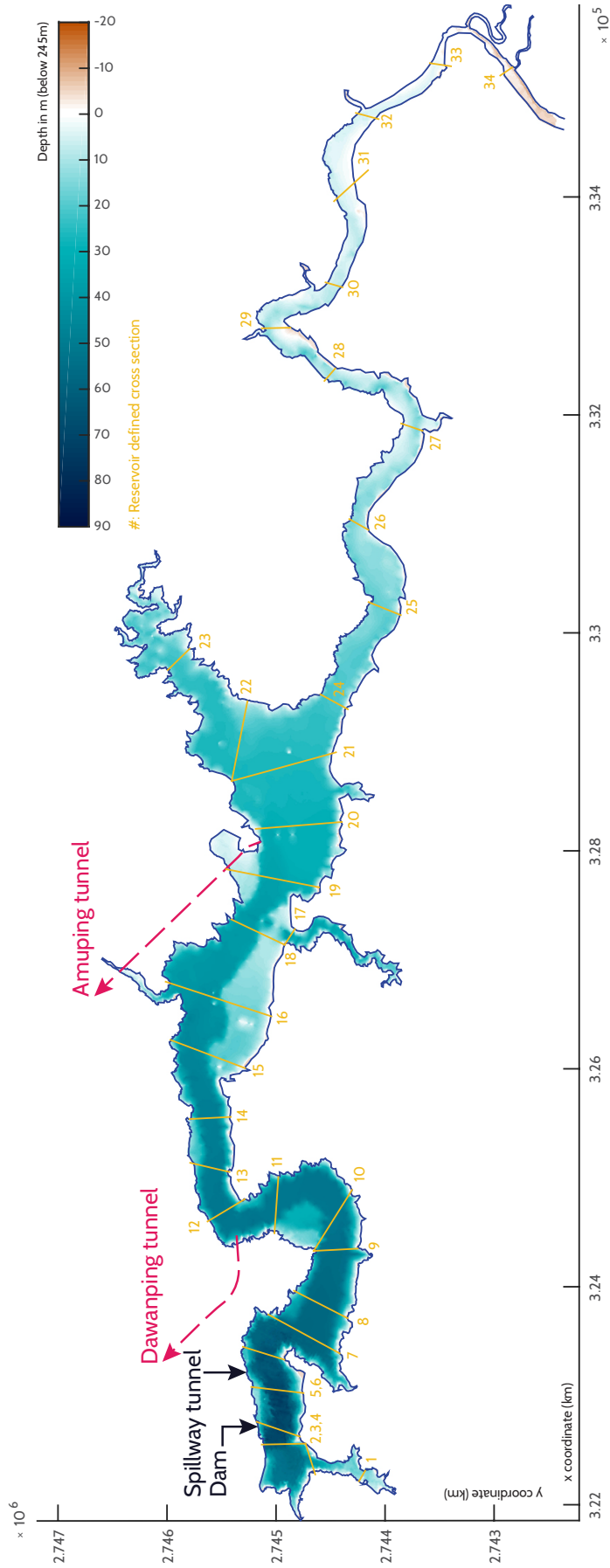


Figure 3.5: The Shihmen Reservoir with echo-sounded bed elevations (here expressed in depths) from 2013. Future plans to bypass the turbidity current from the reservoir are indicated with the dashed lines; the so-called Dawanping Silt-Sluice left and the Amuping tunnel right. An 'elephant nose' inlet is attached to the Dawanping tunnel in order to pick up the turbidity current at the lowest elevation possible. Note that the bed is generally smooth in cross sectional direction. Also note that the bottom is flat and wide in the area between cross sections 19 to 25 and 23.

through the three measurements. Obtained was:

$$w_{s0} = 2.27 \text{ mm s}^{-1} \text{ and } c_{\text{gel}} = 56.2 \text{ g l}^{-1} \quad (3.6)$$

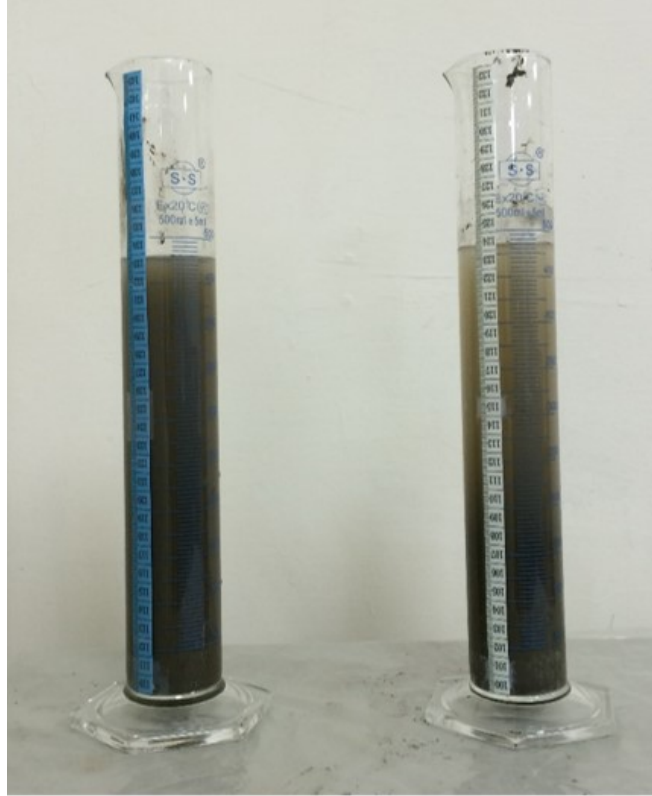


Figure 3.6: Experiment set up in which the mud characteristics were determined, January 2015.

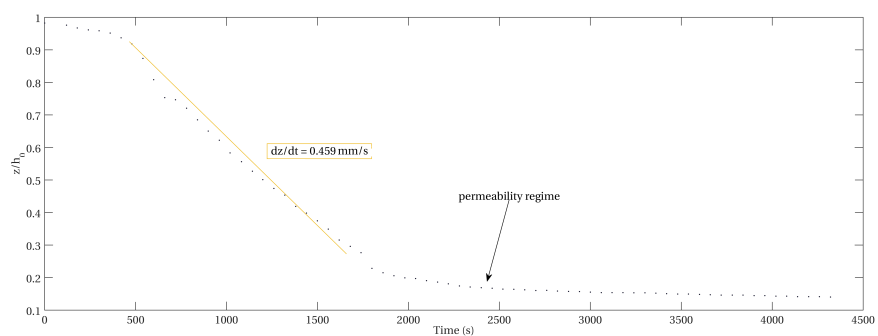


Figure 3.7: Hindered regime measured for $c = 40 \text{ g l}^{-1}$.

3.2.3 SSC monitoring using TDR

The Shihmen Reservoir is monitored by several TDR units. One of the floating TDRs is shown in figure 3.8. SSC is also monitored at the spillways, the water out-take and the sediment sluice with the TDR device. The time domain reflectometry (TDR) is an automated monitoring technique based on transmitting an electromagnetic pulse through a coaxial cable which is connected to a sensing waveguide. Figure 3.9 displays a typical set-up. The waveguide



Figure 3.8: One of the floating platforms in the Shihmen Reservoir where a TDR device is placed on, November 2014.

reflects the transmitted signal and the reflections are typical for the changes in characteristic impedance along the waveguide. The reflected signal can be used to measure, e.g., soil moisture content, electrical conductivity, water levels and displacement of the soils (for references see Chung and Lin (2011)). The TDR technique has been utilised since the 1930s for cable fault locating. In recent years, the TDR has been optimised to measure SSC in water systems. Generally SSC measuring techniques for fluvial environments are limited by having small measurement ranges, being dependent on the particle size or being too expensive or delicate. The TDR monitoring system is said to be robust and relatively acquirable for low expenses. It has been validated for SSC in the wide range of 2000 mg l^{-1} to $130\,000 \text{ mg l}^{-1}$ SSC and has a stated accuracy of 1500 mg l^{-1} (Chung & Lin, 2011). Furthermore, by connecting multiple TDR sensing waveguides to a TDR pulser, one can increase the temporal and spatial resolution.

To measure the SSC Chung and Lin (2011) developed the following method. The measured TDR travel time

$$\Delta\tau = t_0 + \Delta t = t_0 + \frac{2L}{c_l} \sqrt{\epsilon_a}, \quad (3.7)$$

$\Delta\tau$ in s, can be written as a function of the actual travel time Δt in s and time offset t_0 . See figure 3.9 for definitions. In Eq. 3.7 is L the 'electrical' length of the probe (which can be calibrated by taking measurements in the air), c_l the velocity of light and ϵ_a the apparent dielectric constant [-]. The latter is a material property that expresses the permittivity ratio between the material and vacuum. It appeared that ϵ_a could be expressed as a function of the dielectric constant of the sediment in suspension ϵ_{ss} and $\epsilon_w(T)$ the dielectric constant of water. $\epsilon_w(T)$ is dependent on the temperature and salinity, although the effect of salinity is absent in the Shihmen Reservoir. Under the assumption that the TDR device is in a two-phase medium, ϵ_a can be defined by

$$\epsilon_a = (1 - SS)\sqrt{\epsilon_w(T)} + SS \cdot \sqrt{\epsilon_{ss}}, \quad (3.8)$$

with SS being the volumetric sediment content in a range 0 to 1, SS can be predicted by the following equation:

$$SS \approx \frac{(\Delta\tau(T) - t_0) - \frac{2L}{c} \sqrt{\epsilon_w(T)}}{\frac{2L}{c} (\sqrt{\epsilon_{ss}} - \sqrt{\epsilon_w(T)})}. \quad (3.9)$$

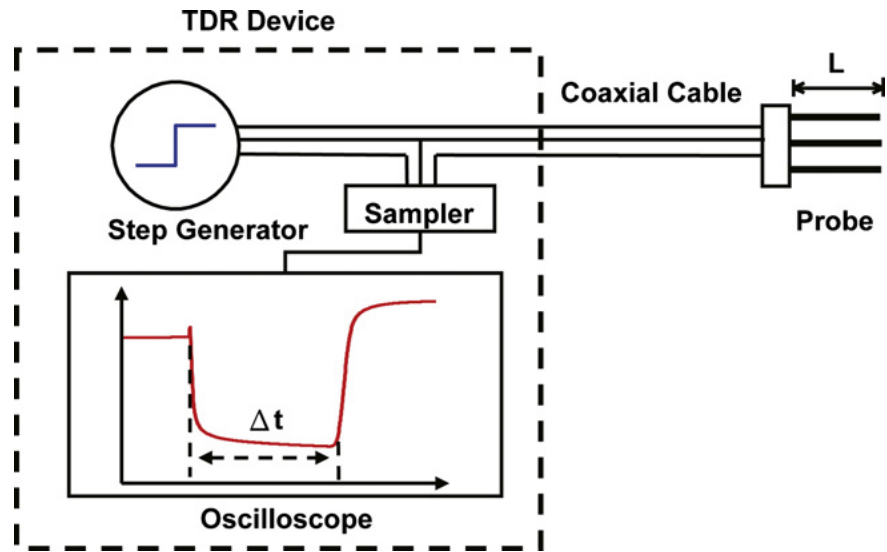


Figure 3.9: Typical set-up of a time domain reflectometry (TDR) system that can monitor suspended sediment concentrations (SSC). The TDR device consists of a pulse generator, a sampler and an optional oscilloscope. The transmission line consists of the coaxial cable and the waveguide (i.e. the probe) which is located in the medium. After Chung and Lin (2011).

Through calibration the values for ϵ_{SS} , t_0 and L can be found. The sensing waveguide and a temperature sensor can then be used to measure the TDR travel time Δt in the field and compute SS . To compute the density instead of the volume fraction, SS is multiplied by the specific gravity of the suspended sediment G_S [-];

$$c = \frac{SS \cdot G_S}{1 - SS} \cdot 10^3. \quad (3.10)$$

in which c is the concentration in g l^{-1} or, equivalent, kg m^{-3} . Negative concentration values were filtered out of the TDR data presented in this thesis.

While pre-processing the SSC data it was seen that some probes of the TDR registered SSC higher values than the probe below them. At first it was thought that density differences occurred due to temperature differences. This appeared not to be the cause as the temperatures measured could only induce differences in the order of 0.5 kg m^{-3} to 2.5 kg m^{-3} , which is well below the density differences measured by the probe, e.g., figures C.8 and C.10. By presenting the TDR data in these kind of contour plots, the non-physical density errors were easily discovered.

3.3 MODEL 1: 2DV FOLLOWING THE THALWEG

3D models are time consuming, both in the set up and in computing time. Therefore a 2DV model was made for the Shihmen Reservoir and used as a test case. The model follows the thalweg of the reservoir, as it was expected that the turbidity current would follow the deepest path in the reservoir. The model is 21 km long by 1 m wide and has several grid set ups, with grid size Δx ranging from 10 m to 200 m and 15 to 100 layers in the vertical. These settings, among flow conditions and others, were varied and tested in the sensitivity analyses. Figure 3.10 includes a schematic overview of the model. The model includes an Dirichlet discharge boundary at the right, a Dirichlet water level boundary at the left and a withdraw of water near the dam to simulate the tunnel spillway outlet. The dam itself is schematised as vertical layers that have zero velocity, thus, the

water can only flow in the upper layers of the model at the left boundary.

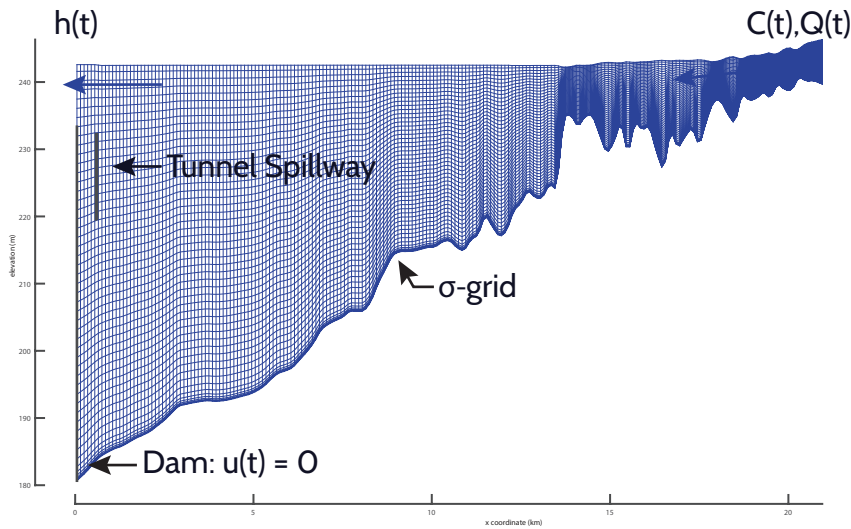


Figure 3.10: The 2DV numerical grid set up based on the thalweg of the Shihmen Reservoir. The grid displayed here has a logarithmic vertical profile with 50 layers and Δx is 200 m.

The thalweg was determined by using the least-cost search algorithm of Ehlschlaeger (1989). The algorithm is often applied to determine run-off patterns in watersheds. It finds the shortest route in the bed elevation data of 2008 from the highest point (upstream) to the lowest point in the reservoir (the bottom outlet in the dam). The thalweg was averaged to a 200 m grid resolution. In this way the bottom topography is kept constant while the grid size Δx is adjusted; computed variations in results are not caused by a change of resolution in bed topography.

3.4 MODEL 2: 3D HIGH RESOLUTION

The 3D-grid of the Shihmen Reservoir consists of 4598 grid cells horizontally and a σ -grid with 50 layers vertically. Grid sizes range from 14 m to 126 m and 13 m to 218 m for Δx and Δy , respectively. A top view is given in figure 3.11. A Dirichlet boundary condition was imposed at cross section 32 for both discharge $Q(t)$ as well as discharge of sediment concentration $C(t)$. The hydraulic structures (table 3.1) were implemented as withdraw points on the grid. Computationally, Delft3D handles hydraulic releases as a mass-subtraction in the continuity equation. The inlets were each uniformly divided over the σ layers corresponding to the elevation, determined at maximum water level (i.e. 245 m). The spillway at the dam was schematised equivalent to the 2DV model. Several monitoring points and cross sections were added to record matter such as suspended sediment transport quantities, flow velocities, SSC, water levels and others. The time step of the model was $\Delta t = 0.75$ s which let to a computational time equal to the physical time that was simulated.

3.5 MODEL EXPERIMENTS

3.5.1 2DV sensitivity analyses

A list of sensitivity analyses conducted is included in appendix B. A complete list of settings for the 2DV model can be found there as well.

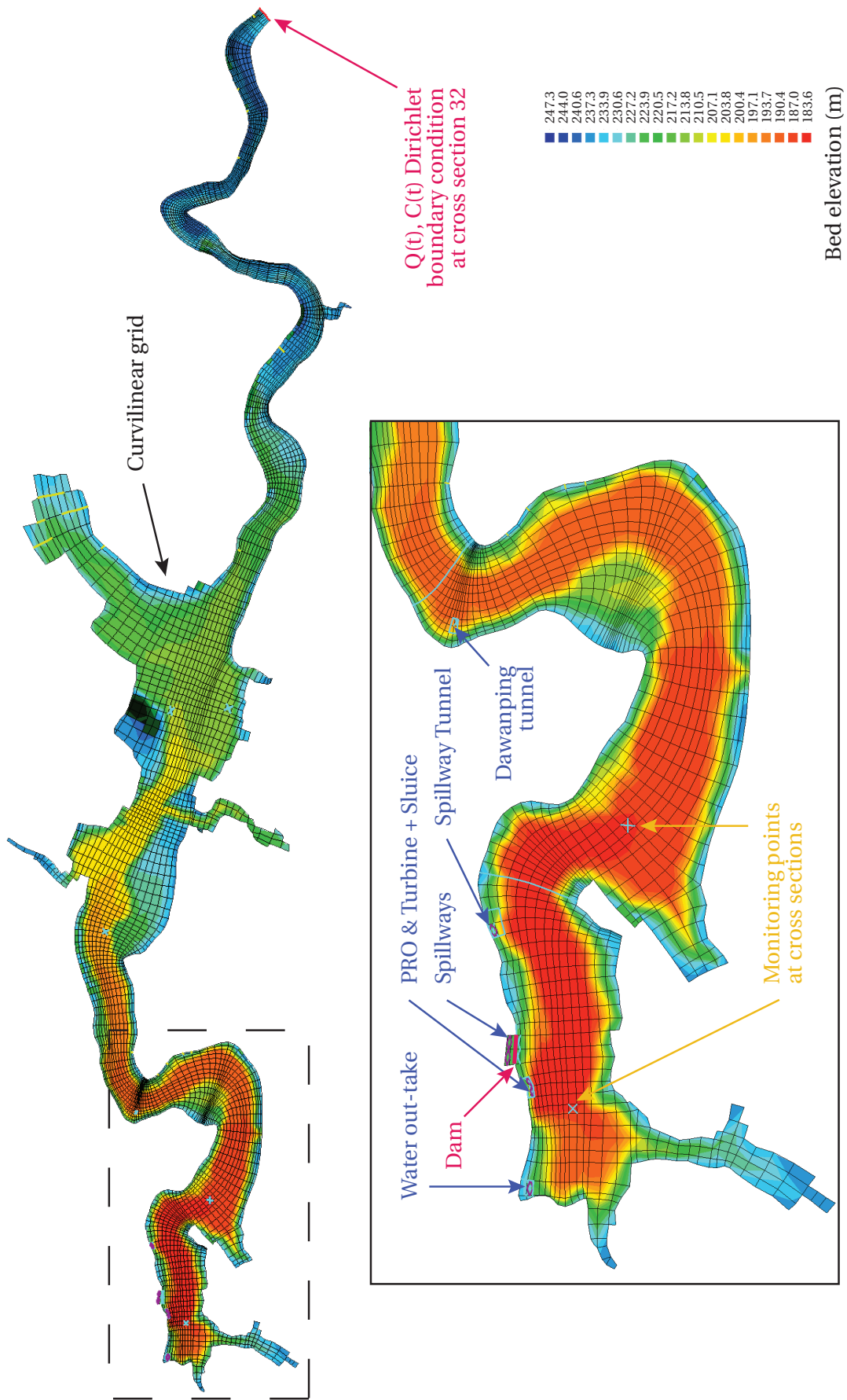


Figure 3.11: 3D curvilinear grid for the Shihmen reservoir.

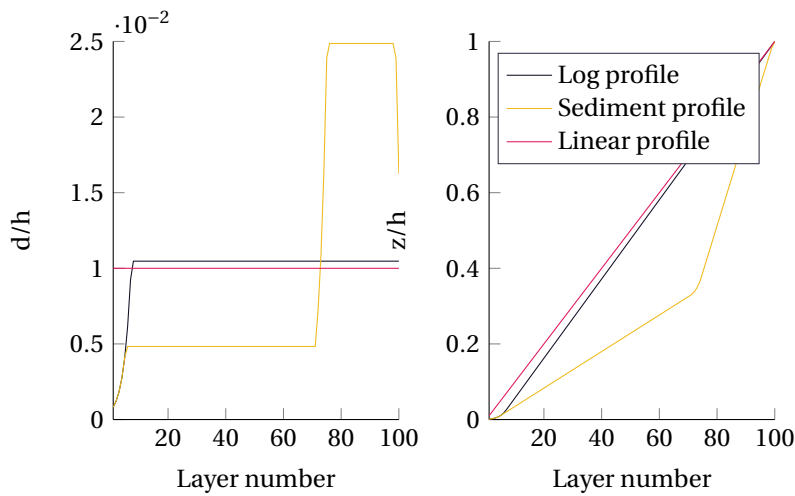


Figure 3.12: Three tested vertical profiles.

Each analysis was compared to one of the two reference simulation. Here the comparison was made for 1) the mean velocity of the turbidity current, 2) the mean velocity of the turbidity current after plunging, 3) the location of the plunge point and 4) the amount of deposit. Visually, vertical profiles were plotted for each analysis, plotted were the 1) density, 2) settling velocity, 3) gradient Richardson number, 4) flow velocity, 5) eddy viscosity and 6) turbulent quantity k . The vertical profiles were determined in the mid reservoir when the current hit the dam (i.e. when a concentration threshold at the cell next to the dam was reached). The location of determination varied during the grid-size Δx analyses, as it was preferred to determine the profile at the grid cell centre.

Vertically, three different σ -layering profiles were tested, they are shown in figure 3.12. The *log-layer* was finer near the bed where the *linear layer* was not. The *sediment layer* was finer near the bed, in the turbidity current and at the water surface.

3.5.2 3D simulations of Typhoon Soulik

The effects of typhoon Soulik¹, were simulated in the model of the Shihmen Reservoir. Inflow data from a weir upstream were used, as well as reservoir operation data provided by DPWE. The maximum hourly averaged peak discharge measured at cross section 32 was $5458 \text{ m}^3 \text{ s}^{-1}$ on the 13th of July. Typhoon Soulik was chosen because of these high flows and the fact that formation of a turbidity current was certain. During the typhoon event 4 TDR monitors were active in the reservoir and 7 monitors were recording SSC at the venting channels such as the sluicing tunnel and the spillways.

3.5.3 Valuing three practical solutions

Recap Eq. 1.1, the venting efficiency rate V_{eff} of the reservoir was defined as

$$V_{\text{eff}} = \frac{c_{\text{out}} \cdot Q_{\text{out}}}{c_{\text{in}} \cdot Q_{\text{in}}}, \quad (3.11)$$

and was used as the main indicator to value three practical implementations. The three were compared to the base case (defined as the calibrated model described in section 3.5.2). Each implementation had three distinguishable settings. An overview is given below.

¹Typhoon Soulik formed on 7th of July 2013 and dissipated on the 14th of July 2013

1. Blocking arm of the reservoir. A top view is given in figure 3.13. This can be thought as a small gravel elevation or possibly a double woven geo-textile spanned between the banks.
 - (a) A block up to elevation 220 m.
 - (b) A block up to elevation 225 m.
 - (c) A block up to elevation 230 m.

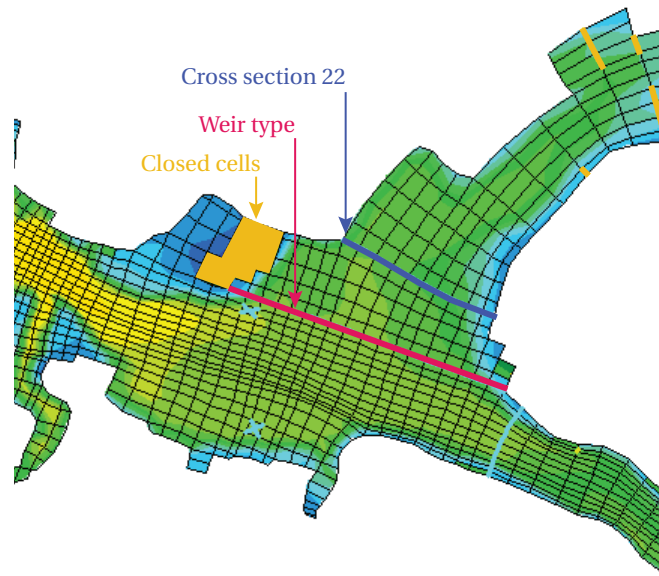


Figure 3.13: Scenario 1: top view of the grid with the weir blocking the arm.

2. Implementation of the Dawanping tunnel. The tunnel initiates sluicing on 13th of July 2013 at 7 AM, i.e. when SSC was measured in the vicinity of the tunnel (based on results presented later). The sluice latest closing time is at 15th of July 2013 closed at 3 AM i.e. when no significant SSC was measured near the tunnel (based on results presented later). Three cases were tested in which the tunnel discharge is varied. Here the total volume of water released through the spillway and tunnel spillway were redistributed according to three different cases.
 - (a) Replacement case wherein the Dawinping tunnel partially took over the role of the spillway and completely took over the role of the spillway tunnel.
 - (b) Constant case wherein the Dawanping tunnel was set to a constant discharge and the spillway tunnel was set to zero.
 - (c) Maximum case wherein the Dawinping tunnel released at maximum capacity for a short period and the spillway tunnel is set to zero.

The discharges set for the Dawanping tunnel are plotted in figure 3.14. For the latter two cases the water level would change with respect to the base case. Based on continuity, the expected water level was calculated beforehand (figure 3.15). In order to keep the water level below the maximum water level of the reservoir (245 m), the release through the spillway was adjusted accordingly (figure 3.16). In this figure the replacement case is equal to the maximum case.

3. Dredged trench to create a thalweg. From figure 3.5 can be seen that the reservoir has a flat bed topography. It was hypothesized that a trench

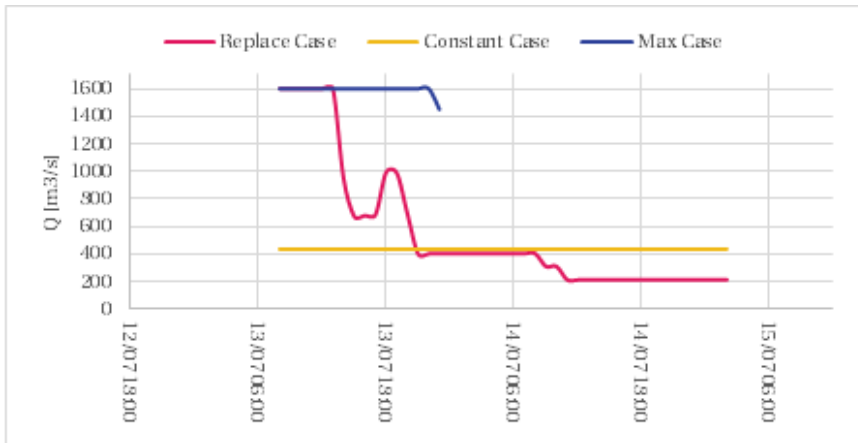


Figure 3.14: Scenario 2: discharges set for the Dawanping tunnel.

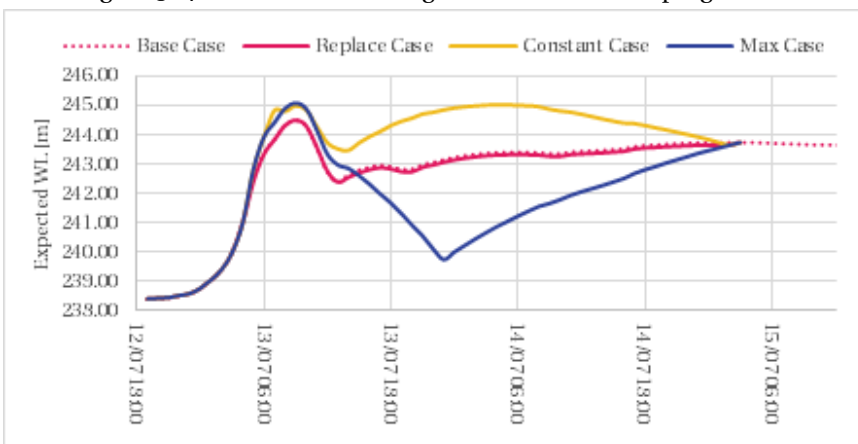


Figure 3.15: Scenario 2: expected water levels computed beforehand.

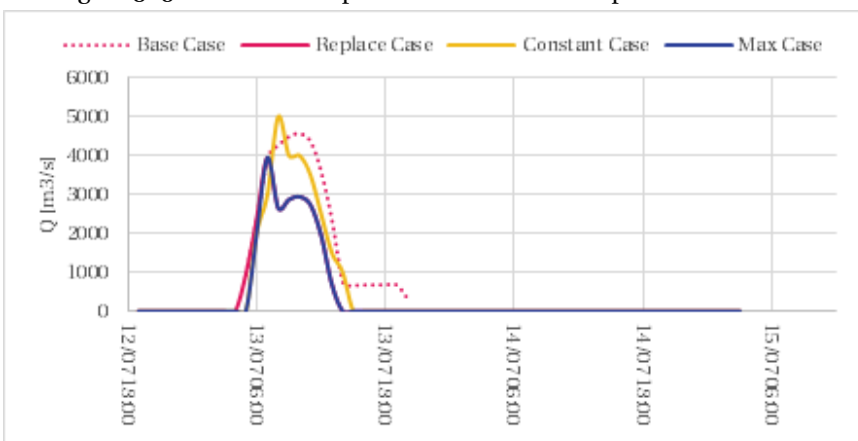


Figure 3.16: Scenario 2: discharges set for the spillway.

would attract higher concentration flows which would induce hindered settling. Therefore the sediment particles might stay mobile for a longer period of time. In these tests a set of trenches, approximately 100 m wide and 7.5 km long, were set in the middle of the flat bed with

- (a) a depth of 2.0 m;
- (b) a depth of 4.0 m; or
- (c) a depth of 6.0 m.

Volumes that had to be dredged were $1.52 \times 10^6 \text{ m}^3$, $3.05 \times 10^6 \text{ m}^3$ and $4.57 \times 10^6 \text{ m}^3$, respectively. The trench made is given in figure 3.17

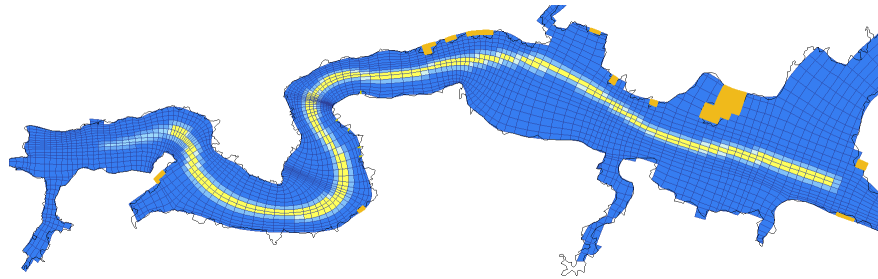


Figure 3.17: Scenario 3: trench dredged.

2DV Sensitivity Analyses

A summary of the sensitivity analyses is presented in this chapter. Appendix B holds a complete overview of results, including the vertical profiles versus the concentration, the settling velocity, the gradient Richardson number, the flow velocity, the turbulent eddy viscosity and the TKE.

Linking to the theory given before, high Richardson numbers occur around the lutocline. The TKE was damped accordingly and therefore the parabolic velocity profile derived earlier is seen from the bed to the lutocline. The velocity profile differs from the one given in sketch 2.1. The simulations show that the inner region (from the bed to where the velocity is maximum) is as high as the outer region (from the maximum velocity to where the velocity is zero) and not 5 to 10 times as high as stated before. However, the velocity and density profiles obtained are very similar to those found in the experiments of García (1993); the turbidity current has a low-velocity sub-critical turbid flow regime where as the sketch of figure 2.1 has a high-velocity super-critical flow regime. The high Richardson numbers that were seen in the simulation (i.e. the inverse of low internal Froude number) support this. The hydraulic jumps seen in the results are indeed features of these sub-critical flows. The jumps are induced by the bed topography (see, e.g. Kneller and Buckee (2000)).

It was seen that the behaviour of the turbidity current was sensitive to four parameters. [1] By increasing the grid size Δx the velocity of the turbidity current decreased and the plunge point retreated. The amount of deposit was the same. A larger grid size results in a loss of detail. Therefore the plunge point location was determined less accurately. However, where the plunging occurs is not much of interest. The change in velocity of the current and in the amount of deposit with larger grid sizes were acceptable. A grid size in the order of 100 m is therefore recommended. [2] Changing the roughness n led to a series of results. Less bed friction increases the velocity, decreases the amount of deposit, moves the plunge point further into the reservoir and decreases the height of the turbidity current. This is a sensitive parameter. [3] The amount of deposit increased strongly with a higher settling velocity w_s . The settling velocity had limited influence on the speed of the current, unless the turbidity current would dilute due to a very high settling velocity. [4] A lower gelling concentration c_{gel} results simply in a lower deposit and does not effect the height of the current.

The difference between the σ -grid, the σ -grid with σ -correction, the z -grid and the z -grid computing non-hydrostatic are not significantly. The velocities are more or less the same. Three main differences can be distinguished, see figure 4.1. The first is between the σ -grids and the z -grids where near the plunge point some local numerical diffusion is added in the σ -grid. The σ -correction cannot prevent this. The second lies in the area near the dam where the non-hydrostatic

computation predicts the height of the mixing above the lutocline lower than the other three. The last difference is the pointy waves in the σ -models near the spillway tunnel. These are not physical and origin from the mass subtraction in the continuity equation without subtraction of momentum. Nevertheless, the three minor differences are for now neglected.

The imposed sediment concentrations at the inflow boundary do matter. A higher value increased the velocity of the current and an increase on the deposited amount. Also the height of the current is less with a higher sediment concentration. All these effects can be reasoned, but it is important to conclude that the TDR device at cross section 32 is preferably of high accuracy as it determines the results for the complete model.

Finally a downscaled model was compared to the higher resolution model, see table 4.1 and compare figures 4.1 (top) and 4.3 (top). Approximately the two give the same result, except for the fact that the plunge point relocates (which is not much of interest), however, the computation time decreases by a factor of 100. Additional numerical diffusion by the σ -grid with respect to the coarser grid is minimal.

Table 4.1: Reference models.

	Reference 1	Reference 2	
Run	006z	028	
Δt	0.75	7.5	s
Δx	10	100	m
Layers	100	50	
Profile	LN-log	LN-log	
t_{comp}	8.5	0.08	h
\bar{u}	1.440	1.389	m/s
\bar{u}_{plunge}	1.181	1.133	m/s
x_{plunge}	12 750	12 100	m
Deposit	50.131	50.746	10^3 kg

Other results seen were:

1. Time step. At Courant numbers¹ between 1.5 to 3 (and greater) the simulation became unstable. Compared to the smallest time step, the velocity of the turbidity slightly decreased with larger time steps.
2. The non-hydrostatic computation. Here the vertical velocities differ only at the head of the current and effects are negligible near the plunge point. Moreover, with use of a larger grid size the spreading of the vertical differences will be averaged over the larger cell. At the head a positive non-hydrostatic pressure is followed by an under-pressure. The magnitudes were however small, in the order of 1 N m^{-2} . Figure 4.2 does show the waves between the dam and the spillway tunnel as mentioned before, although these are minimal.
3. Turbulent background viscosities and diffusivities. For very (unrealistically) high values the velocity of the turbidity current decreased, otherwise the background values did not have any significant influence. An example of the effect of increased eddy diffusivity is given in figure 4.3. Herein the Ozmidov length scale was increased considerably, which implies an increase of vertical momentum and mass and therefore lower Richardson numbers and a less sharp lutocline.

¹The courant number is defined as $\sigma = u\Delta t/\Delta x$ with u being the flow velocity at the river upstream.

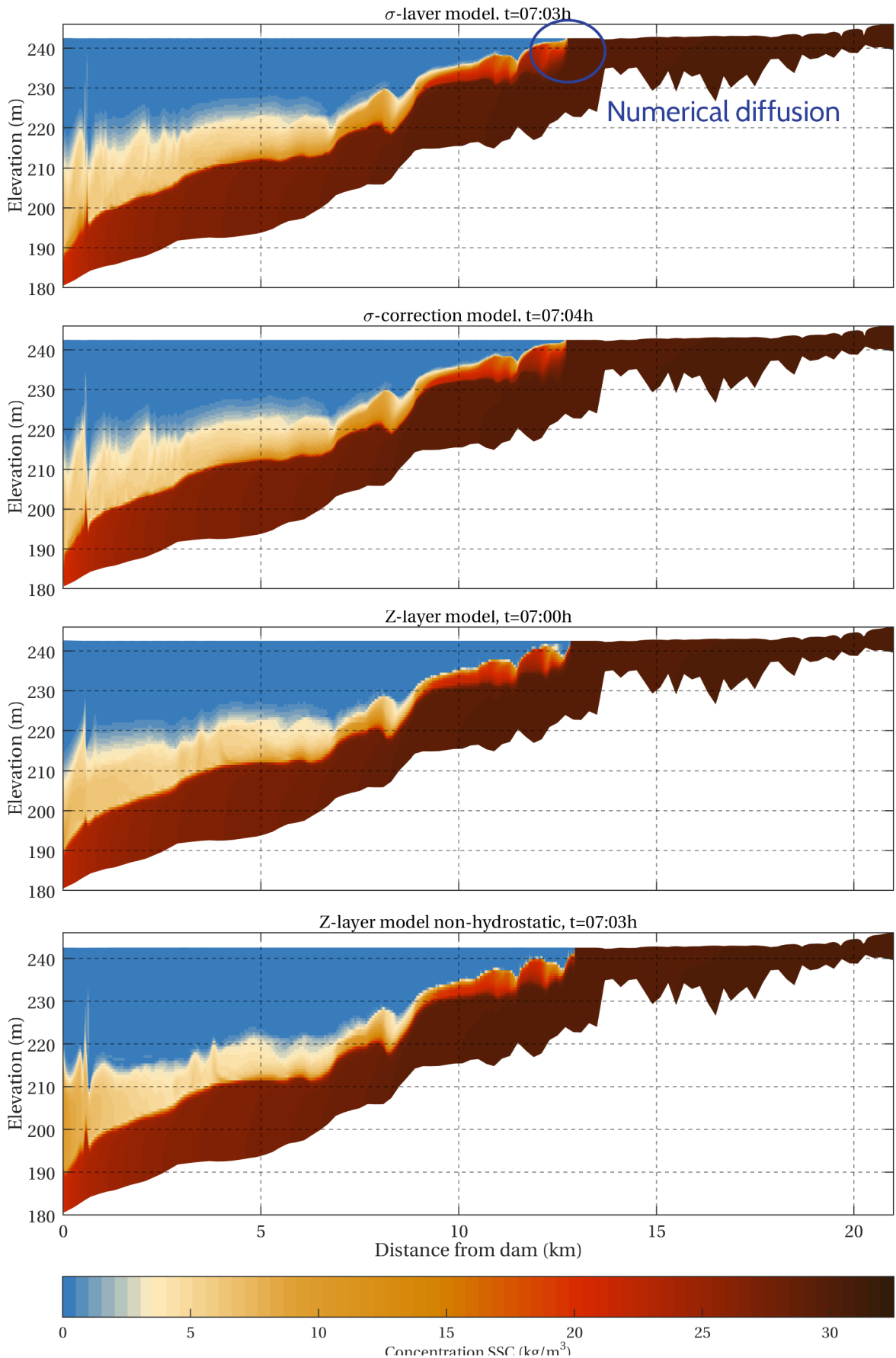


Figure 4.1: Fine horizontal grid ($\Delta x = 10$ m) with different vertical grids: σ -grid (above), σ -grid with σ -correction filter (second from above), z -grid (third from above) and z -grid non-hydrostatic (below).

4. Specific density and dry bed density of the sediment. These had no significant influence.
5. The vertical grids that were finer near the bed, i.e. the log-profile and the sediment-profile, gave more detailed velocity profiles near the bed and were therefore more accurate in computing the bed shear stresses. The log-profile and the sediment-profile quantitatively not show better results for one over the other.
6. A lower initial water level increases the velocity of the turbidity current (after plunging) and results in slightly less sedimentation. By dropping the water level during the test, even higher velocities are obtained and less sedimentation.

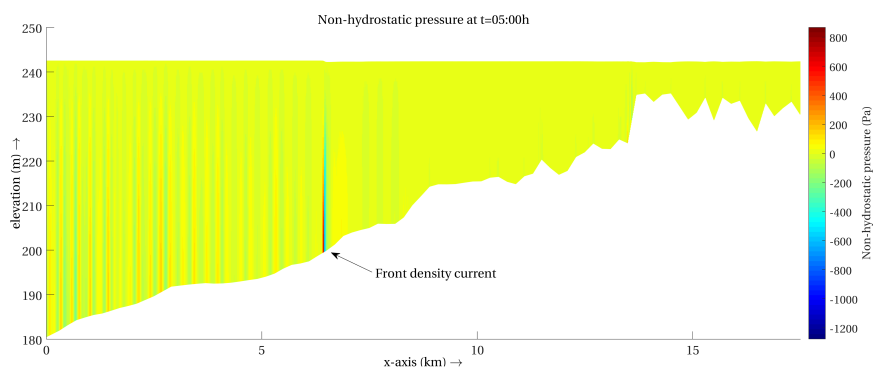


Figure 4.2: Non-hydrostatic pressure.

Note on the method applied

Generally, the procedure of determining the vertical profiles (appendix B) was not exact. The method is based on an Eulerian point of view. It is cumbersome to compare two vertical profiles of two turbidity currents that differ in propagation speed. It comes down to the frequency with which one stores the results (here 1 min). A high frequency would imply a more sound comparison, however, the frequency is limited by the (huge) amount of data collected during a run.

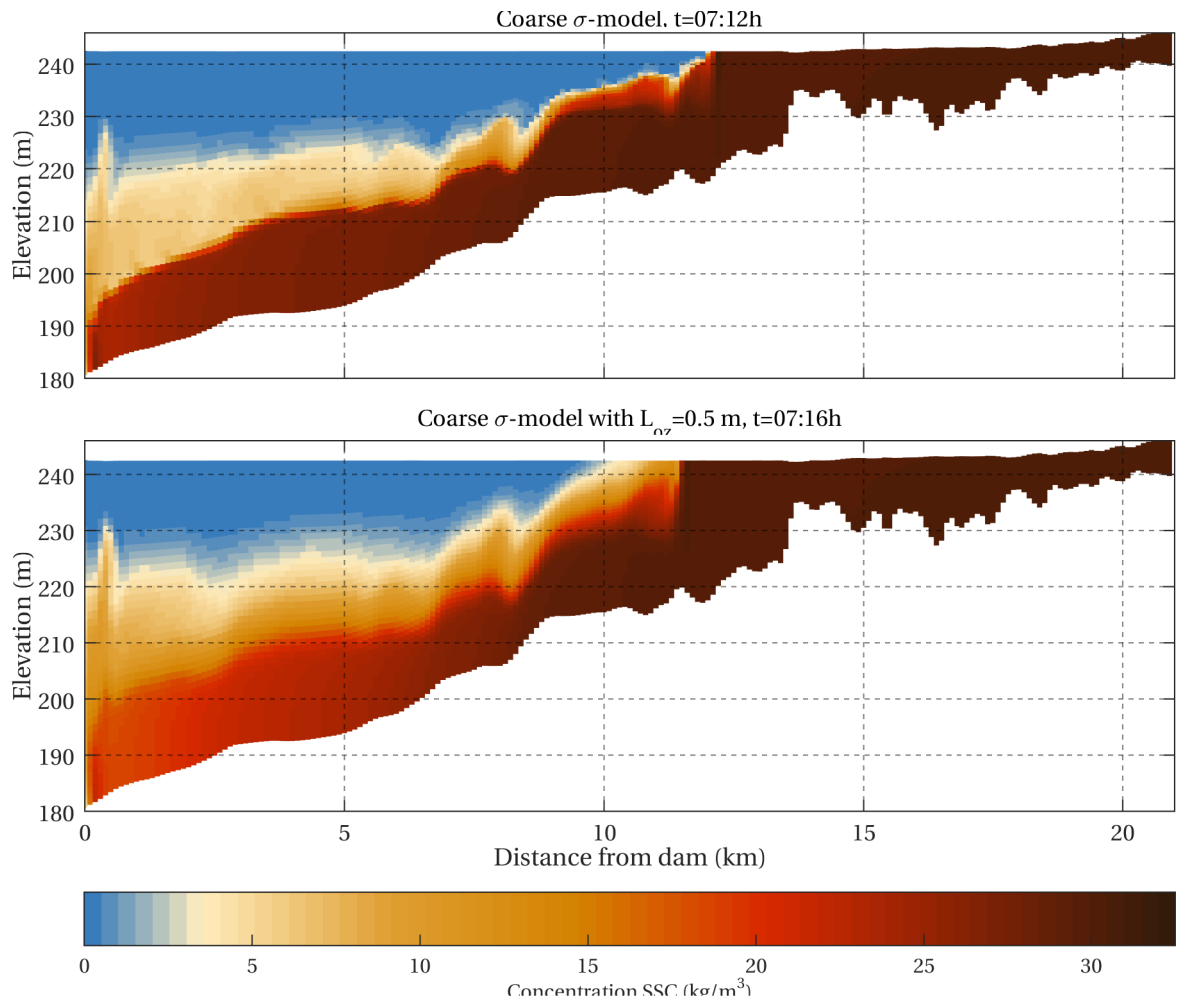


Figure 4.3: Coarse horizontal grid ($\Delta x = 100$ m) without any additional eddy diffusivity (above) and the same grid with an applied Ozmidov length scale of 5 m (below).

5

3D Simulations of Typhoon Soulik (2013)

To give the reader an impression of the simulated turbidity current, a time sequence is given in figures 5.1 and 5.2. It is seen that a concentration flow of approximately 60 kg m^{-3} enters the reservoir, forms a turbidity current and diverges into a main flow and a part that accumulates in the arm of the reservoir. The main flow reaches the dam and, once the dam is hit, the turbidity current is reflected back (not shown). The turbidity current itself dies while a large pool of sediments is formed in which the sediments slowly settle out.

The model was calibrated first against the TDR measurements. The settling velocity, gelling concentration and Manning coefficient were set to $w_s = 2.5 \text{ mm s}^{-1}$, $c_{gel} = 70 \text{ kg m}^{-3}$, and $n = 0.015 \text{ m}^{1/3} \text{ s}^{-1}$, respectively. The latter indicates a fairly smooth bed.

It must be noted that the σ -correction was switched off in the simulations presented. The σ -correction induced wiggles in the water level once the turbidity current reflected at the dam. Figure 5.3 shows the magnitude of the bouncing water levels. The unstable water level induced artificial vertical velocities and thus mixing. Therefore the σ -correction was put off in the simulations discussed. A smooth and stable water surface was then obtained.

5.1 COMPARISON WITH TDR

The simulated results showed good comparison with the TDR-monitoring devices in the upper parts of the water column (consider the elevations above 215 m in figures 5.4 and 5.5). At the spillway an almost identical concentration match was made. Appendix C includes all measured TDR SSC versus the simulated concentrations. The timing of the model is in agreement with the measured values. Although the height of the current in the model is approximately 5 m higher than measured. Also the model over-predicts the concentration and shows a steeper concentration profile.

The model did not agree with the concentrations lower in the water column (consider the elevations below 215 m in figure 5.4 and 5.5). This was seen at cross-section 7 and the TDR devices at the PRO, sluicing tunnel and power outlet. The TDR recorded higher concentrations and for a longer period of time, approximately 2 days.

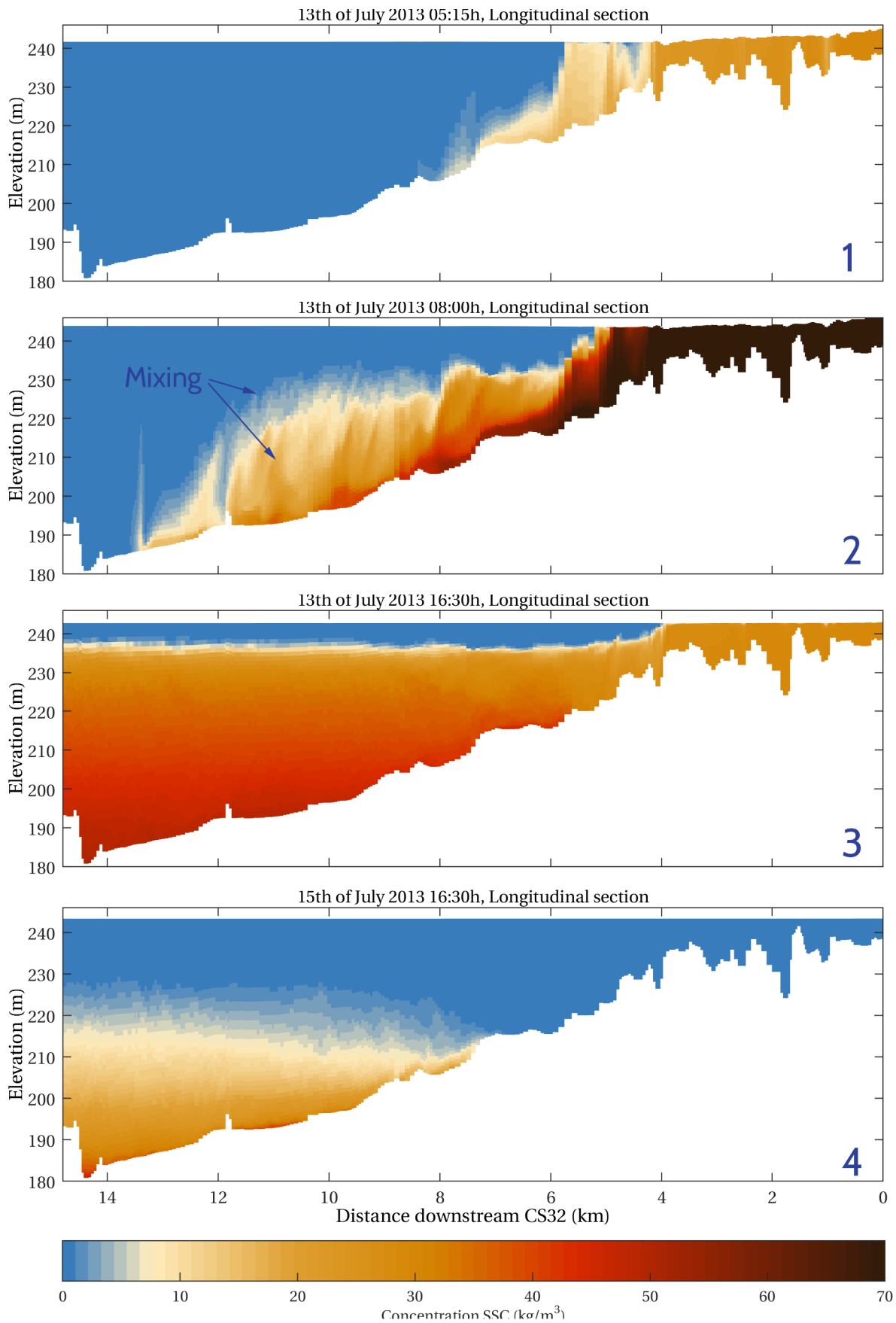


Figure 5.1: Simulated concentrations in approximately the middle of the reservoir.

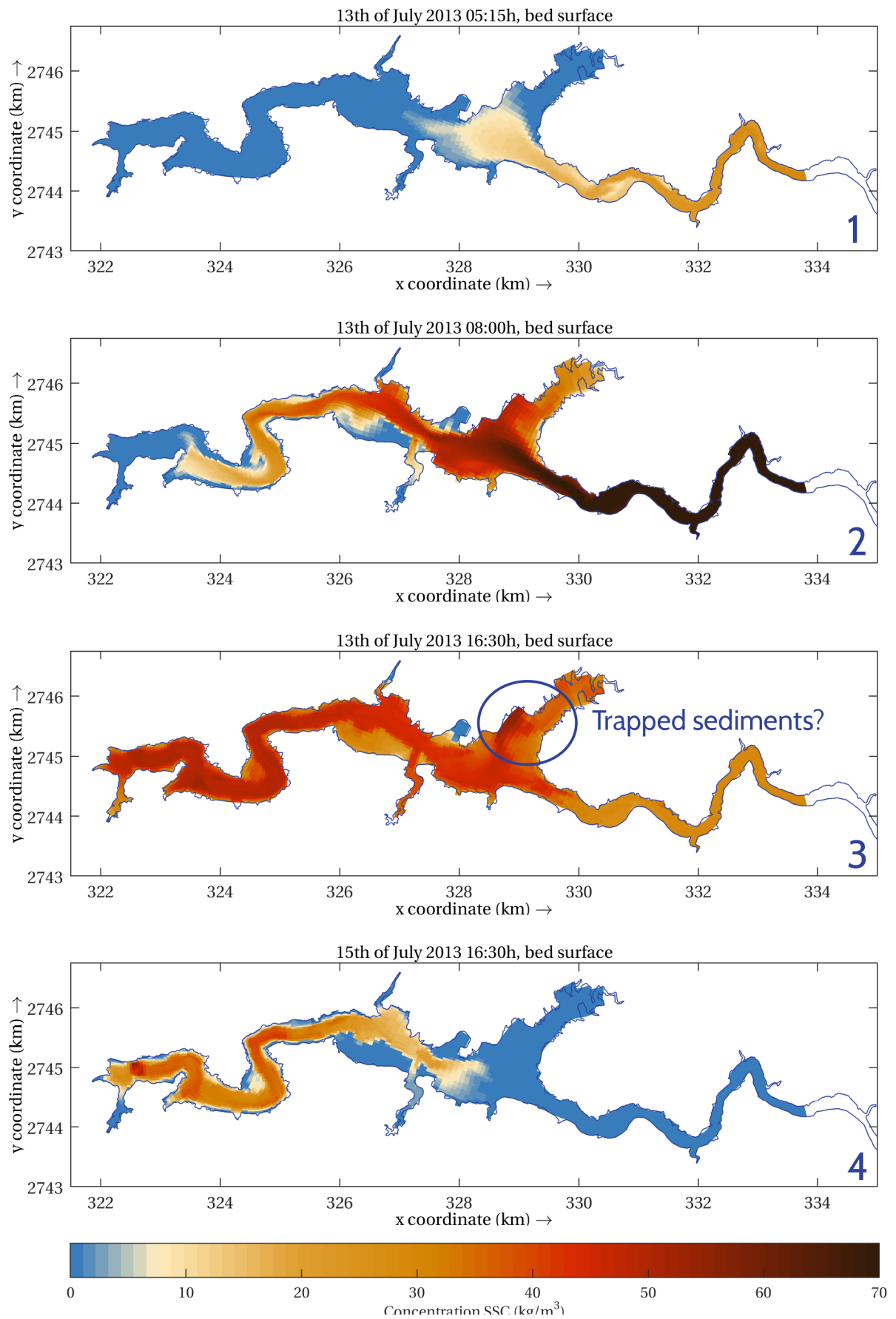


Figure 5.2: Simulated concentrations near the bed of the reservoir.

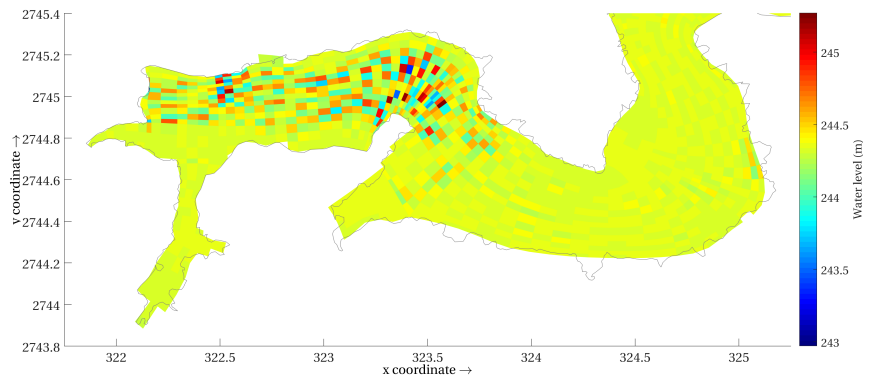


Figure 5.3: The σ -correction filter generated instabilities.

5.2 BEHAVIOUR OF THE TURBIDITY CURRENT

During the typhoon event the plunge location was modelled as a sharp horizontal interface, see figures 5.1 (2) and 5.6. The return current, induced by the plunging of the current, was computed as well. The highest concentrations were seen in the deepest parts of the reservoir, in particular near the sluicing tunnel at the dam and in the arm of the reservoir, see figure 5.2 (2).

Observing the turbidity current from the side showed that significant stirring occurred at the head of the current and in the following body (figure 5.1 (2)). Peaks emerged from the current into the water column alternated by low laid depressions. Small fore-running turbidity heads were seen in front of the major turbidity current. In the bends secondary flow effects within the current were seen, consider cross section 12 near the entrance of the future Dawanping tunnel (figure 5.7). The plot of the cross section also shows a not completely smooth interface between the low concentration front and the ambient water.

Another picture emerges after the typhoon event when all the sediments accumulated near the bed. The highest available masses near the bed were not recorded where the highest concentrations were located before. No accumulation was seen in the west part of the arm (figure 5.8). Material appeared to accumulate at the banks and other shallow areas of the reservoir.

5.3 VENTING EFFICIENCY

According to the simulation a venting efficiency of 21.3 % was achieved, see table 5.1. It is seen that the total vented mass through the bottom outlets is equal to the vented mass over the spillway. The tunnel spillway, that has its entry point lower than the spillway, slightly performs less than the two. The water out-take is included in the results since the concentration at this outlet should be as low as possible with respect to its purpose (irrigational water supply).

The SSC at the location of the future Dawanping tunnel were computed and given in 5.9. Sediments were recoded for approximately 2 days at this location with concentrations over 30 g l^{-1} . SSCs recorder at the TDRs in the low bottom outlets indicate the presence of sediments far longer than the floating TDRs monitors recorded (e.g., figure C.2).

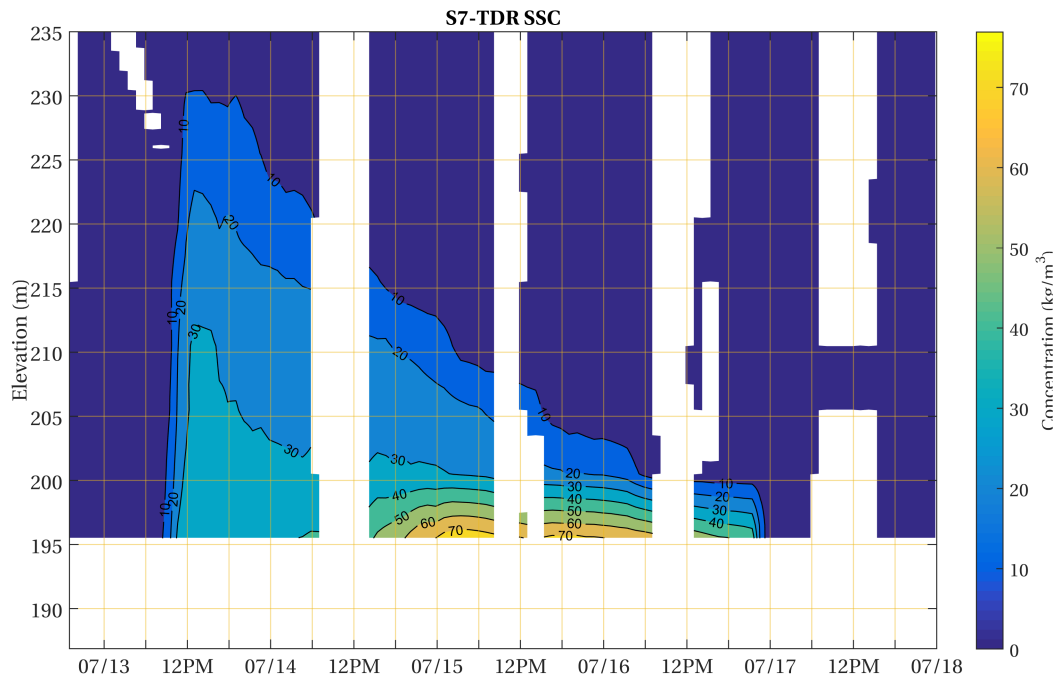


Figure 5.4: Measured SSC from the TDR at cross-section 7.

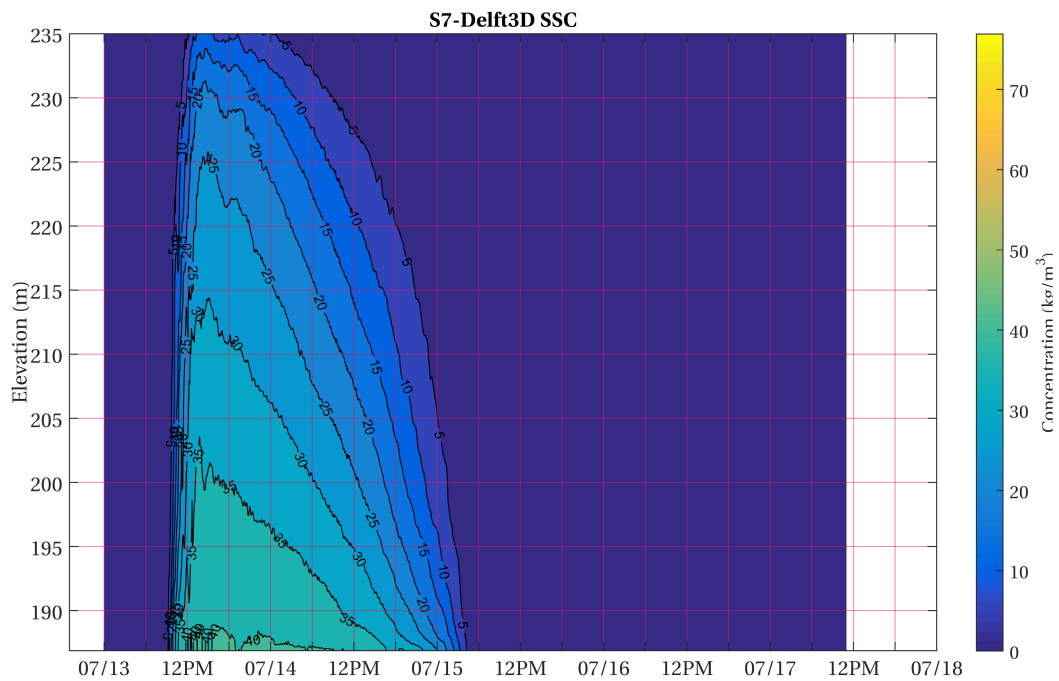


Figure 5.5: Simulated SSC by Delft3D at cross-section 7.

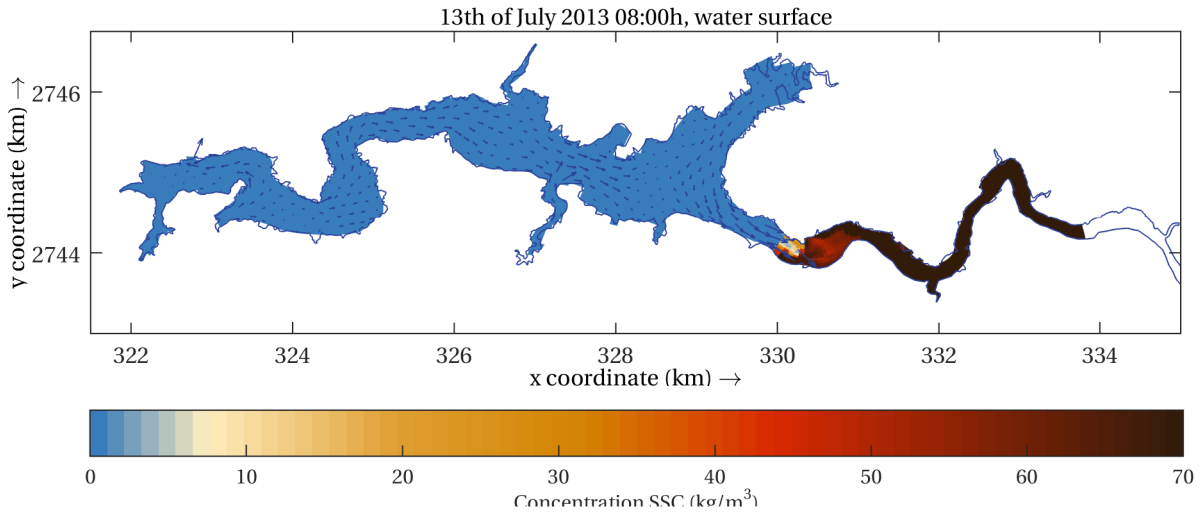


Figure 5.6: Water surface where the plunge point is visible as well as the return current.

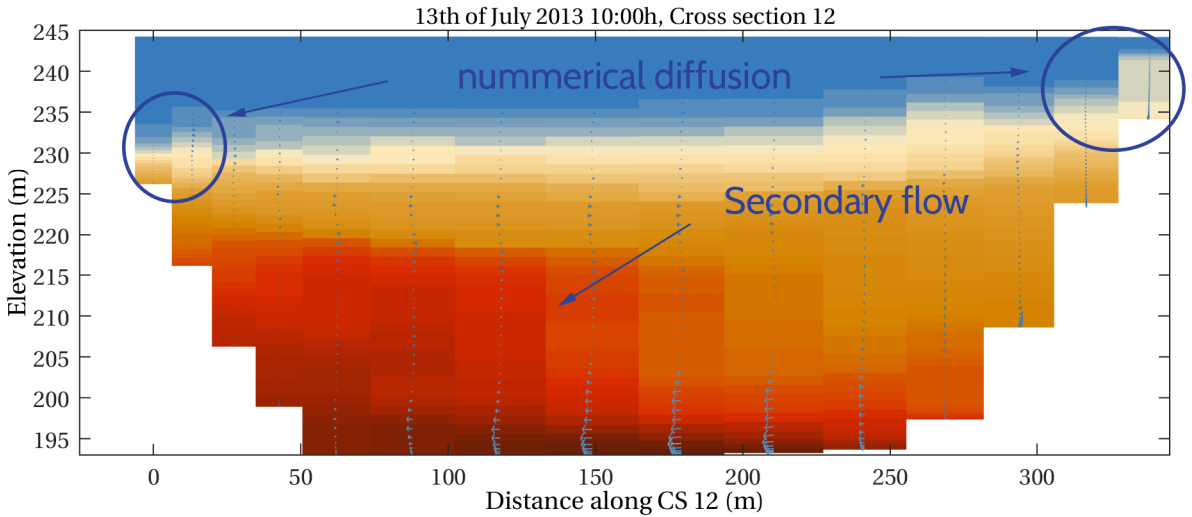


Figure 5.7: Cross section 12: secondary flow in the turbidity current and possibly cross sectional mixing induced by the σ -grid.

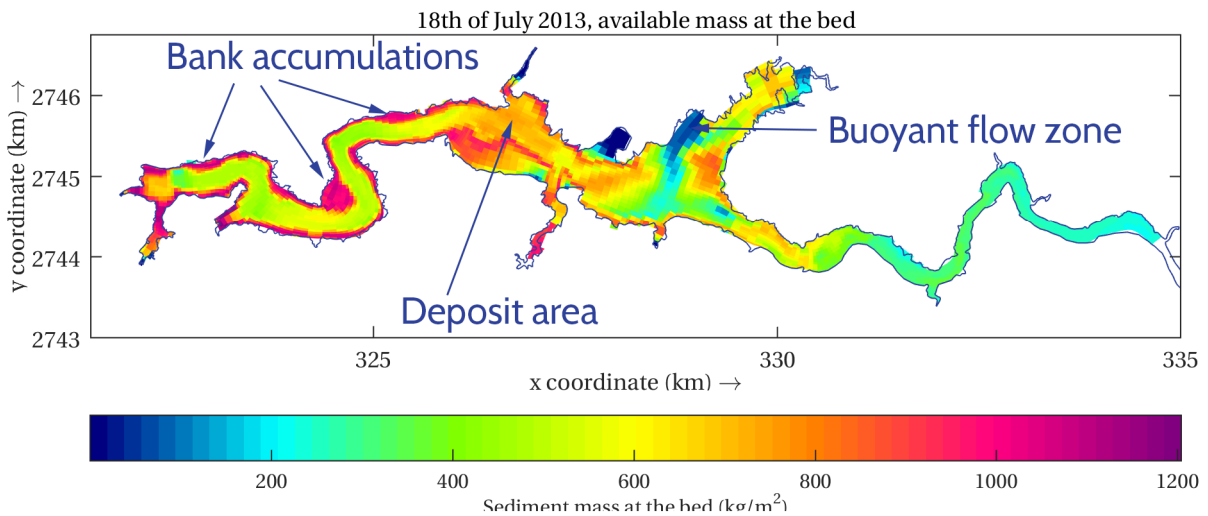


Figure 5.8: Sediment mass near the bed after typhoon Soulik. These sediments might still be in the permeability regime and therefore mobile.

Table 5.1: Computed venting efficiencies during typhoon Soulik (2013).

Location	Q_{tot} 10^7 m^3	$\bar{c} \cdot Q_{\text{tot}}$ 10^5 m^3	V_{eff} %
Cross-section 32	26.160	24.115	
PRO, turbine & sluice	3.846	1.875	7.78
Spillway tunnel	8.153	1.263	5.24
Water out-take	0.348	0.095	0.40
Spillway	12.673	1.899	7.88
			21.29

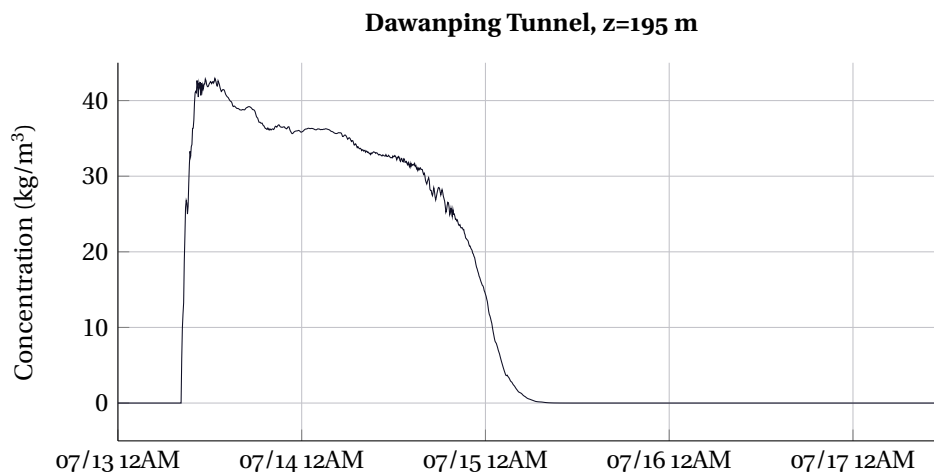


Figure 5.9: Delft3D SSC at the future Dawanping tunnel.

5.4 DISCUSSION

Comparison with TDR & venting efficiency

In the upper part of the water column satisfying model results were obtained while in the lower part of the water column the model was off. This can be explained by the fact that the model *does* include the hindered settling regime but *does not* take the permeability regime into account. According to the TDR device a significant amount of material rests at the bottom for several days. In the current model the settling velocity w_s goes to zero once the concentration reaches the gelling concentration. This explains good comparison with the TDR measurements at higher water elevations. After the hindered settling phase the model considers the sediments as deposited. In reality, however, the permeability phase starts and the material does not form a solid bed yet.

The presence of fluid mud near the sediment sluice and PRO is underpinned by the measured concentrations near the bottom outlets. From the TDR measurements it cannot be concluded whether the concentrations of 70 g l^{-1} in cross section 7 are the result of local formation of fluid mud or whether this high concentration originates from upstream and flew downstream over the bottom. Or possibly a combination of the two. Therefore TDRs should be installed close to the bed. In any case, the rheology of such a fluid formed, possibly does not behave as a Newtonian fluid. In that case the current Delft3D model should be extended to capture all sediment movements during and after a typhoon event.

For now it can be concluded that the venting efficiency at the bottom outlets is under predicted. This is confirmed by the findings of Yang et al. (2014). They found a venting efficiency of 35.1 % versus the 21.3 % predicted by the model.

The difference is directly related to the under predicted efficiency at the bottom outlets.

Mixing

Earlier, Slørdal (1997) reported that the σ -correction might lead to a systematic underestimation of the baroclinic pressure term. This would explain the wiggles seen during the σ -correction simulations. From numerical tests Slørdal (1997) concluded that the underestimation is reduced by increasing the vertical resolution, but is sometimes enhanced by increasing the horizontal resolution. However, this would severely increase the computing time. In the 2DV sensitivity analyses it was seen that the σ -grid did not significantly introduce numerical mixing compared to the z -grid. Cross section 12 in figure 5.7 indicate that the combination of steep banks and the σ -grid applied introduce numerical diffusion. Therefore it is of interest to compare the 3D σ -model with an equivalent 3D z -model.

Referring to the main turbidity flow in longitudinal direction however, it is unknown whether the mixing seen in figure 5.1 is a valid and sound physical representation or numerically introduced. The numerical diffusion might be due to longitudinal effects, which were negligible in the 2DV case, or implicitly by cross sectional effects as seen in figure 5.7. Comparison with the TDR devices (figures 5.4 and 5.5) do show that the model computed the turbidity current indeed too high, although this cannot be directly addressed to numerical diffusion. Concluded in the sensitivity analyses, the height of the current could also be increased by a too high roughness coefficient or sediment related parameters. Further calibration on those settings could improve the agreement on the height of the current with the measured values and possibly decrease the amount of mixing.

Continuing on calibration, one should keep in mind that the $k - \epsilon$ model is set with default coefficients. If the roughness and sediment related parameters make no difference, one could consider calibrating the turbulence model, starting with the Prandtl-Schmidt numbers. Suggestion is made to acquire necessary data from flume or scale experiments first.

Observations of turbidity current behaviour

The fore-running concentrations seen at the head of the turbidity current are concentrations imposed at the upstream boundary at the start of the event. The TDR device at cross-section 32 recorded some pulses with low concentrations which propagate through the system.

The question rises why the areas where at first high SSCs were seen, contained at the end hardly any available mass of sediments near the bed and vice versa. It is reasoned that the higher concentration areas have lower settling velocities due to hindered settling. Thus the particles cannot deposit directly on the bed. Instead these sediments can still be vented out of the reservoir. By comparing the locations of the predicted mass near the bed with the initial bed levels of figure 3.5, it is seen that sediments accumulate on elevated areas, approximately 15 m to 45 m below the water level. Here, the concentrations are low and thus sediments settle faster and in higher rates. The extremely low water in the Shihmen reservoir during spring 2015, revealed under water deposits (figure 5.10). Furthermore, as can be seen from the cover of this thesis, the banks are full with clayey materials. These examples indicate that the model is correct.

However, there are three major exceptions on this general tendency: 1) the area west of the dam, 2) the area west in the arm (hereby called the 'buoyant flow zone') and 3) the area given by deposit in figure 5.8. The first is the result of low dynamic flow in that area, although, since the model did not take discharges

from tributaries into account, there might be some flow and accumulation might be less in reality. The second needs some explanation. A flow diagram and reasoning is given in figure 5.11. The third, and last, is caused partially by the dying tail of the turbidity current and later significantly fed by the released sediments from the buoyant flow zone. Those sediments eventually accumulate in the deposit area.

The results and reasoning on the sediment mass near the bed should be validated against bed level records. Or, at least a decent sensitivity analysis on the settling velocity and gelling concentration in the 3D model should be conducted in order to provide weight to these findings.



Figure 5.10: Low water levels (2015) in the Shihmen reservoir. The simulated accretion can be seen with Google maps.

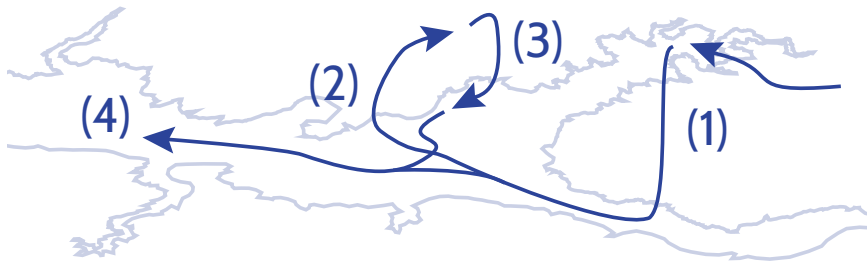


Figure 5.11: Explanation of the 'buoyant flow zone': (1) the turbidity current plunges and moves into the reservoir; (2) the turbidity current is diverted into a main stream and the a stream that flows into the buoyant flow zone; (3) the sediments are temporarily trapped in the zone and due to the high concentration settling hardly takes place, in the meantime concentrations in the main stream decrease and the turbidity current dies; (4) due to density differences, the sediments in buoyant flow zone start to flow downstream and eventually were not deposited in the zone.



Increasing the Venting Efficiency

In the model presented in the previous chapter three practical solutions are implemented in order to test their effect on the venting efficiency.

6.1 SCENARIO 1: BLOCKADE

According to the simulation results, a blocked arm does not have any significant effect on the venting efficiency. A slight increase in total mass vented through the spillway was seen, which were subtracted from the amount of mass at the spillway tunnel (table 6.1).

Suspended sediments were not removed from the system, however they moved to other places in the system compared to the normal Soulik simulation (figure 6.1). Blocking the arm till an elevation of 220 m decreased sedimentation in the arm. Those sediments accumulated in front of the blockade. By increasing the blocked elevation, i.e. 225 m and 230 m, depositions in the eastern part of the arm decreased. However, these sediments are now deposited in the western part of the arm. Furthermore, sedimentation at the banks of the reservoir were less at blocked elevations 225 m and 230 m. Those sediments partially spread out in front of the blockade.

Table 6.1: Scenario 1, blockade: venting efficiency results.

	Base	220 m	225 m	230 m	Unit
PRO, turbine & sluice	1.875	1.856	1.837	1.894	10^5 m^3
Spillway tunnel	1.263	1.209	1.093	1.046	10^5 m^3
Water out-take	0.096	0.093	0.087	0.087	10^5 m^3
Spillway	1.899	1.965	2.048	2.289	10^5 m^3
V_{eff}	21.29	21.24	21.00	22.05	%

6.2 SCENARIO 2: DAWANPING TUNNEL

Application of the Dawanping tunnel had a remarkable positive impact on the venting efficiency. The Max and Replace scenarios showed that the venting efficiency (nearly) doubled and the Constant scenario increased the venting efficiency with approximately 10 % (table 6.2). A positive result was also seen at the water out-take for both the Max case and the Replace case. Lower Nephelometric Turbidity Unit (NTU) values at this location is positive, pointing to the use of water for irrigational purposes.

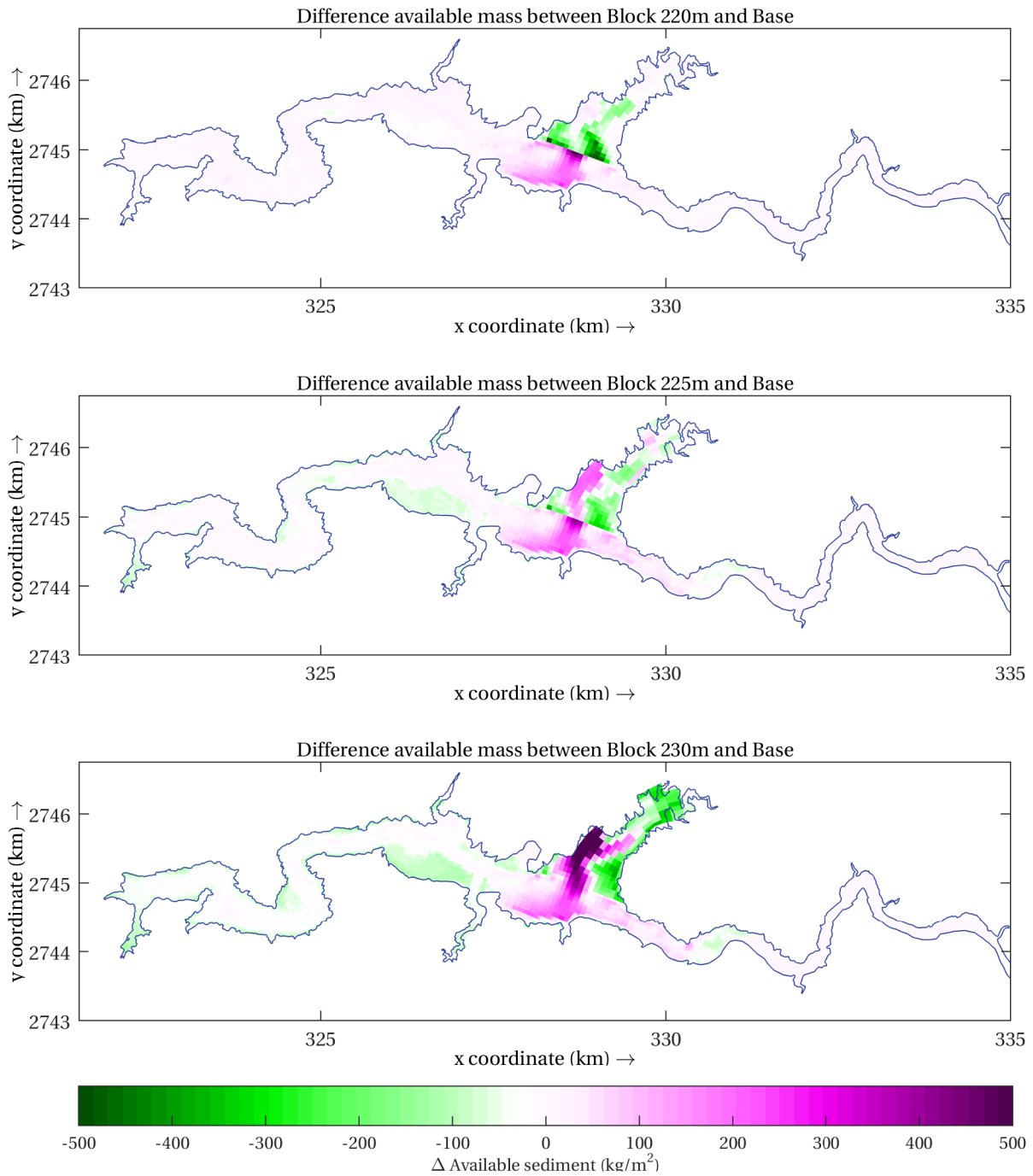


Figure 6.1: Difference of sediment mass near the bed between the Blocked arm till the elevation at 220 m, 225 m, 230 m and the original Soulik simulation.

In all three cases sedimentation decreased significantly for the complete system (figure 6.2). Deposits were mainly less at the banks of the reservoir, while a slight increase in mass deposit was seen near the deep trail towards the dam.

Table 6.2: Scenario 2, Dawanping: venting efficiency results.

	Base	Replace	Constant	Max	Unit
PRO, turbine & sluice	1.875	1.415	1.613	1.344	10^5 m^3
Spillway tunnel	1.263	0.000	0.000	0.000	10^5 m^3
Water out-take	0.096	0.050	0.071	0.040	10^5 m^3
Spillway	1.899	0.382	0.953	0.366	10^5 m^3
Dawanping	0.000	7.553	5.199	8.854	10^5 m^3
V_{eff}	21.29	38.98	32.49	43.97	%

6.3 SCENARIO 3: OPTIMISED THALWEG

The simulation results show a declining trend in venting efficiency with increasing depth of the trench applied, although the results are not significant (table 6.3). The trenches appear to attract sediments which result in a decrease of deposits at the banks of the reservoir and in the arm but an increase at the trench itself (figure 6.3). This feature is amplified by an increasing trench depth. Mass vented through the spillway tunnel decreased while the mass vented over the spillway increased. The efficiency of the near bottom outlets, i.e. the sluicing tunnels, tend to decrease if a deeper trench is applied.

Table 6.3: Scenario 3, thalweg: venting efficiency results.

	Base	2 m	4 m	6 m	Unit
PRO, turbine & sluice	1.875	1.883	1.842	1.788	10^5 m^3
Spillway tunnel	1.263	1.143	1.011	0.960	10^5 m^3
Water out-take	0.096	0.088	0.084	0.077	10^5 m^3
Spillway	1.899	2.030	2.108	2.112	10^5 m^3
V_{eff}	21.29	21.33	20.92	20.48	%

6.4 DISCUSSION

Scenario 1: Blockade

Blocking the arm of the reservoir did not increase the overall venting efficiency, however, it led to a redistribution of the sediment mass. The increase of sediment deposits in the western part and the decrease in the eastern part of the arm can be explained based on the buoyant flow effect of figure 5.11; the blockade hinders both the incoming mass flow from the main stream and the outgoing mass flow driven by the buoyancy effect. Therefore sediments are more uniformly deposited in the arm than in the normal simulation of typhoon Soulik. Apparently the hindering caused by the blockade slows down the outgoing buoyant flow as well. Its deposits are now placed further upstream, i.e. in front of the blockade. It can be concluded that a blockade with an elevation of approximately 230 m (and higher) still allows sediments to enter the arm but eliminates the possibility for them to leave again.

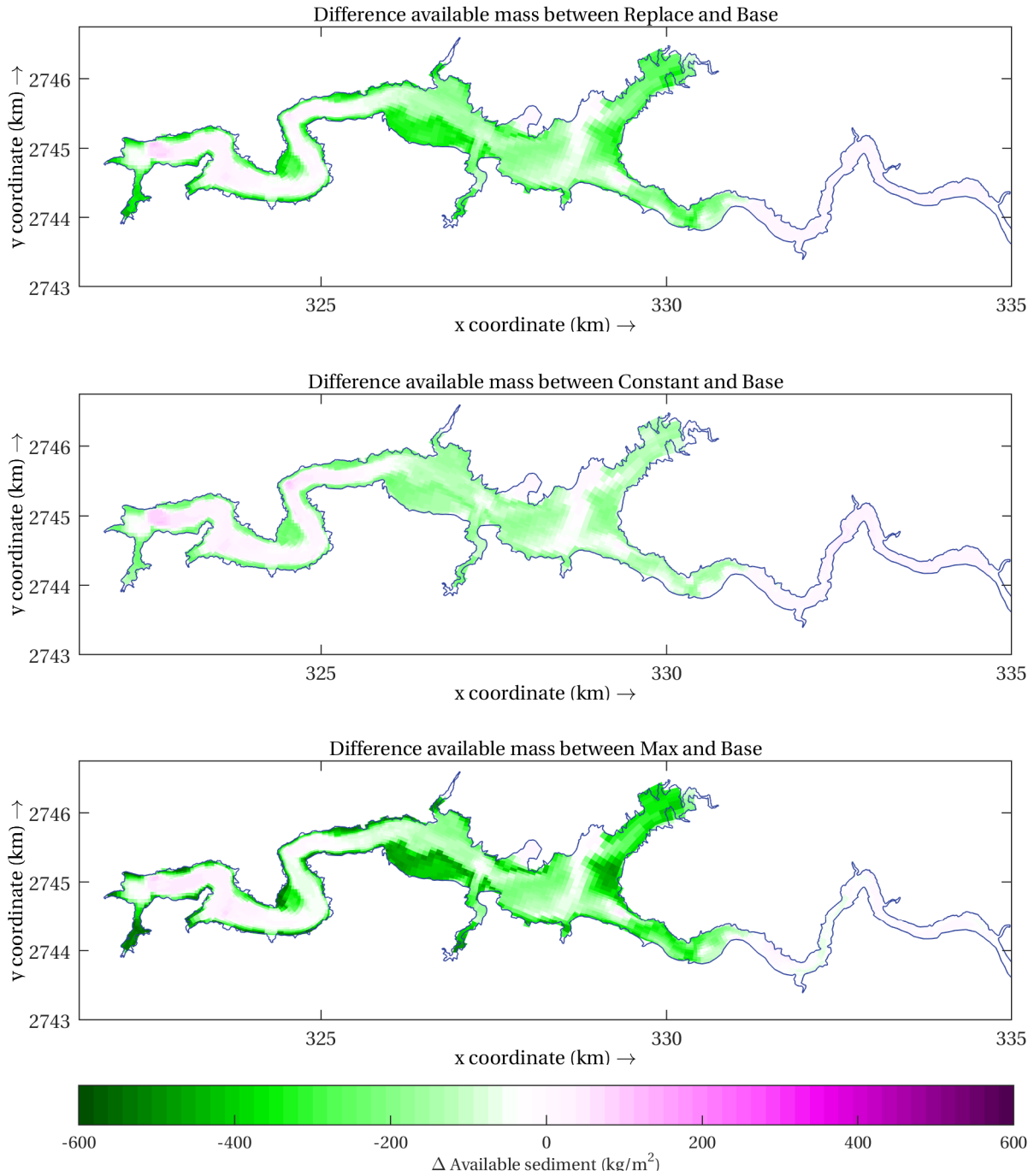


Figure 6.2: Difference of sediment mass near the bed between the replace, constant and max cases and the original Soulik simulation.

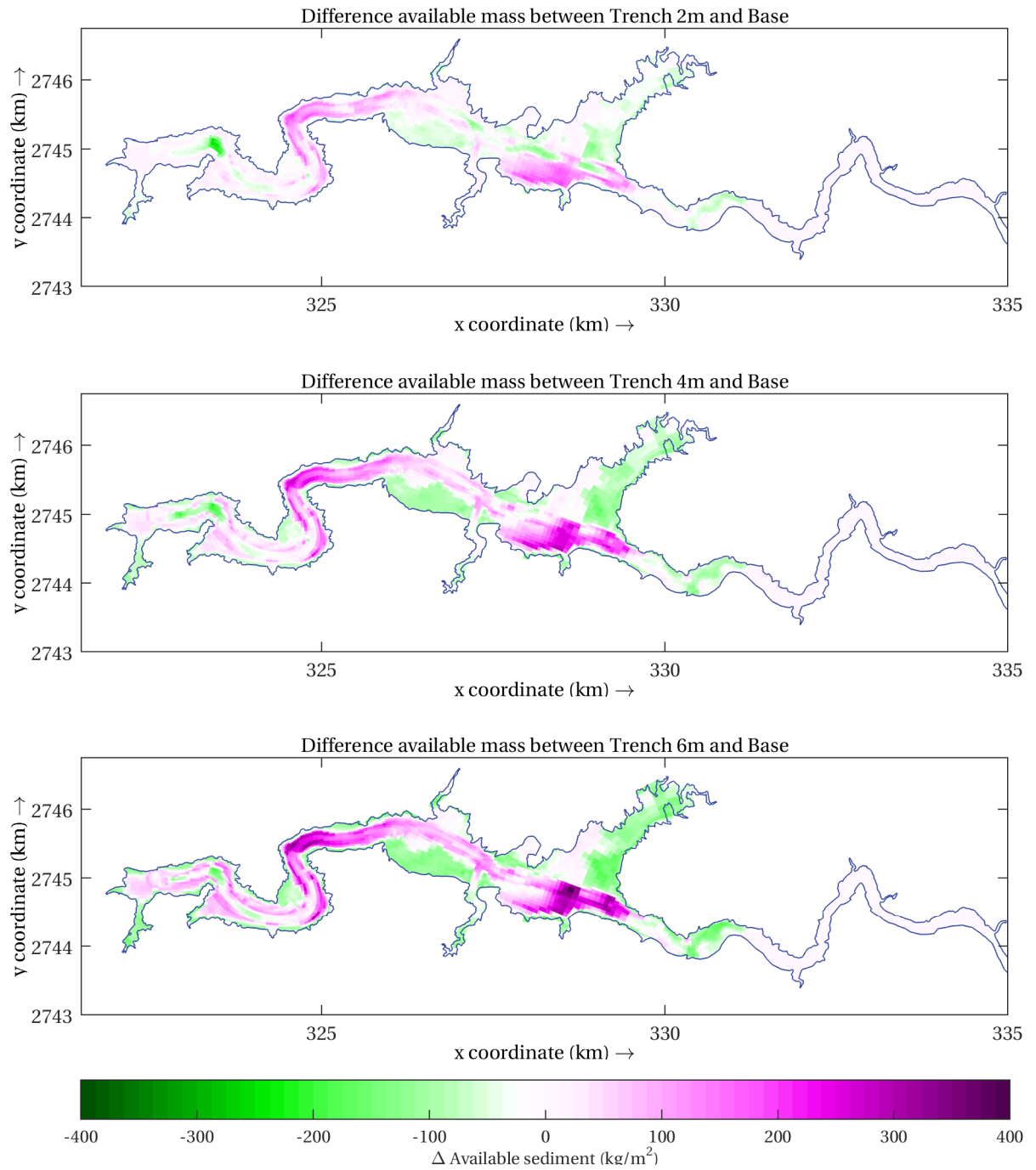


Figure 6.3: Difference of sediment mass near the bed between the Trench with a depth of 2 m, 4 m, 6 m and the original Soulik simulation.

The increase of total mass vented out through the spillway can be reasoned. Sediments not diverged into the arm, due to the blockade, are now forced into the main stream of the turbidity current. The spillway spills at the moment the main stream arrives at the dam and therefore sediments are vented by the spillway. The venting share of the other tunnels will be therefore lower.

Scenario 2: Dawanping tunnel

Two conclusions can be drawn based on the Dawanping simulations: 1) the location of a (new) sluicing tunnel is important and 2) reservoir operations matter.

The first is easiest explained by the Replace case in which the Dawanping tunnel overtakes a part of the spillway and the spillway tunnel. In this case, sediments are picked up further upstream (and thus in an earlier stage) compared to the original Soulik simulation. This has a positive and significant impact on the venting efficiency.

The second is seen in the difference between the other two simulations, the Max and Constant case. The Max case performs better than the Constant case which can partially be explained by the findings from the 2DV sensitivity analyses. There it was seen that a lower initial water level, or a water level drop, results in a higher velocity of the turbidity current and thus less deposit. At the Max case the water level is indeed abruptly lowered (see figure 3.15). Another cause of the higher efficiency seen at the Max case and not in the Constant case is the intensity (quantity) of sluicing.

It is suggested that additional venting schemes are simulated to come to the most optimal scheme. And, during the design phase of additional sluicing tunnels, a model such as the one presented here, should be used to determine the optimal location. In these type of simulation studies, the effect of timing should be included. In all three cases presented here, the Dawanping starts venting when SSC is measured at the TDR of cross section 12. It is expected that this is the ideal case, although, with respect to the water level in the reservoir and possible siltation effects downstream of the reservoir, this might not be the case. Complementing, the model presented does not include local entrainment effects of the turbidity current into the sluicing tunnel. One could consult the literature and knowledge from the dredging industry where slurry pick-up and transport through pipes is extensively researched.

Scenario 3: Optimised thalweg

According to the simulations an improved thalweg does not improve the venting efficiency and the performance of the applied trench was not in line with the expectations beforehand.

At the banks less sedimentation was seen because, by implementing a trench, the complete turbidity current is positioned lower in the water column. Therefore less sediments are mixed up in the water column to be deposited on the reservoir banks. Instead the sediments accumulate at the flat bed of the reservoir. This effect is enforced with deeper trenches.



Conclusions

At the beginning of this thesis it was questioned what practical solutions can be recommended to achieve a higher venting efficiency rate for turbidity currents in reservoirs. The objective formed was to value three of those practical solutions, namely: 1) blocking a part of the reservoir, 2) implementing an extra sediment sluice and 3) deepening the thalweg. Out of those three the additional bypass tunnel is recommended. The other two had no significant impact. Higher venting efficiencies were obtained with the new sluice since the turbidity current was picked up in an earlier stage compared to the remote bottom outlets at the dam. Therefore, the location of a bottom outlet in a reservoir is of importance. The venting efficiency doubles with the new sluicing tunnel, although the operations of the reservoir applied will be decisive for the actual efficiency.

The flow behaviour of turbidity currents in reservoirs as well as the prediction of where sediments accumulate appear not to be straightforward. As an example, it was seen that high SSCs do not explicitly mean high deposition rates at that specific location. And as was seen, a possible solution to decrease the sedimentation from a turbidity current may be counter-productive. The 3-dimensional RANS model used in this thesis proved to give valuable insight in these complex flow behaviours and scenarios.

Good agreements were found with the TDR monitoring system during the settling phase of the sediments, although the model slightly over-predicted the height of the current. Main parameters that should be calibrated while modelling turbidity currents in reservoirs, were found to be the settling velocity, the gelling concentration and the bed friction. The venting efficiency computed for the Shihmen case was under-predicted. This was caused by the fact that the model did not incorporate the complete settling process of the cohesive sediments. The permeability phase (fluid mud formation) and the consolidation phase were not included in the model. The TDR-monitoring devices suggested presence of fluid mud and the actual venting efficiencies of Yang et al. (2014) were therefore 14 % higher than the predictions made by the model.

Recommendations

Following the discussions and conclusions given in this thesis, the following recommendations are made:

- Make use of the method given and the results discussed in this thesis for studies after turbidity currents in reservoirs. A model such as presented gives valuable information about turbidity currents. The performance of reservoir operation schemes can be tested extensively as well as the implementation of additional reservoir outlets. Furthermore, such a model could also be used in a wider extent, e.g., to predict SSCs that are vented from the reservoir and cause environmental problems downstream.
- Extend the application range of the model by including the permeability regime of mud. An integrated model that could simulate the turbidity current as well as the first consolidation parts of mud would be superior. A more accurate venting efficiency could then be calculated for reservoirs that deal with turbidity current consisting of cohesives.
- Improve the accuracy of the model by calibrating and validating against bed topography data. Therefore it is suggested that typhoons of several years are computed as one long sequence and the computed bed topography is compared to the surveyed changes from the field.
- In order to decrease the computing time, it is suggested to test a 3D model with a coarser grid, e.g., one with 3 to 5 cells in the cross section. Such a model could be qualified against a high resolution model. Computations will become much faster and, coupled to landslide model of DPWE, it would be possible to make *real-time* predictions. Reservoir operations could then be optimised according to the actual flow conditions.
- In order to qualify the mixing processes seen above the lutocline, three suggestions for further studies are made. The first is to compare data from a physical model with the RANS model. It is expected that the diffusivity terms and possibly the turbulence model could be improved by means of calibration. Second is to simulate Typhoon Soulik with a z -grid to rule out numerical diffusion induced cross sectionally by the σ -grid. And the third is to acquire complete vertical SSC profiles of the Shihmen Reservoir to validate the lower regions of the model. Therefore additional TDRs should be installed near the bed.



Principles of Turbidity Currents

This appendix introduces the principles of a turbidity current following the lecture series of Parker (2007). In his series the comparison between a turbidity current and a better-imaginable river flow was made. Parker (2007) considers a control volume of water on a bed slope surrounded by air, as shown in figure A.1. The immersed weight of this control volume is:

$$W_{\text{imm}} = (\rho_w - \rho_{\text{atm}})gLA. \quad (\text{A.1})$$

Generally the density of air ($\rho_{\text{atm}} \cong 1.2 \text{ kgm}^{-3}$) is neglected as it is much smaller than the density of the water ($\rho_w \cong 1000 \text{ kgm}^{-3}$). Thus, the forcing of a non-turbid fluid flow in ambient air is:

$$F_{\text{river}} \cong \rho_w g LA \sin \alpha. \quad (\text{A.2})$$

Now a turbidity current is considered. It is a control volume of water turbid with sediment particles which flows under ambient water without any sediment particles. Here the density of the ambient fluid can no longer be neglected since the density of dilute sediment-laden water is a few percent more than the density of normal water, e.g., $\rho_t \cong 1030 \text{ kgm}^{-3}$. The forcing is:

$$F_{\text{turbidity}} = (\rho_t - \rho_w)gLA \sin \alpha, \quad (\text{A.3})$$

with the density of the sediment-laden water based on the concentration, i.e., $\rho_t = \rho(c_s)$. As sediments can be deposit or be entrained, the concentration will vary in time and space. This fact distinguishes turbidity currents from other density currents (driven by salt or temperature density differences) which do not have this density varying-feature. Concentrations in turbidity currents are in general dilute, i.e., $c \ll 1$.

$$\rho_t = \rho_w(1 - c) + \rho_s c = \rho_w(1 + Rc), \quad R = \frac{\rho_s}{\rho_w} \cong 1.65 \quad (\text{A.4})$$

To indicate, a turbidity current has only 1 % to 4 % of the driving force of a river which is carrying the same concentration of suspended sediment:

$$\frac{F_{\text{turbidity}}}{F_{\text{river}}} = \frac{\rho_t - \rho_w}{\rho_w - \rho_{\text{atm}}} \cong Rc \ll 1. \quad (\text{A.5})$$

As concluded by Parker (2007), the important difference between normal river flows and turbidity currents are:

- a river flows under air with a density ρ_{atm} , which is negligible in most cases (apart from air induced shear stresses, i.e. wind forcing);

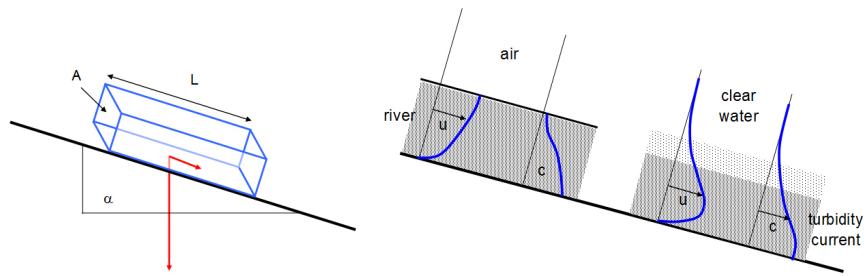


Figure A.1: A control volume of (turbid) water under a slope, from Parker (2007). Figure A.2: Velocity and concentration profiles, for a flow under air (left) and a turbidity current (right), from Parker (2007).

- a turbidity current flows under ambient water with a density ρ_w , which is *not* negligible;
- a river flows down-slope under the influence of gravity acting on the *water*, the water then drags the sediment with it;
- a turbidity current flows down-slope under the influence of gravity acting on the *sediment*, the sediment then drags the water with it;
- turbidity currents die as concentration will dilute, river flows do not die as $c \rightarrow 0$.

As particles in turbidity currents can settle, turbidity currents constantly have to keep their sediments in suspension in order to survive. Sediments within dilute turbidity currents are kept in suspension by turbulence. By looking at the parameters of the presented principle, the following conclusions can be drawn:

- As flood-discharge, sediment concentration and particle sizes vary during the floods, the driving force behind the turbidity current is unsteady, hence turbidity currents are unsteady flows;
- Temperature gradients cause density differences in both ρ_w as in ρ_t , which influence to the rate of stratification. Although density differences due to temperature are much smaller than those caused by sediment concentrations and are most-likely negligible.

A.1 FORMATION OF A TURBIDITY CURRENT: THE PLUNGE POINT

Plunging is a phenomenon when sediment-laden river flow is heavier than the body of water it flows into. The sediment water immediately sinks, forming a continuous turbidity current. Usually plunging is associated with mud-flows, whereas (most of the) larger sand particles tend to deposit in a delta upstream.

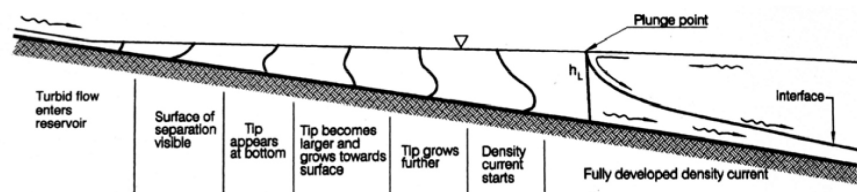
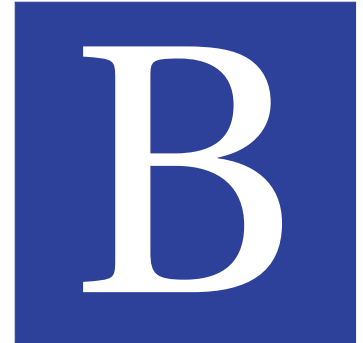


Figure A.3: Transition from non-stratified to stratified flow from Morris and Fan (1998).

The sketched river profile is given in figure A.2. Here the difference between a river flow and a turbidity current is clear: the interface between the river water is sharp with the air above it, while the interface between the ambient water of the reservoir and the turbidity current is more diffuse.

The so-called plunge point (or line) indicates where non-stratified flow plunges beneath the clear ambient water and so produce a stratified flow. The transition from the velocity profile typical for a river to the velocity profile of the turbidity current in the reservoir is demonstrated in figure A.3. The plunging process causes a weak counter-current which moves clear surface water upstream. The plunge point is, because of the counter-current, often clearly visible. It can be by the distinctive coloured sediment-laden water and possibly by the gathering of floating debris, e.g., wood logs and plastics.

The plunge point its location is not fixed. It is determined by the water level, inflowing discharge, suspended sediment concentration and the geometry of the reservoir (Morris & Fan, 1998). For further insight in the plunge point depth and the physical dimensions of the reservoir, reference is made to Akiyama and Stefan (1984).



2DV Sensitivity Analysis Results

The following tests were conducted:

1. Time step Δt ;
2. Horizontal grid size Δx ;
3. Vertical grid:
 - (a) Distribution profile of layers over the vertical;
 - (b) Number of layers,
4. Background turbulent viscosity:
 - (a) Horizontal eddy viscosity;
 - (b) Horizontal eddy diffusivity;
 - (c) Vertical eddy viscosity;
 - (d) Vertical eddy diffusivity;
 - (e) Ozmidov length scale,
5. Hydraulic settings:
 - (a) Roughness of the bed;
 - (b) Initial water level;
 - (c) Inflow discharge;
 - (d) Effect of the σ -correction filter;
 - (e) Hydrostatic versus non-hydrostatic,
6. Sediment parameters:
 - (a) Settling velocity;
 - (b) Hindered settling concentration;
 - (c) Specific density;
 - (d) Dry bed density;
 - (e) Inflow concentration.

In the following tables two different reference models were used to compute the relative differences in velocities, deposit and plunge point location. The two standard settings are given in table B.1, i.e. a high resolution reference (1) and a low resolution reference (2).

Table B.1: Default settings for the two reference models in the 2DV sensitivity analyses.

Roughness C	50	$\text{m}^{1/2} \text{s}^{-1}$
σ correction	Y	
Hydrostatic	Y	
Sediment parameters		
Gelling concentration	117.234	kg m^{-3}
Specific Density	2760	kg m^{-3}
Dry bed density	1656	kg m^{-3}
Settling Velocity	0.0519	mm/s
Shear stress Sedimentation	1000	N m^{-2}
Shear stress Erosion	0.5	N m^{-2}
Turbulence parameters		
Hor. Viscosity	10^{-9}	$\text{m}^2 \text{s}^{-1}$
Hor. Diffusivity	10^{-9}	$\text{m}^2 \text{s}^{-1}$
Ver. Viscosity	10^{-8}	$\text{m}^2 \text{s}^{-1}$
Ver. Diffusivity	10^{-8}	$\text{m}^2 \text{s}^{-1}$
Ozmidov length scale	0	m
Boundary conditions		
Q-river	20	$\text{m}^2 \text{s}^{-1}$
Water level	242.5	m
Inflow SSC	30	kg m^{-3}
Reference 1		
Time step	0.75	s
Grid size	10	m
Ver. layers	100	
Grid profile	equal	
Reference 2		
Time step	7.5	s
Grid size	100	m
Ver. layers	50	
Grid profile	LN-log	

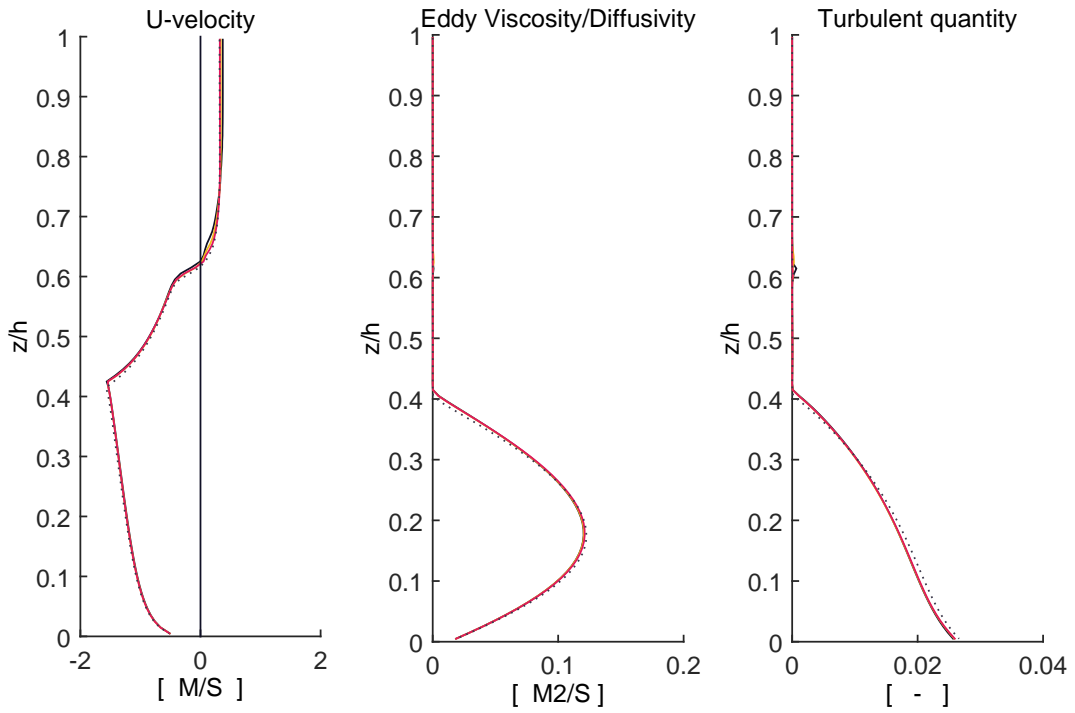
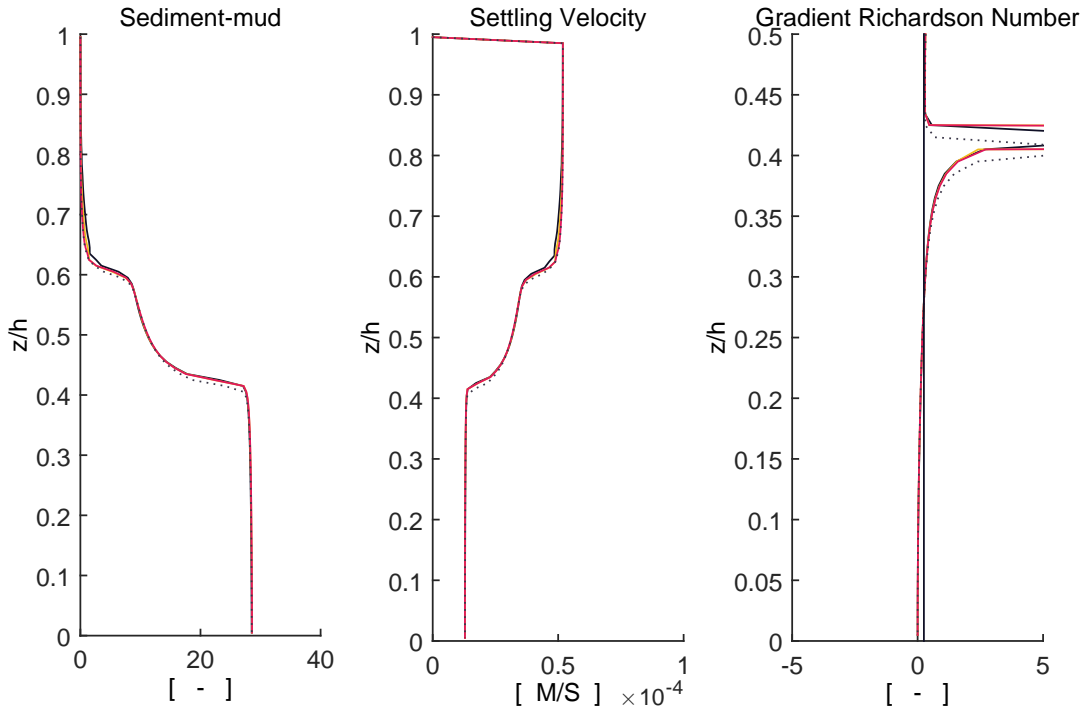
Table B.2: 2DV sensitivity analyses results.

Run	Parameter	Value	Unit	\bar{u} m s^{-1}	\bar{u}_{plunge} m s^{-1}	x_{plunge} m	Deposit 10^3 kg	\bar{u} %	\bar{u}_{plunge} %	x_{plunge} m	Deposit %	Crash	Remarks
1	Time step	6	s										
2	Time step	3	s	1.394	1.129	12 670	51.20	-3.2	-4.4	-80	2.1	N	
3	Time step	1.5	s	1.417	1.157	12 700	50.35	-1.6	-2.0	-50	0.4	N	
4	Time step	12	s									Y	
5	Time step	20	s									Y	
6	Time step	0.75	s	1.423	1.164	12 710	50.25	-1.2	-1.4	-40	0.2	N	
006Z		Reference 1		1.440	1.181	12 750	50.13	0.0	0.0	0	0.0	N	LN-layer
7	σ -correction	N		1.429	1.171	12 720	49.97	-0.8	-0.8	-30	-0.3	N	
8	Hydrostatic	Y					$z\text{-grid}$					N	
9	Hydrostatic	N					$z\text{-grid}$					N	
10	Grid size	20	m	1.423	1.164	12 640	50.12	-1.2	-1.4	-110	0.0	N	
11	Grid size	50	m	1.411	1.150	12 350	50.23	-2.0	-2.6	-400	0.2	N	
12	Grid size	100	m	1.400	1.139	12 100	50.05	-2.8	-3.6	-650	-0.2	N	
13	Grid size	200	m	1.362	1.118	11 600	50.12	-5.4	-5.3	-1150	0.0	N	
14	LN-layer	50		1.429	1.164	12 710	50.46	-0.8	-1.4	-40	0.7	N	
15	LN-layer	25		1.423	1.163	12 420	50.51	-1.2	-1.5	-330	0.7	N	
16	LN-layer	15		1.423	1.153	11 900	50.78	-1.2	-2.4	-850	1.3	N	
17	Sed-layer	100		1.434	1.170	12 710	50.46	-0.4	-0.9	-40	0.7	N	
18	Sed-layer	50		1.429	1.164	12 640	50.45	-0.8	-1.4	-110	0.6	N	
19	Sed-layer	25		1.411	1.146	12 240	51.08	-2.0	-3.0	-510	1.9	N	
20	Sed-layer	15		1.411	1.142	11 720	51.28	-2.0	-3.3	-1030	2.3	N	
25		Settings reference 2		1.400	1.139	12 100	50.41	-2.8	-3.6	-650	0.6	N	$\Delta t = 0.75 \text{ s}$
25	Time step	0.75	s	1.400	1.139	12 100	50.41	0.8	0.5	0	-0.7	N	
28		Reference 2		1.389	1.133	12 100	50.75	0.0	0.0	0	0.0	N	
31	Roughness C	40	$\text{m}^{1/2} \text{ s}^{-1}$	1.311	1.054	11 700	50.76	-5.6	-7.0	-400	0.0	N	
32	Roughness C	60	$\text{m}^{1/2} \text{ s}^{-1}$	1.458	1.196	12 200	50.50	5.0	5.6	100	-0.5	N	
33	Roughness C	70	$\text{m}^{1/2} \text{ s}^{-1}$	1.515	1.248	12 500	50.42	9.1	10.2	400	-0.6	N	
69	Roughness n	0.01	$\text{m}^{1/3} \text{ s}^{-1}$	1.777	1.489	12 600	47.41	27.9	31.4	500	-6.6	N	
70	Roughness n	0.0125	$\text{m}^{1/3} \text{ s}^{-1}$	1.733	1.448	12 600	47.19	24.8	27.8	500	-7.0	N	
71	Roughness n	0.015	$\text{m}^{1/3} \text{ s}^{-1}$	1.683	1.409	12 600	47.36	21.2	24.4	500	-6.7	N	

Run	Parameter	Value	Unit	\bar{u} m s^{-1}	\bar{u}_{plunge} m s^{-1}	x_{plunge} m	Deposit 10^3 kg	\bar{u} %	\bar{u}_{plunge} %	x_{plunge} m	Deposit %	Crash	Remarks
34	BG Hor. Viscosity	10^{-8}	$\text{m}^2 \text{ s}^{-1}$	1.389	1.133	12 100	50.74	0.0	0.0	0	0.0	N	
35	BG Hor. Viscosity	10^{-7}	$\text{m}^2 \text{ s}^{-1}$	1.389	1.133	12 100	50.74	0.0	0.0	0	0.0	N	
35.2	BG Hor. Viscosity	10^{-1}	$\text{m}^2 \text{ s}^{-1}$	1.389	1.133	12 100	50.75	0.0	0.0	0	0.0	N	
35.3	BG Hor. Viscosity	2	$\text{m}^2 \text{ s}^{-1}$	1.394	1.139	12 100	50.45	0.4	0.5	0	-0.6	N	
36	BG Hor. Diffusivity	10^{-8}	$\text{m}^2 \text{ s}^{-1}$	1.389	1.133	12 100	50.74	0.0	0.0	0	0.0	N	
37	BG Hor. Diffusivity	10^{-7}	$\text{m}^2 \text{ s}^{-1}$	1.389	1.133	12 100	50.74	0.0	0.0	0	0.0	N	
37.2	BG Hor. Diffusivity	1	$\text{m}^2 \text{ s}^{-1}$	1.389	1.133	12 100	50.74	0.0	0.0	0	0.0	N	
37.3	BG Hor. Diffusivity	10^1	$\text{m}^2 \text{ s}^{-1}$	1.373	1.108	12 100	51.53	-1.2	-2.2	0	1.5	N	
38	BG Ver. Viscosity	10^{-9}	$\text{m}^2 \text{ s}^{-1}$	1.389	1.133	12 100	50.75	0.0	0.0	0	0.0	N	
39	BG Ver. Viscosity	10^{-7}	$\text{m}^2 \text{ s}^{-1}$	1.389	1.133	12 100	50.75	0.0	0.0	0	0.0	N	
39.2	BG Ver. Viscosity	10^{-6}	$\text{m}^2 \text{ s}^{-1}$	1.389	1.133	12 100	50.75	0.0	0.0	0	0.0	N	
39.3	BG Ver. Viscosity	10^{-5}	$\text{m}^2 \text{ s}^{-1}$	1.389	1.133	12 100	50.75	0.0	0.0	0	0.0	N	
39.4	BG Ver. Viscosity	10^{-4}	$\text{m}^2 \text{ s}^{-1}$	1.389	1.133	12 100	50.74	0.0	0.0	0	0.0	N	
39.5	BG Ver. Viscosity	10^{-3}	$\text{m}^2 \text{ s}^{-1}$	1.383	1.124	12 000	50.96	-0.4	-0.8	-100	0.4	N	
39.6	BG Ver. Viscosity	10^{-2}	$\text{m}^2 \text{ s}^{-1}$	1.277	1.010	10 300	51.00	-8.1	-10.9	-1800	0.5	N	
40	BG Ver. Diffusivity	10^{-9}	$\text{m}^2 \text{ s}^{-1}$	1.389	1.133	12 100	50.75	0.0	0.0	0	0.0	N	
41	BG Ver. Diffusivity	10^{-7}	$\text{m}^2 \text{ s}^{-1}$	1.389	1.133	12 100	50.75	0.0	0.0	0	0.0	N	
41.2	BG Ver. Diffusivity	10^{-6}	$\text{m}^2 \text{ s}^{-1}$	1.389	1.133	12 100	50.75	0.0	0.0	0	0.0	N	
41.3	BG Ver. Diffusivity	10^{-5}	$\text{m}^2 \text{ s}^{-1}$	1.389	1.133	12 100	50.75	0.0	0.0	0	0.0	N	
41.4	BG Ver. Diffusivity	10^{-4}	$\text{m}^2 \text{ s}^{-1}$	1.389	1.133	12 100	50.75	0.0	0.0	0	0.0	N	
41.5	BG Ver. Diffusivity	10^{-3}	$\text{m}^2 \text{ s}^{-1}$	1.389	1.133	12 100	50.75	0.0	0.0	0	0.0	N	
41.6	BG Ver. Diffusivity	10^{-2}	$\text{m}^2 \text{ s}^{-1}$	1.389	1.133	12 100	50.75	0.0	0.0	0	0.0	N	
39+41	BG Ver. Visc. = Diff.	10^{-4}	$\text{m}^2 \text{ s}^{-1}$	1.389	1.133	12 100	50.74	0.0	0.0	0	0.0	N	
42	Ozmidov length scale	10^{-1}	m	1.389	1.133	12 100	50.81	0.0	0.0	0	0.1	N	
43	Ozmidov length scale	0.5	m	1.367	1.102	11 500	52.26	-1.6	-2.7	-600	3.0	N	
44	Ozmidov length scale	1	m	1.321	1.042	11 000	54.66	-4.9	-8.0	-1100	7.7	N	
44.4	Ozmidov length scale	10^1	m	1.074	0.754	7800	66.99	-22.7	-33.5	-4300	32.0	N	
44.5	Ozmidov length scale	5	m	0.949	0.606	400	76.01	-31.7	-46.5	-11 700	49.8	N	

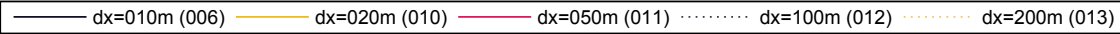
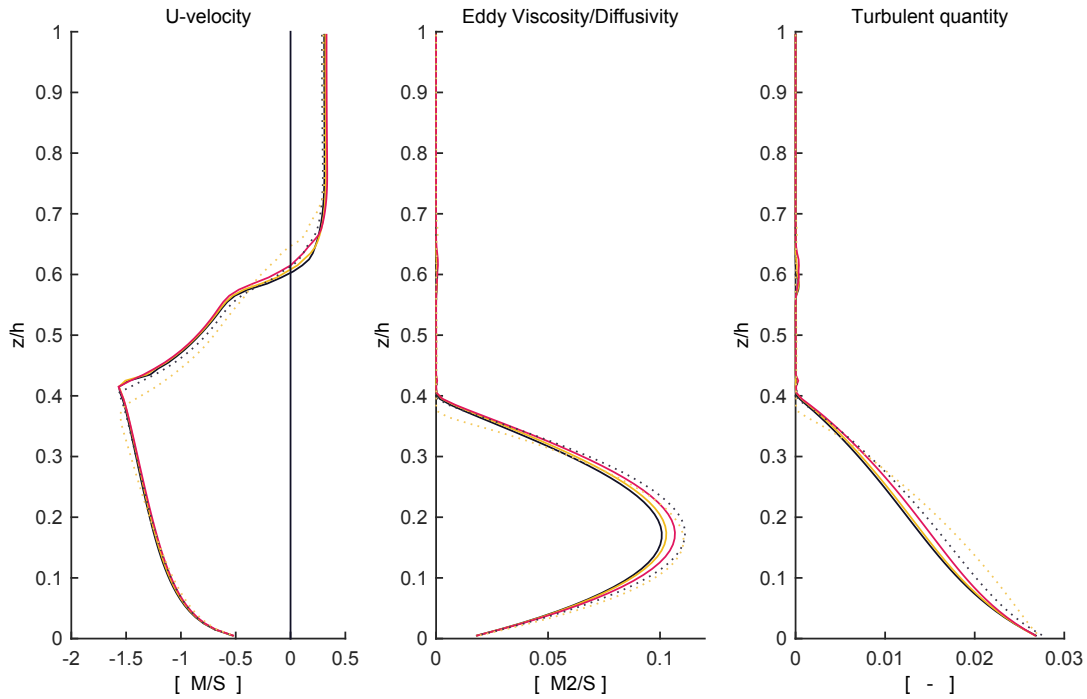
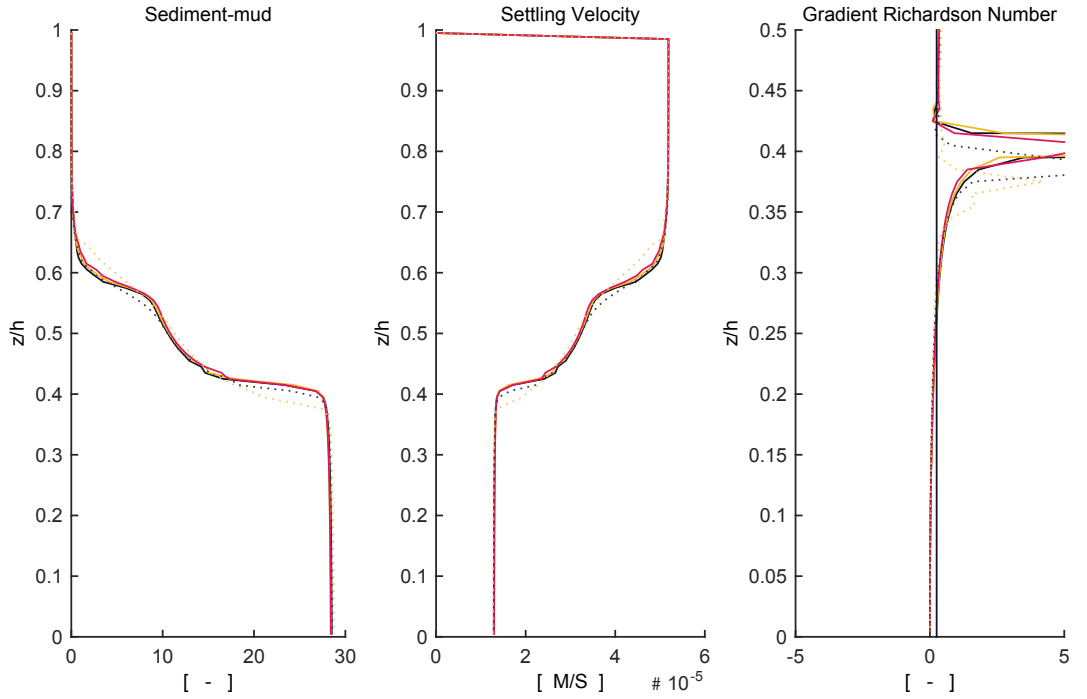
Run	Parameter	Value	Unit	\bar{u} m s ⁻¹	\bar{u}_{plunge} m s ⁻¹	x_{plunge} m	Deposit 10 ³ kg	\bar{u} %	\bar{u}_{plunge} %	x_{plunge} m	Deposit %	Crash	Remarks
45	Settling velocity	0.2595	mm s ⁻¹	1.383	1.127	12 100	256.26	-0.4	-0.5	0	405.0	N	
46	Settling velocity	0.1038	mm s ⁻¹	1.389	1.133	12 100	101.59	0.0	0.0	0	100.2	N	
47	Settling velocity	0.02595	mm s ⁻¹	1.389	1.133	12 100	25.36	0.0	0.0	0	-50.0	N	
48	Settling velocity	0.01038	mm s ⁻¹	1.389	1.133	12 100	10.14	0.0	0.0	0	-80.0	N	
49	Gelling concentration	140.6808	kg m ⁻³	1.389	1.133	12 100	66.22	0.0	0.0	0	30.5	N	
50	Gelling concentration	128.9574	kg m ⁻³	1.389	1.133	12 100	58.78	0.0	0.0	0	15.8	N	
51	Gelling concentration	105.5106	kg m ⁻³	1.389	1.133	12 100	42.16	0.0	0.0	0	-16.9	N	
52	Gelling concentration	93.7872	kg m ⁻³	1.389	1.133	12 100	33.11	0.0	0.0	0	-34.8	N	
53	Specific density	2898	kg m ⁻³	1.406	1.149	12 200	50.02	1.2	1.4	100	-1.4	N	
54	Specific density	2829	kg m ⁻³	1.400	1.142	12 200	50.26	0.8	0.8	100	-1.0	N	
55	Specific density	2691	kg m ⁻³	1.389	1.133	12 100	50.78	0.0	0.0	0	0.1	N	
56	Specific density	2622	kg m ⁻³	1.389	1.133	12 100	50.69	0.0	0.0	0	-0.1	N	
57	Dry bed density	1987.2	kg m ⁻³	1.389	1.133	12 100	52.51	0.0	0.0	0	3.5	N	
58	Dry bed density	1821.6	kg m ⁻³	1.389	1.133	12 100	51.69	0.0	0.0	0	1.9	N	
59	Dry bed density	1490.4	kg m ⁻³	1.389	1.133	12 100	49.67	0.0	0.0	0	-2.1	N	
60	Dry bed density	1324.8	kg m ⁻³	1.389	1.133	12 100	48.42	0.0	0.0	0	-4.6	N	
61	Discharge	20.5	m ² s ⁻¹	1.406	1.143	12 000	50.00	1.2	0.9	-100	-1.5	N	
62	Discharge	21	m ² s ⁻¹	1.429	1.157	11 800	48.94	2.9	2.1	-300	-3.5	N	
63	Discharge	19.5	m ² s ⁻¹	1.373	1.123	12 200	51.48	-1.2	-0.9	100	1.4	N	
64	Discharge	19	m ² s ⁻¹	1.351	1.105	12 200	52.52	-2.7	-2.5	100	3.5	N	
65	Inflow SSC	28	kg m ⁻³	1.367	1.108	11 900	53.74	-1.6	-2.2	-200	5.9	N	
66	Inflow SSC	29	kg m ⁻³	1.378	1.117	12 000	52.27	-0.8	-1.4	-100	3.0	N	
67	Inflow SSC	31	kg m ⁻³	1.400	1.142	12 200	49.16	0.8	0.8	100	-3.1	N	
68	Inflow SSC	30	kg m ⁻³	1.411	1.155	12 200	47.56	1.6	1.9	100	-6.3	N	
68.1	Inflow SSC	320	kg m ⁻³	2.349	2.159	13 600	0.30	69.1	90.6	1500	-99.4	N	
68.2	Inflow SSC	5	kg m ⁻³	0.964	0.672	8100	43.08	-30.6	-40.7	-4000	-15.1	N	
68.3	Inflow SSC	10	kg m ⁻³	1.104	0.815	9100	59.27	-20.5	-28.1	-3000	16.8	N	
WL01	Water Level	242.5	m	0.597	0.818	13 300	88.30					N	SSC: Soulik
WL02	Water Level	245.0	m	0.581	0.833	13 500	93.48	-2.7	1.8	200	5.9	N	SSC: Soulik
WL03	Water Level	240.0	m	0.612	0.830	12 700	84.54	2.5	1.5	-600	-4.3	N	SSC: Soulik
WL04	Water Level	245 to 237.5	m	0.609	0.875	12 600	81.25	2.0	7.0	-700	-8.0	N	SSC: Soulik, water level drop

TIME STEP ANALYSIS at x=7905m

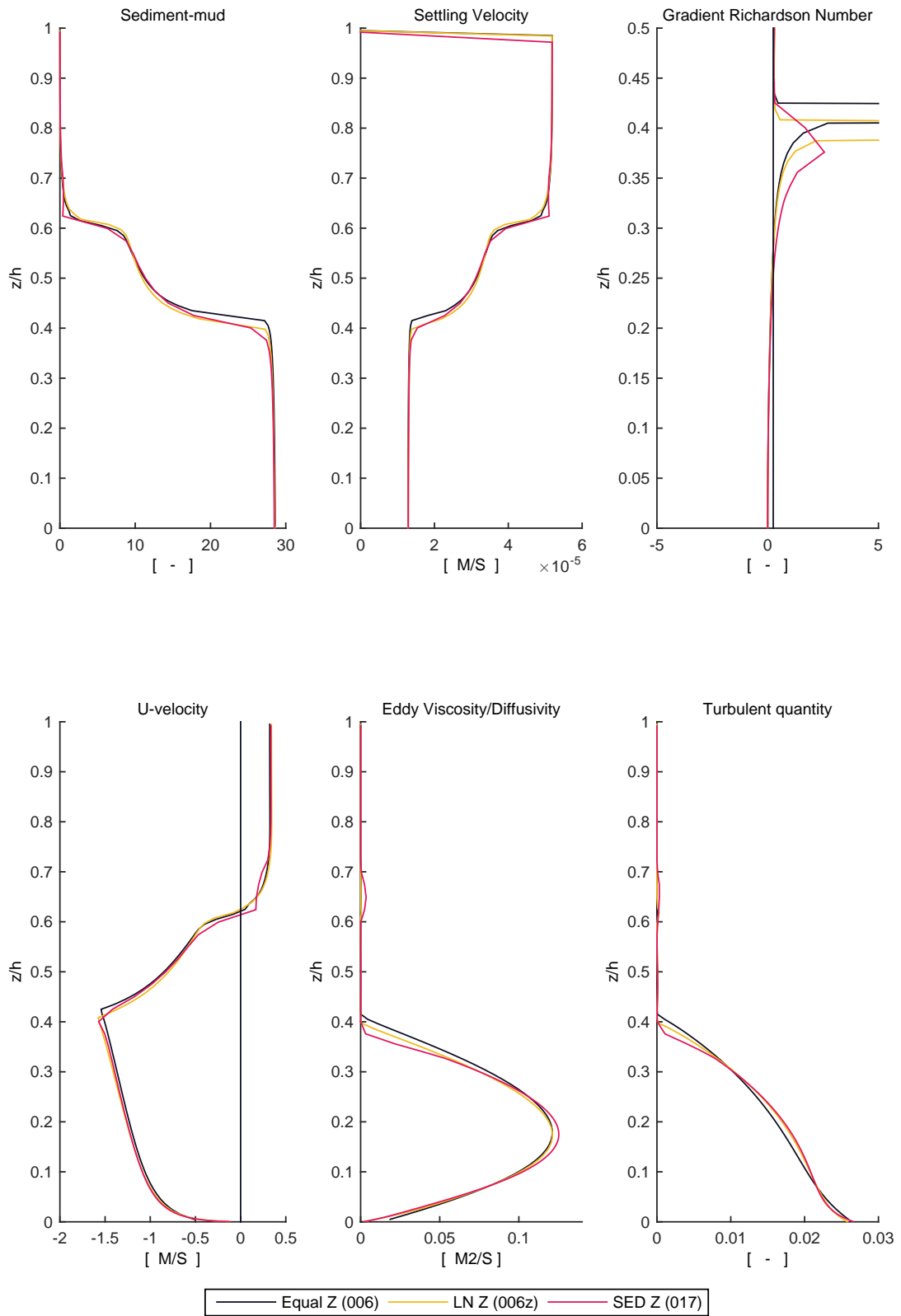


— dt=0.0500 SIGCOR (002) — dt=0.0250 SIGCOR (003) — dt=0.0125 SIGCOR (006) dt=0.0125 (007)

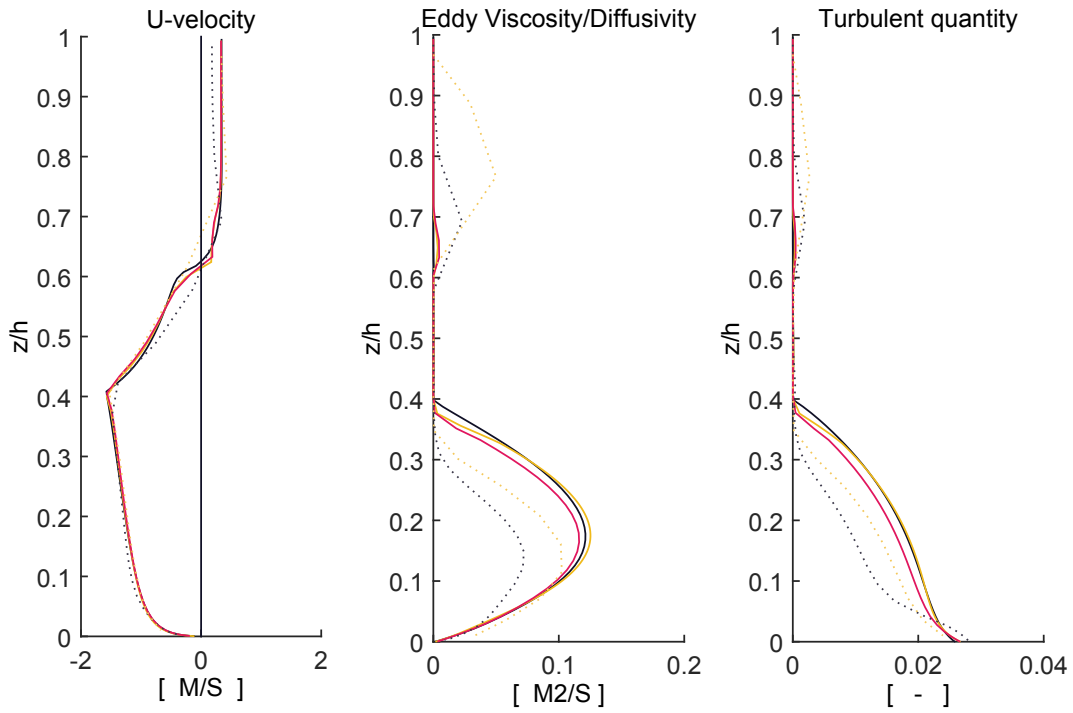
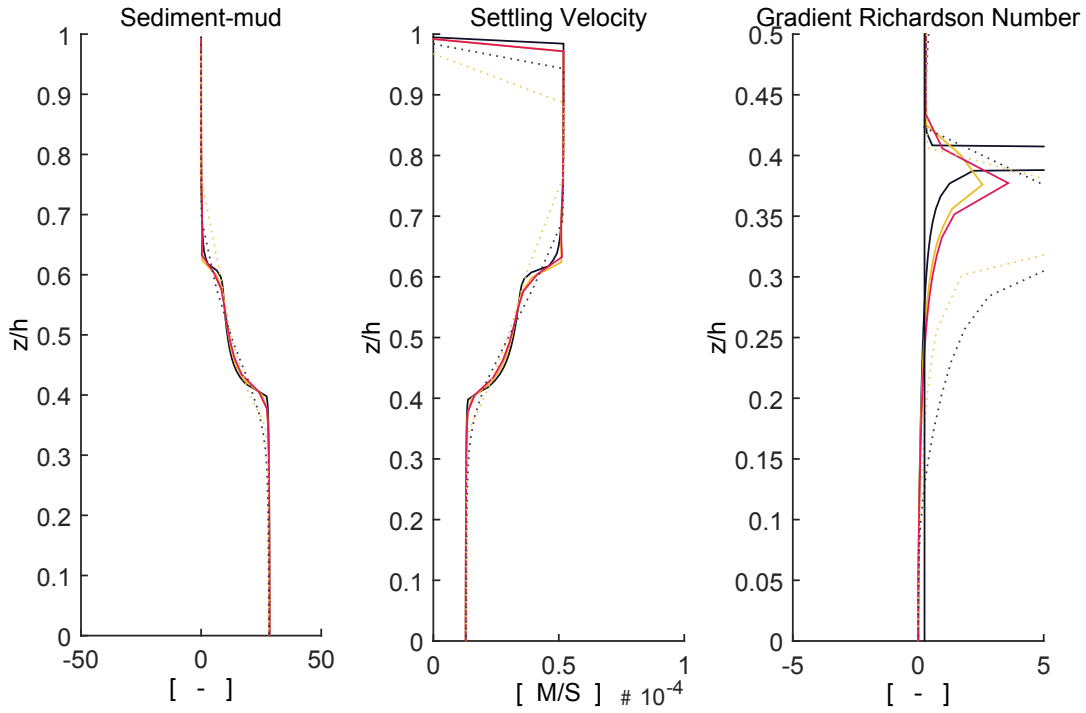
GRID RESOLUTION ANALYSIS at x=7800m



VERTICAL GRID PROFILE ANALYSIS A at x=7905m

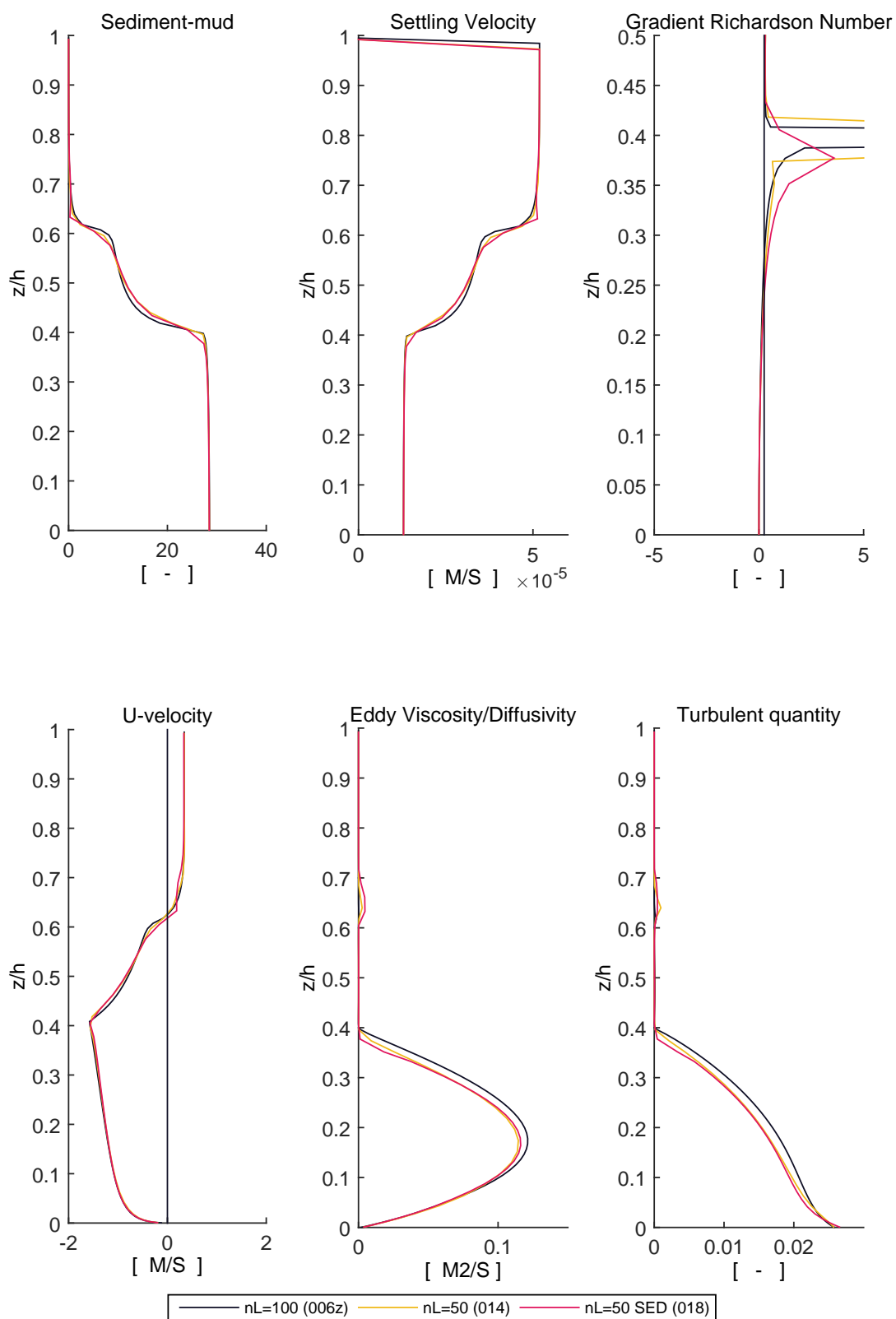


SEDIMENT VERTICAL GRID RESOLUTION ANALYSIS at x=7905m

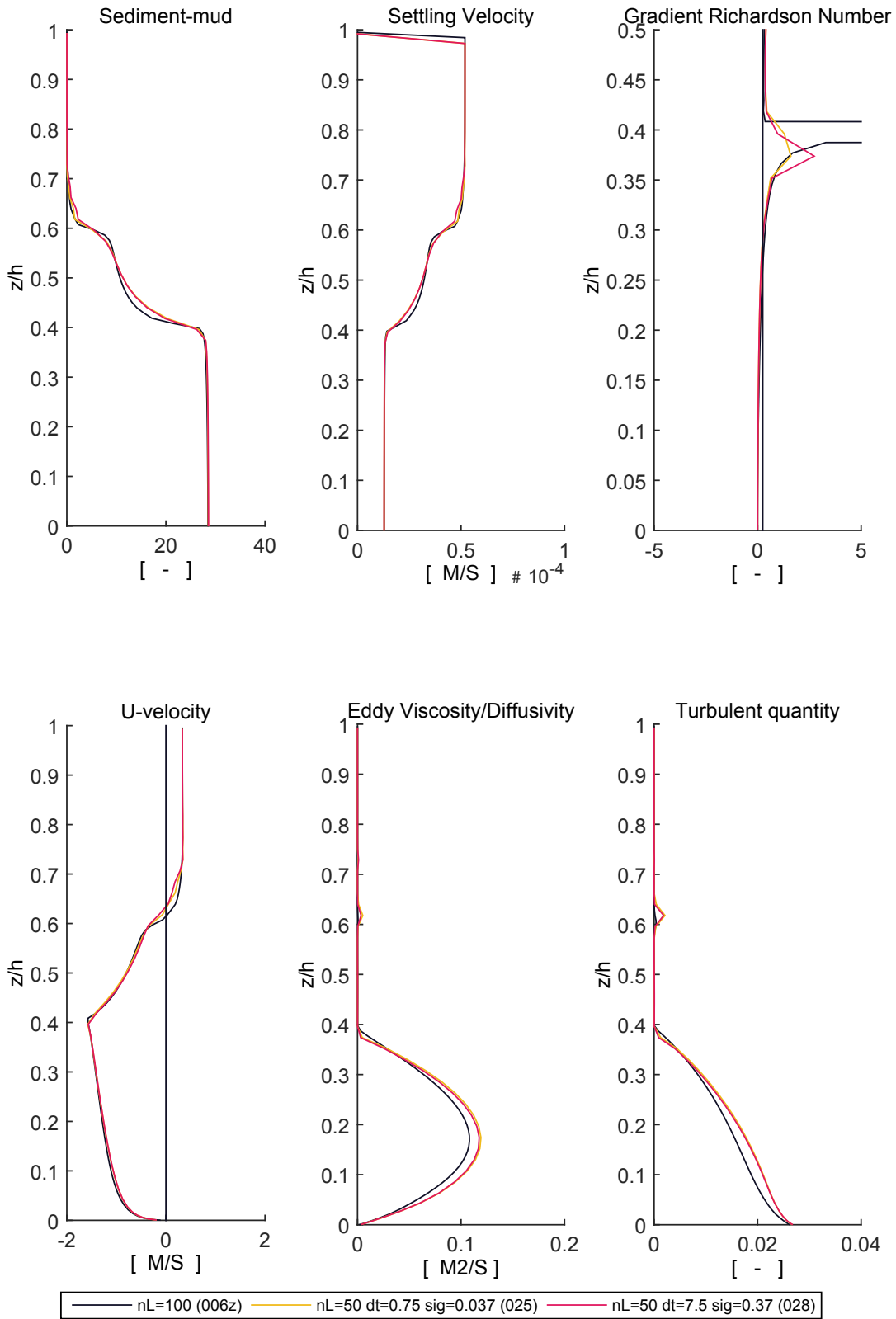


— nL=100 (006z) — nL=100 SED (017) — nL=50 SED (018) nL=25 SED (019) nL=15 SED (020)

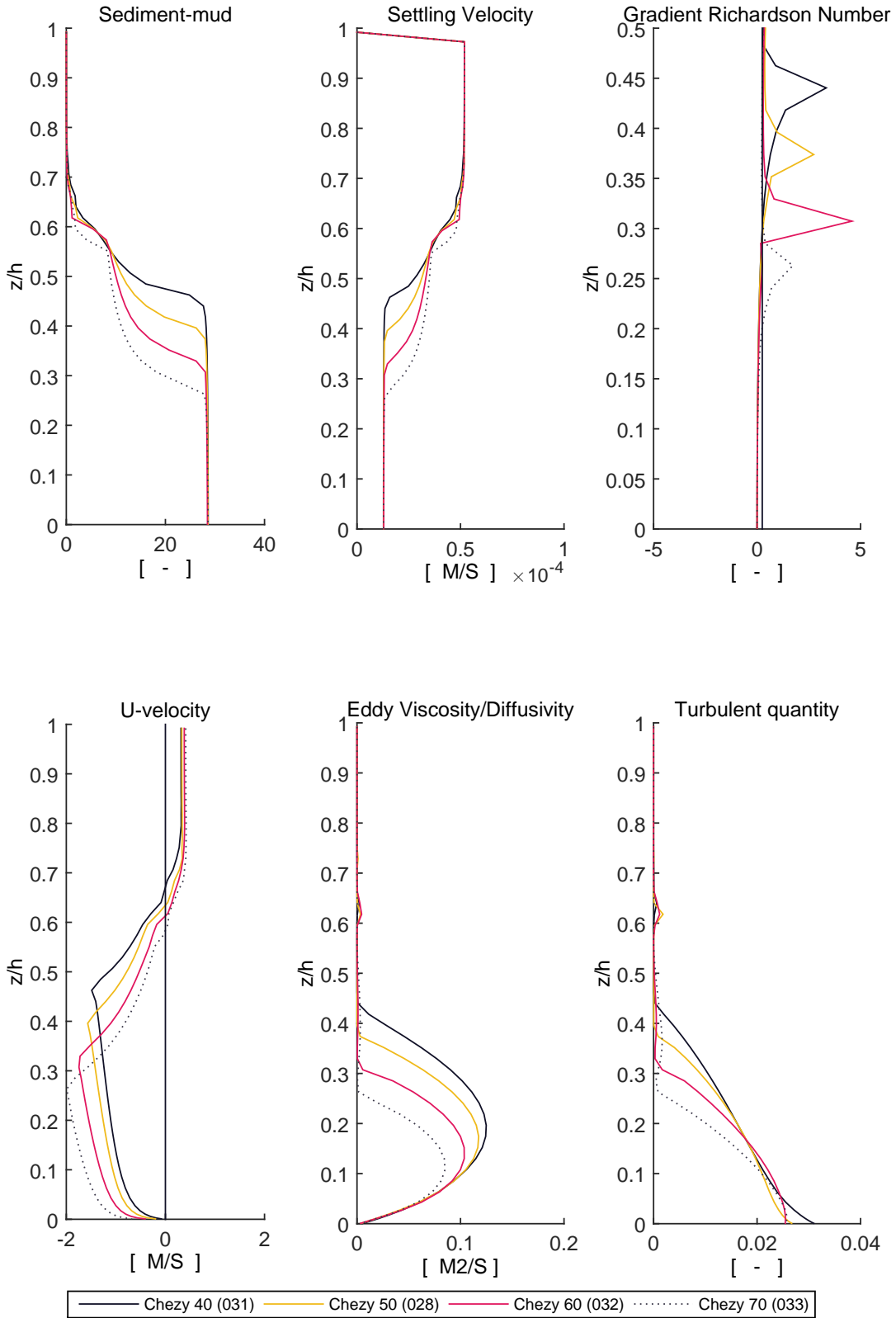
VERTICAL GRID PROFILE ANALYSIS B at x=7905m



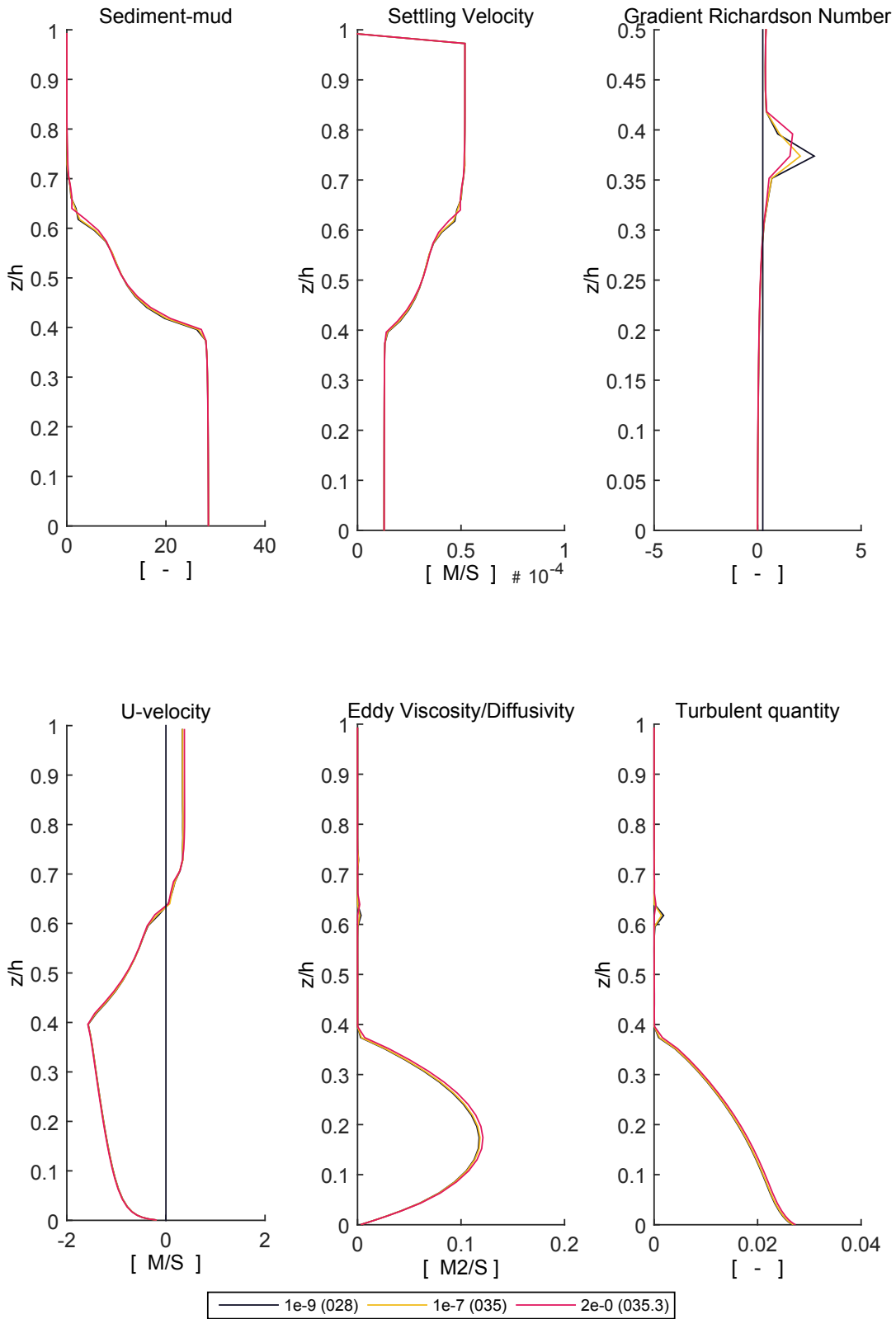
COURANT NUMBER SCALING at x=7850m



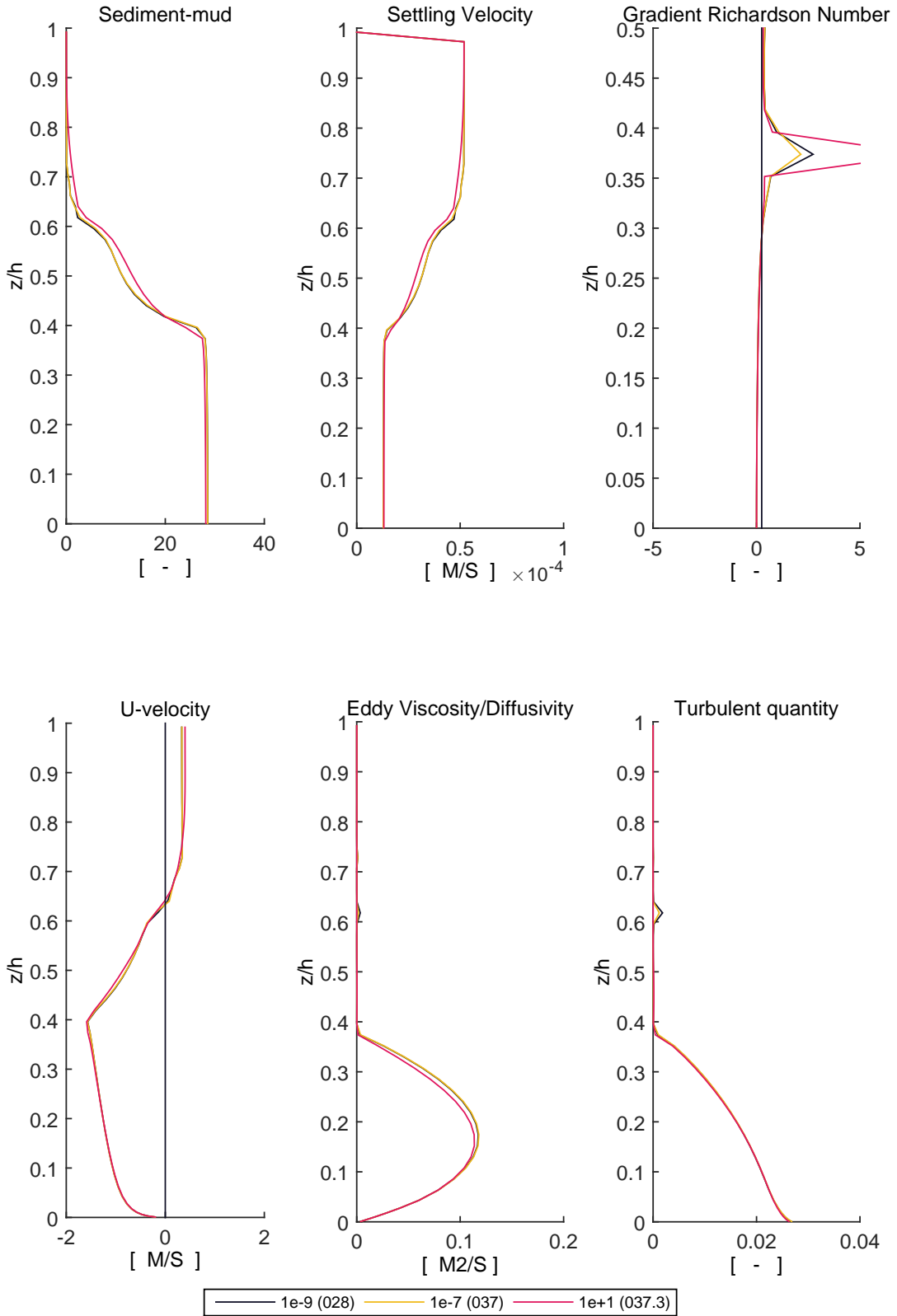
CHEZY COEFFICIENT ANALYSIS at x=7850m



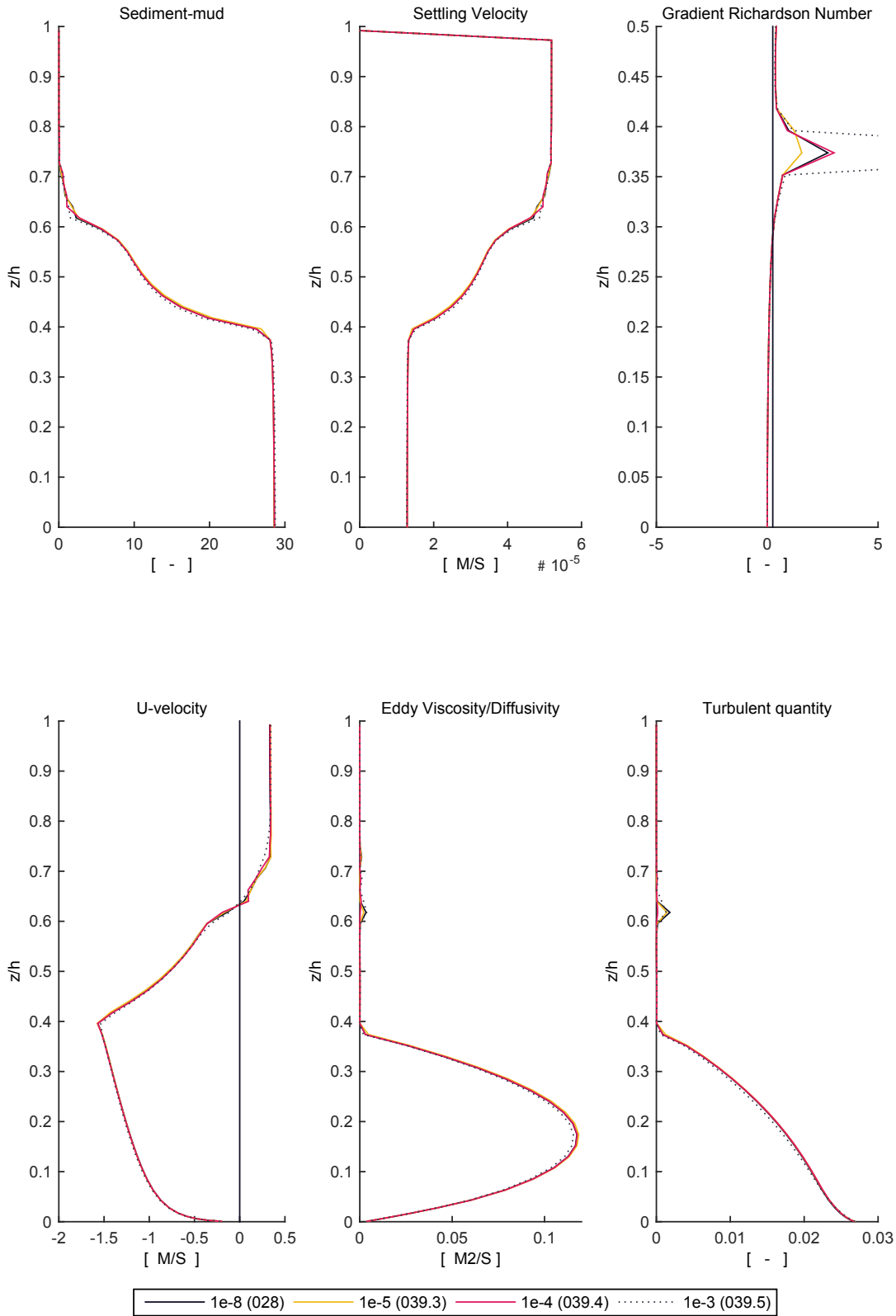
HORIZONTAL EDDY VISCOSITY ANALYSIS at x=7850m



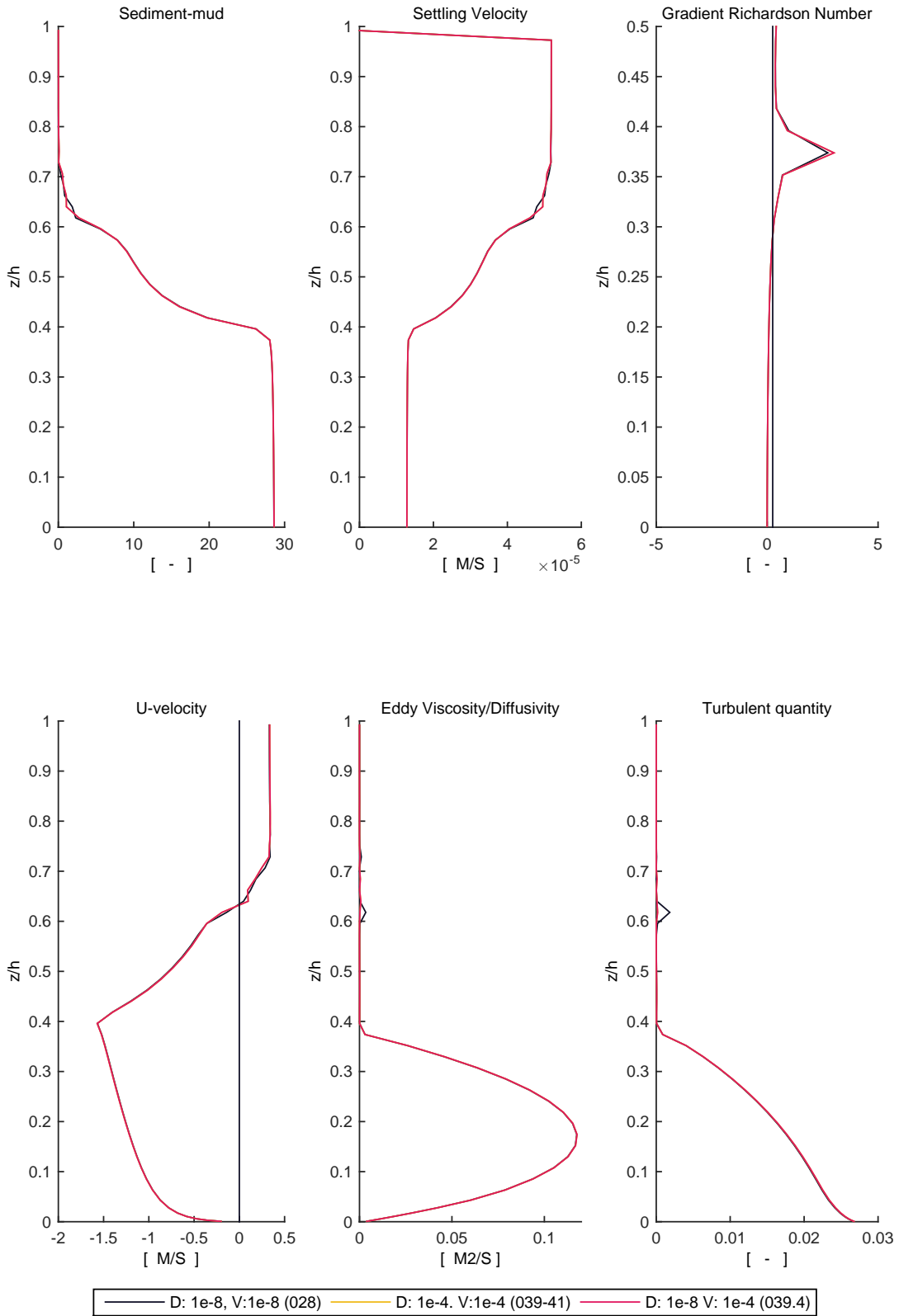
HORIZONTAL EDDY DIFFUSIVITY ANALYSIS at x=7850m



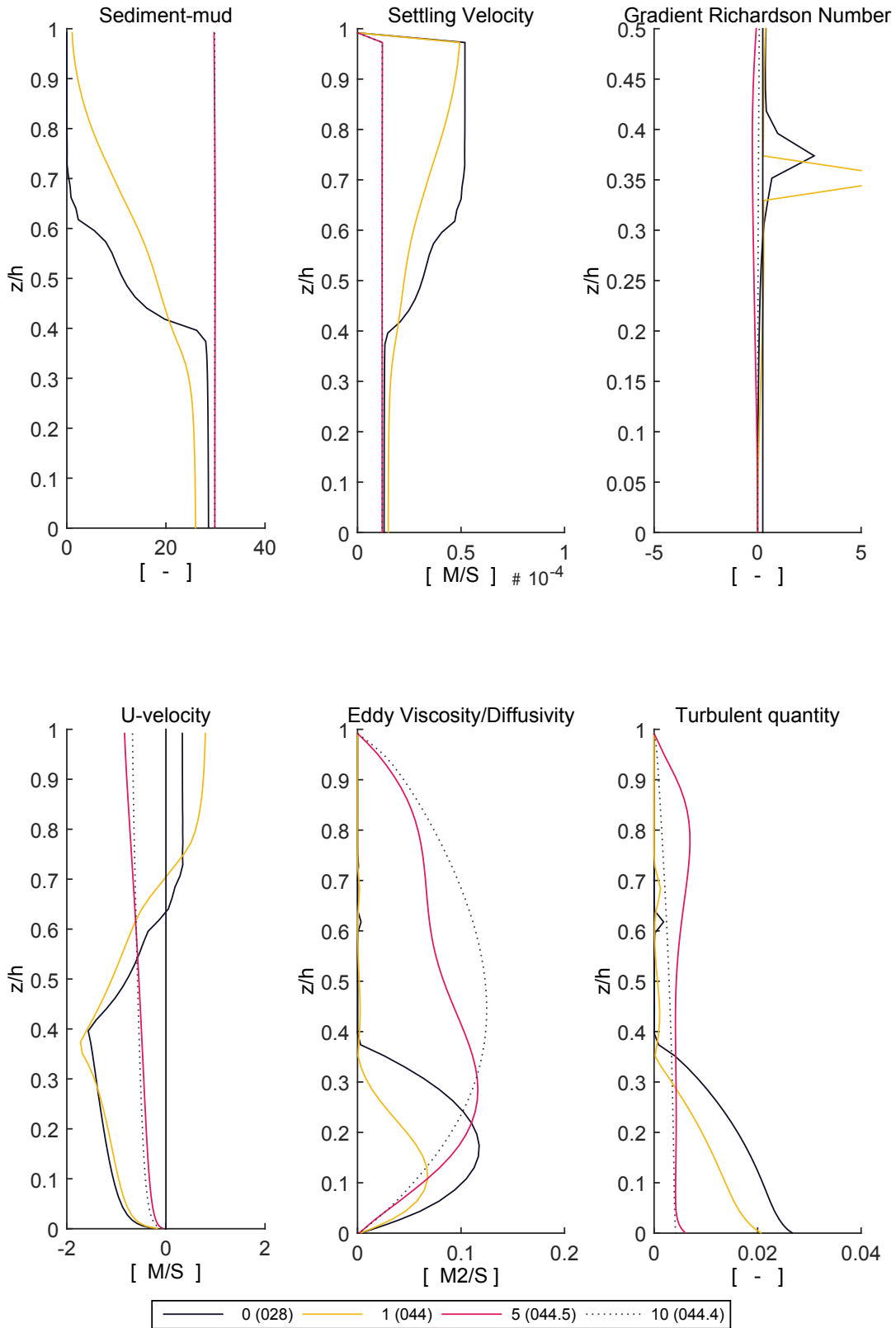
VERTICAL EDDY VISCOSITY ANALYSIS at x=7850m

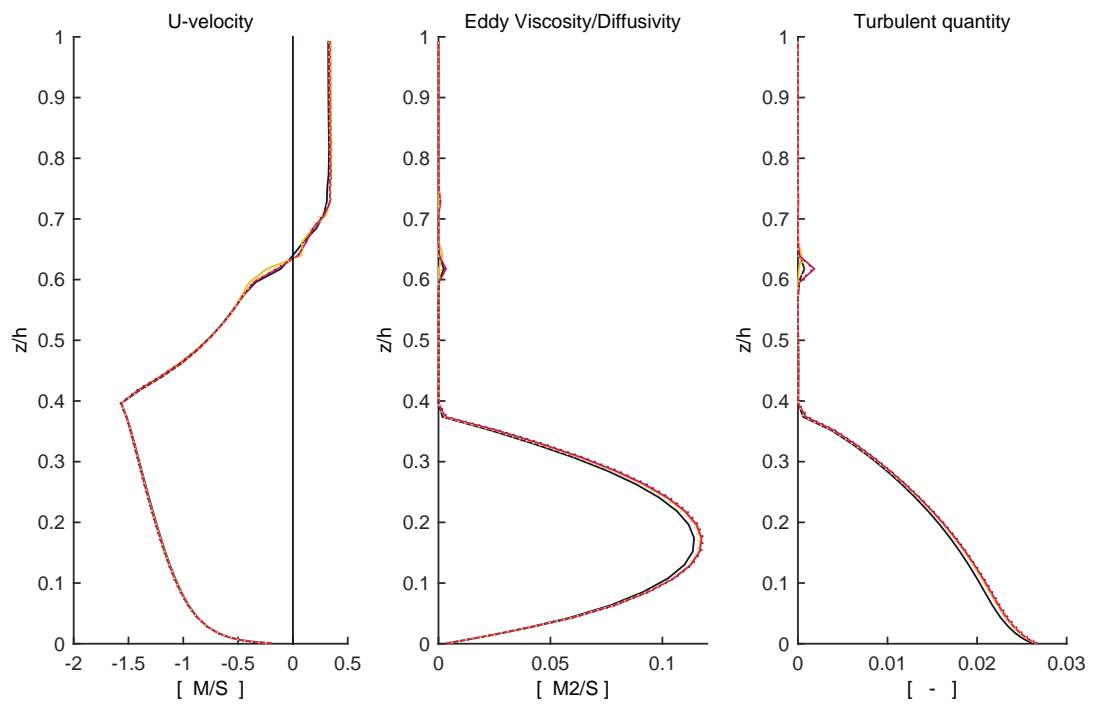
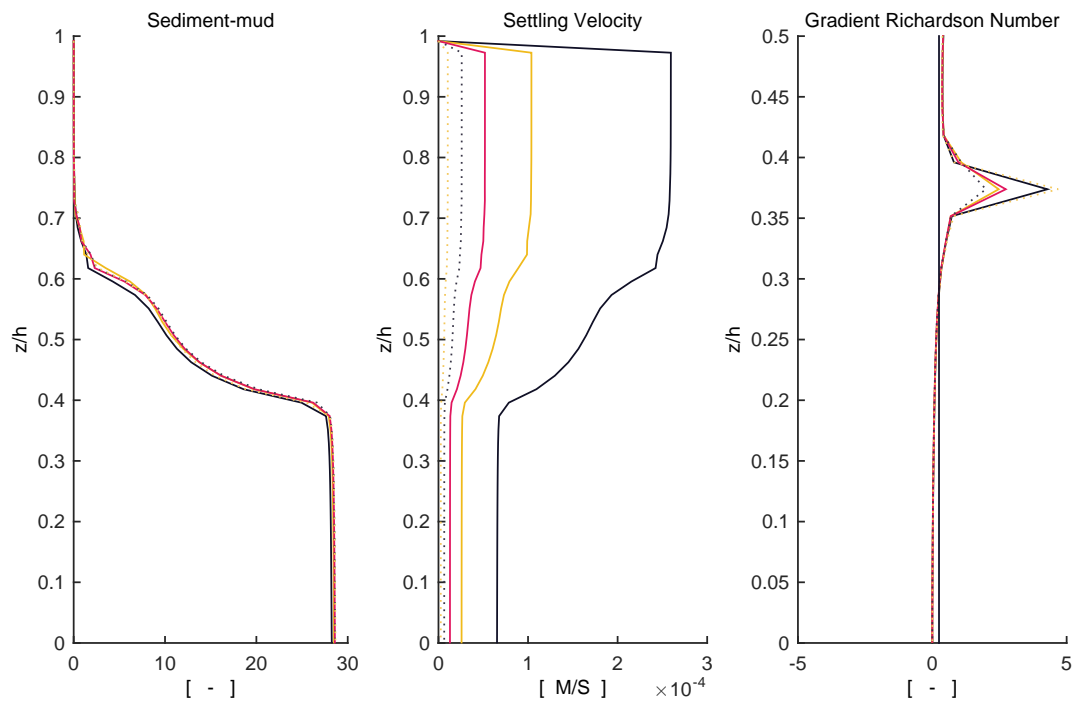


VERTICAL EDDY VISCOSITY & DIFFUSIVITY ANALYSIS at x=7850m



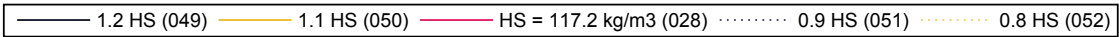
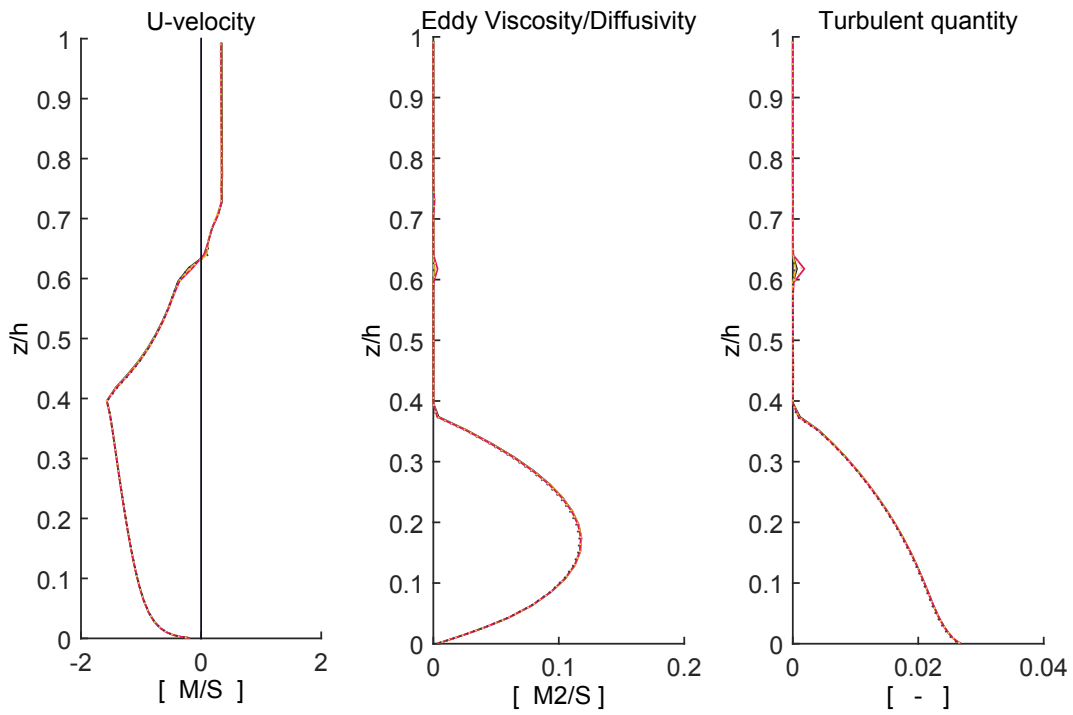
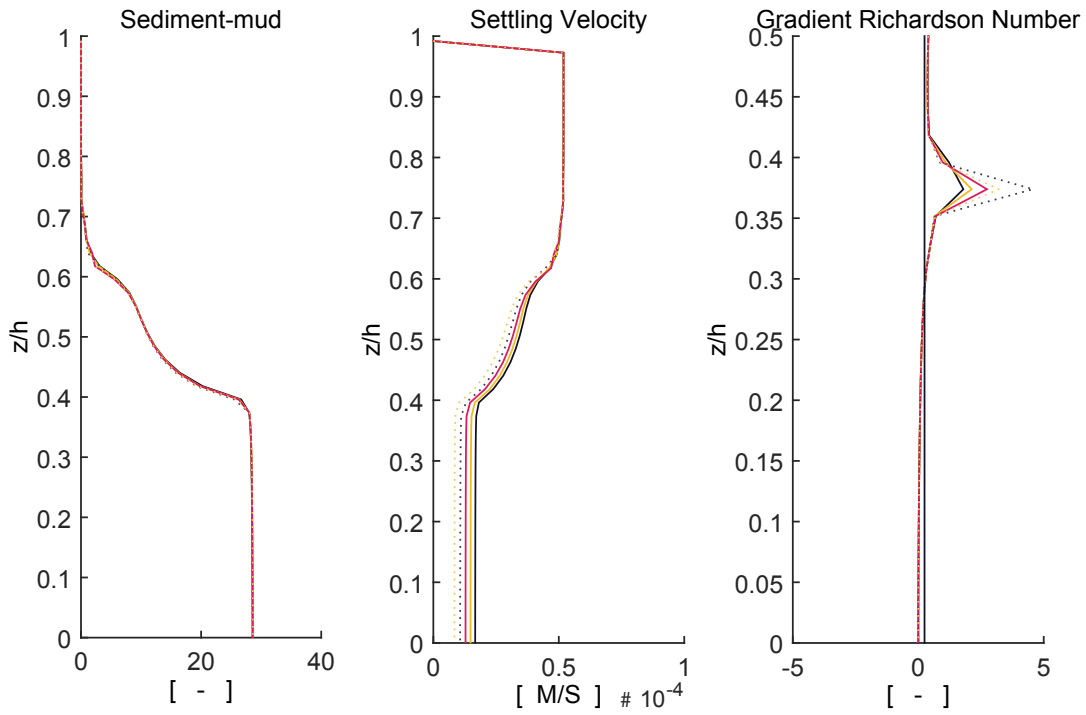
OZMIDOV LENGTH SCALE ANALYSIS at x=7850m



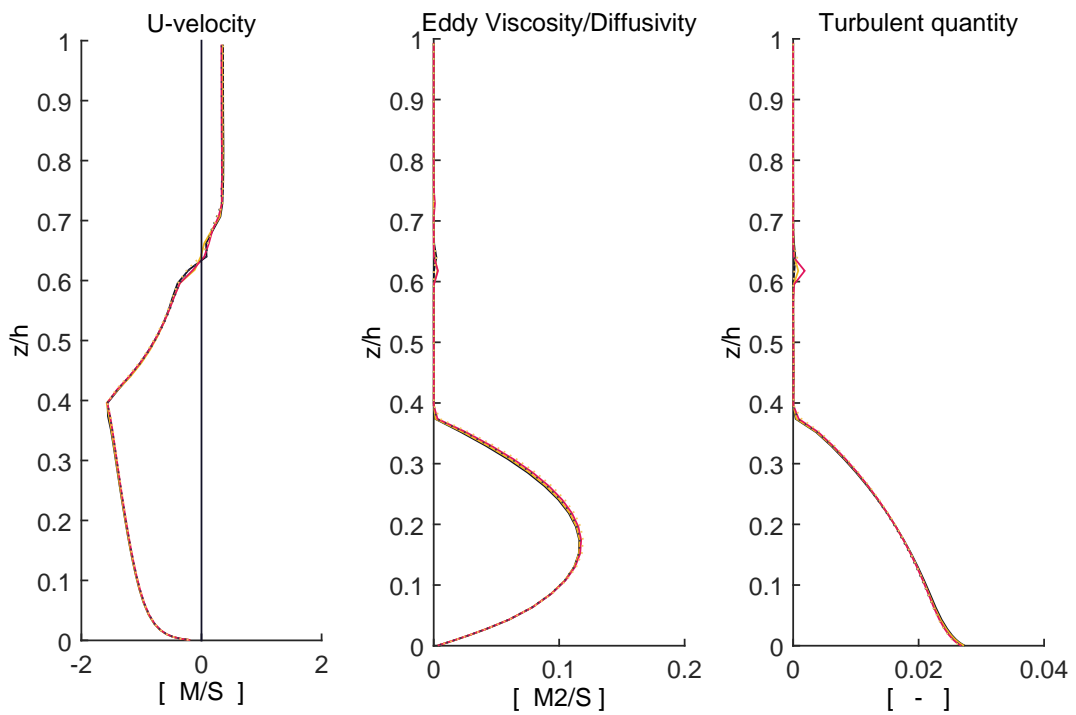
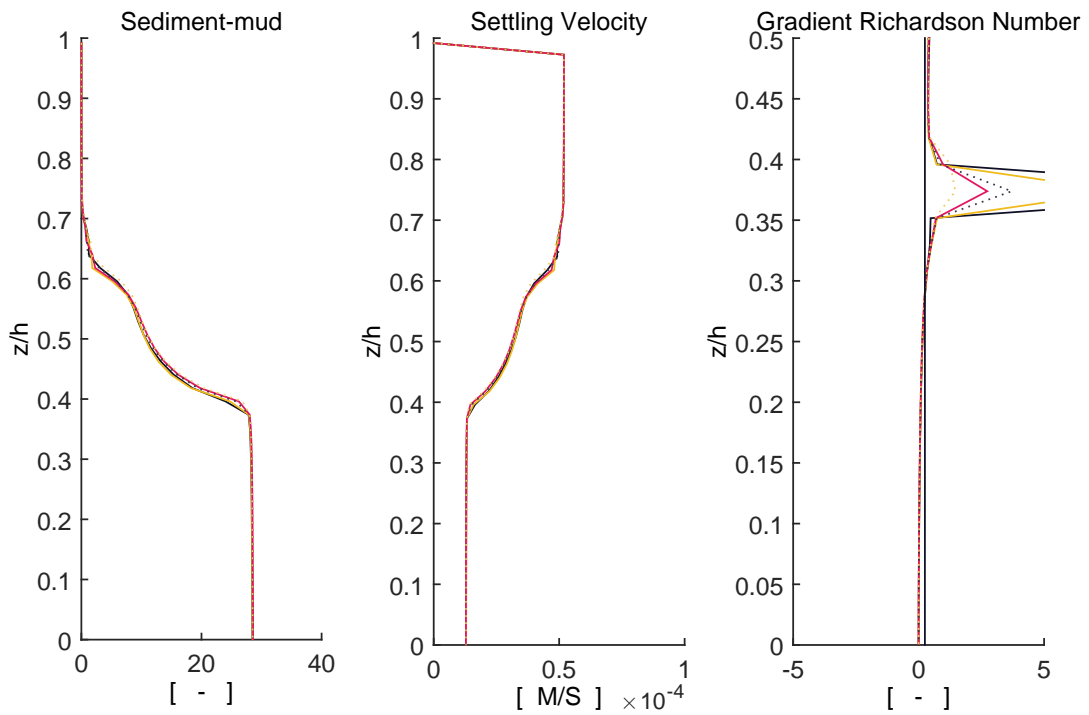
SETTLING VELOCITY ANALYSIS at $x=7850\text{m}$ 

— 5 W_{s0} (045) — 2 W_{s0} (046) — $W_{s0} = 0.052 \text{ mm/s}$ (028) ····· 1/2 W_{s0} (047) ····· 1/5 W_{s0} (048)

HINDERED SETTLING ANALYSIS at x=7850m

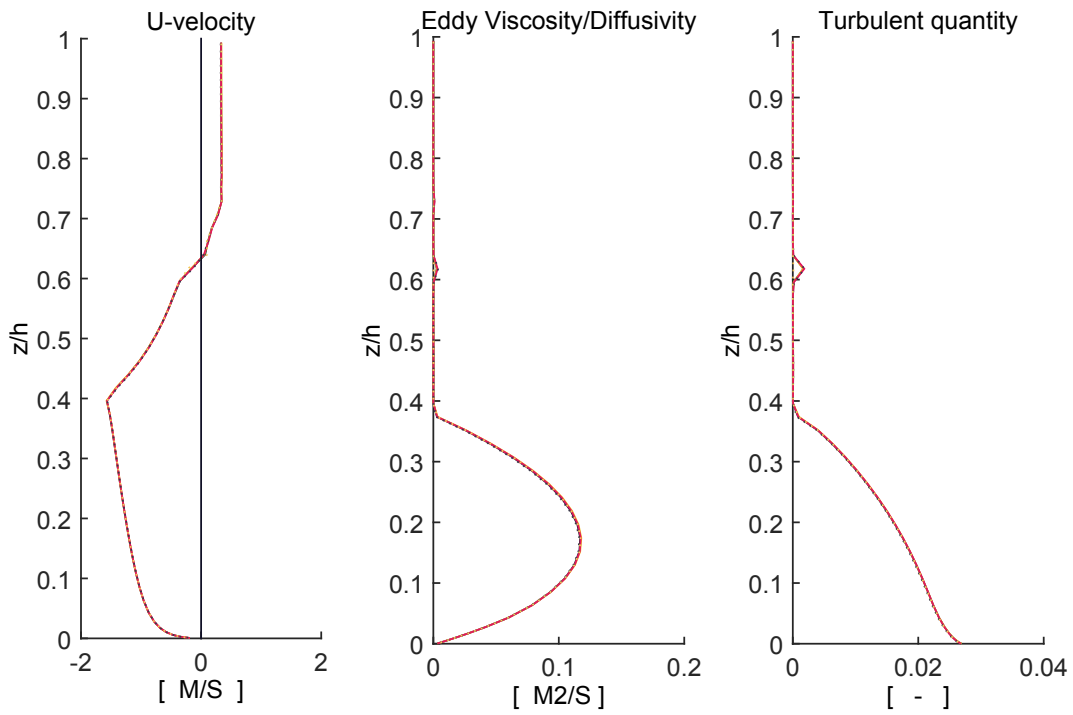
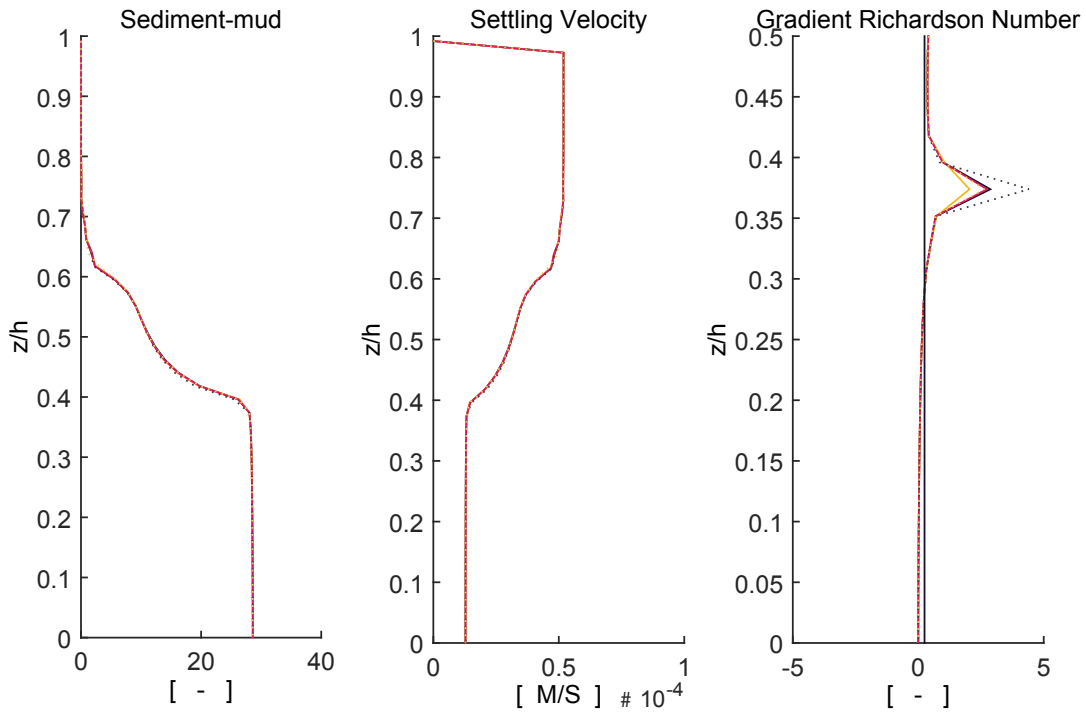


SPECIFIC SEDIMENT DENSITY ANALYSIS at x=7850m



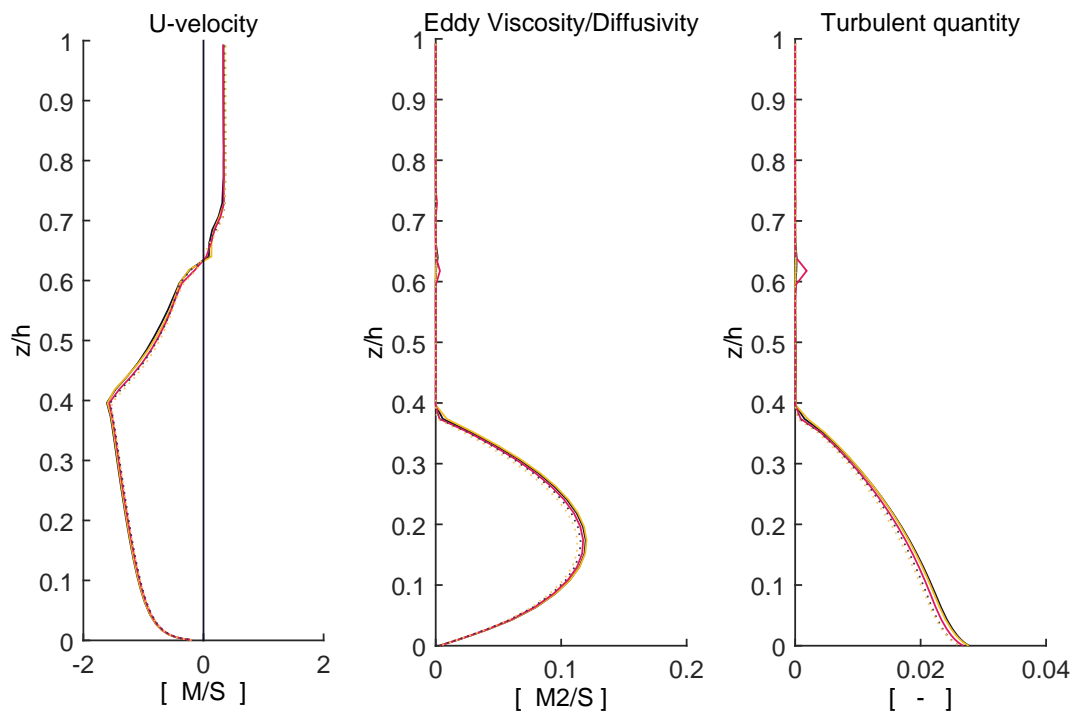
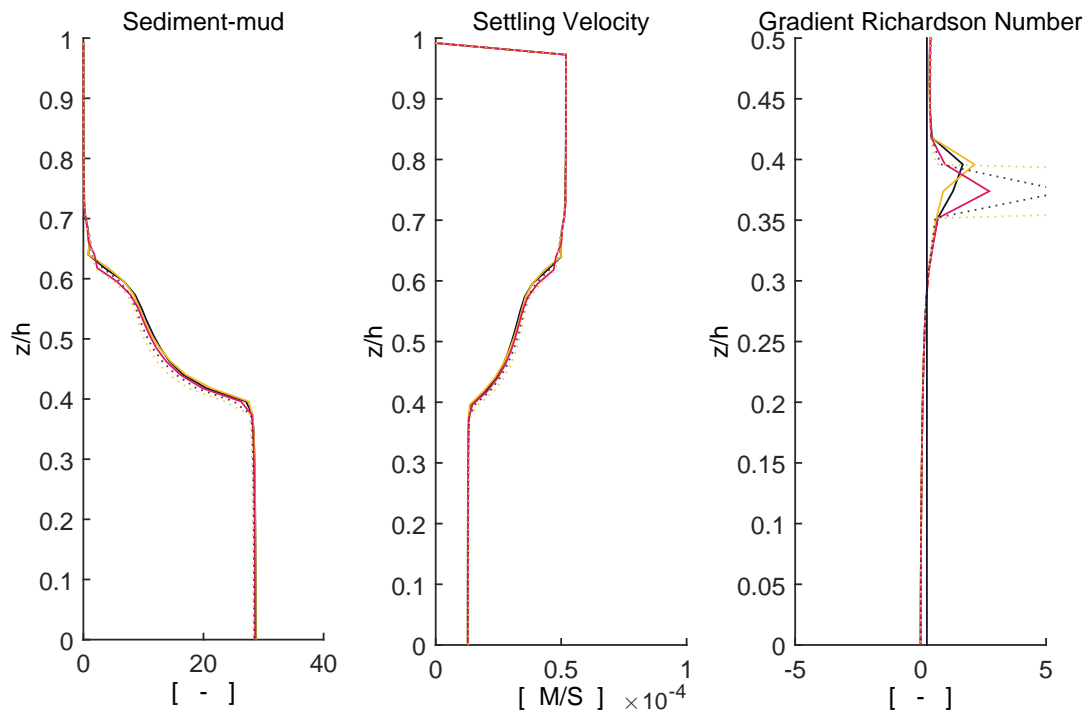
— 1.050 rho (053) — 1.025 rho (054) — rho = 2760 kg/m³ (028) 0.975 rho (055) 0.950 rho (056)

DRY BED DENSITY ANALYSIS at x=7850m



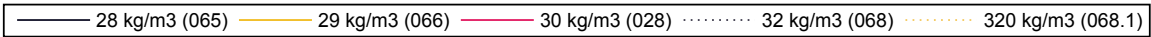
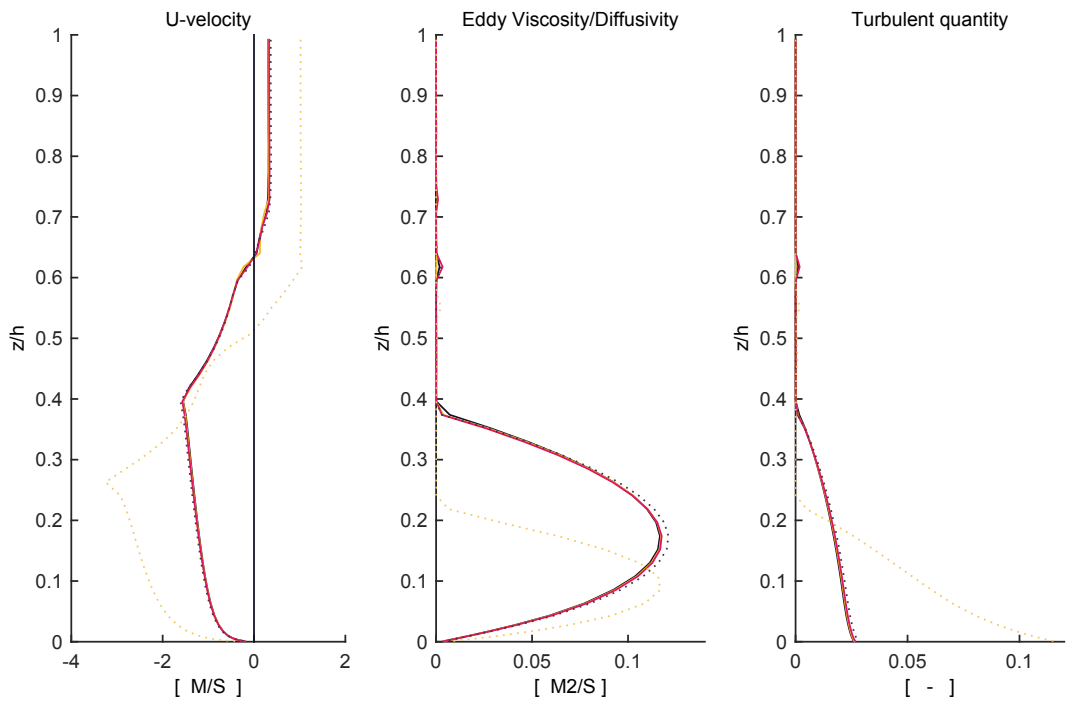
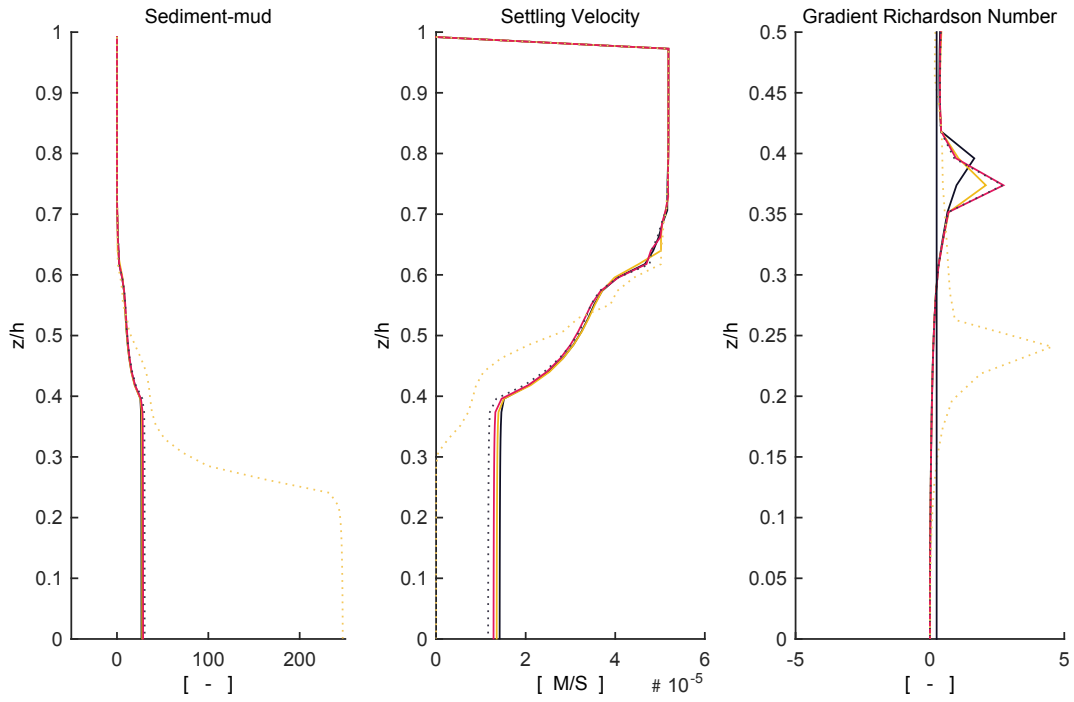
— 1.2 rho (057) — 1.1 rho (058) — rho = 1656 kg/m3 (028) 0.9 rho (059) 0.9 rho (060)

DISCHARGE BOUNDARY ANALYSIS at x=7850m

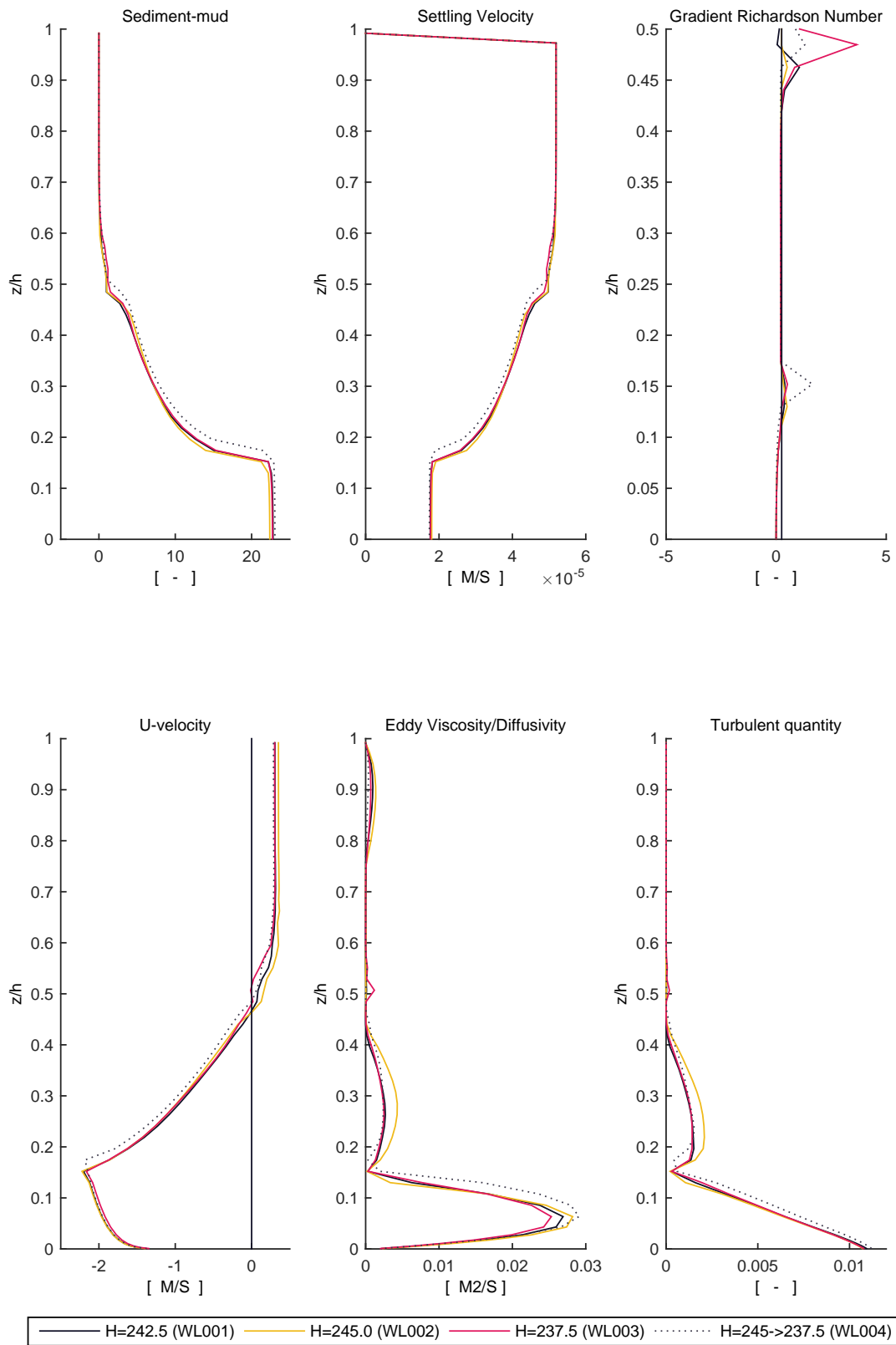


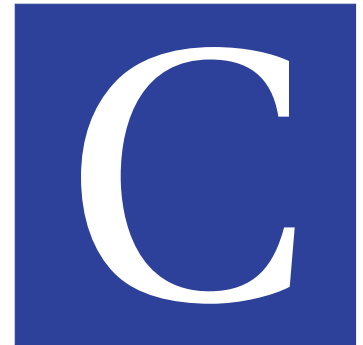
— 1.050 q (062) — 1.025 q (061) — q = 20 m2/s (028) 0.975 q (063) 0.950 q (064)

CONCENTRATION BOUNDARY ANALYSIS at x=7850m



BOUNDARY WATER LEVEL CONDITION at x=7850m





Results Soulik (2013)

Typhoon Soulik (2013) modelling results are presented here. These correspond to chapter 5.

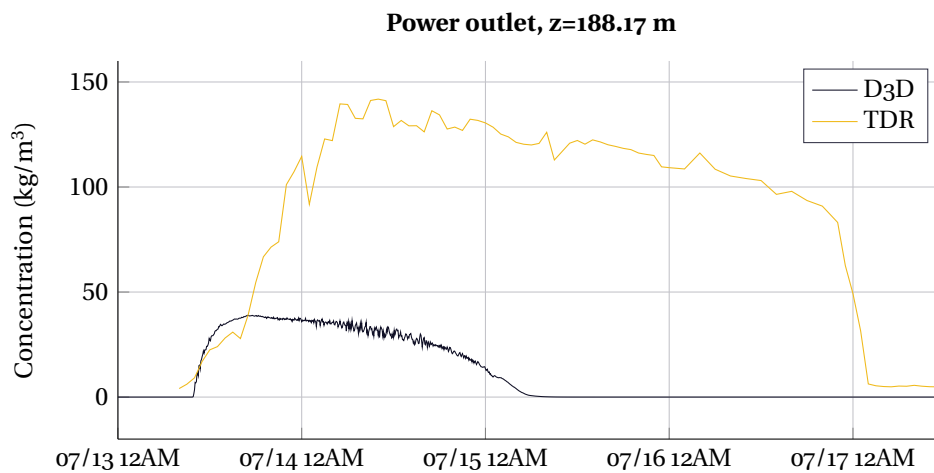


Figure C.1: TDR SSC versus SSC at the Power Plant out-take

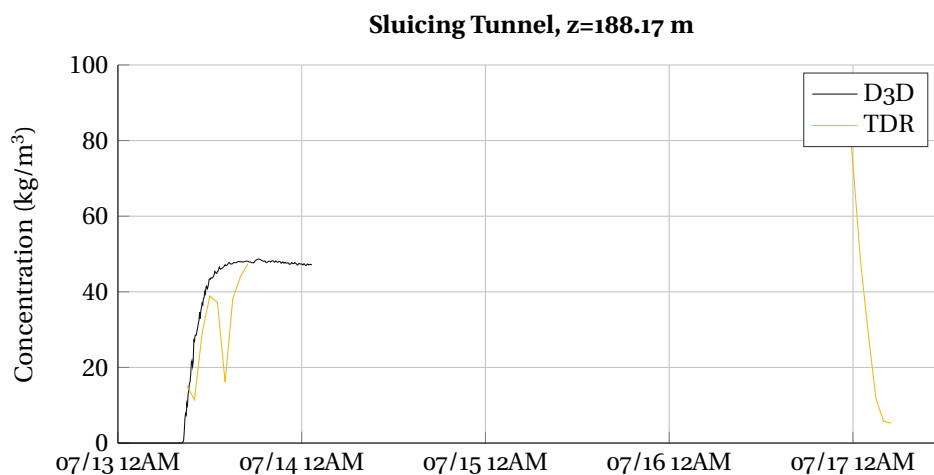


Figure C.2: TDR SSC versus SSC at the Sluicing Tunnel

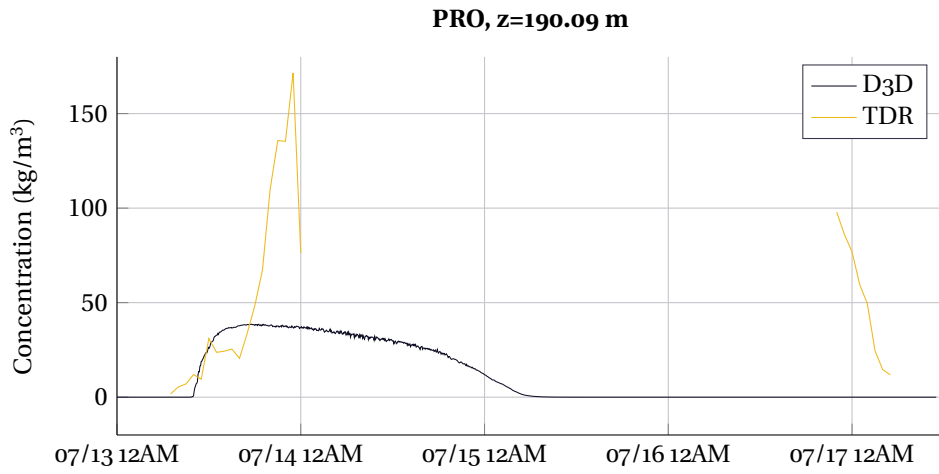


Figure C.3: TDR SSC versus SSC at the PRO

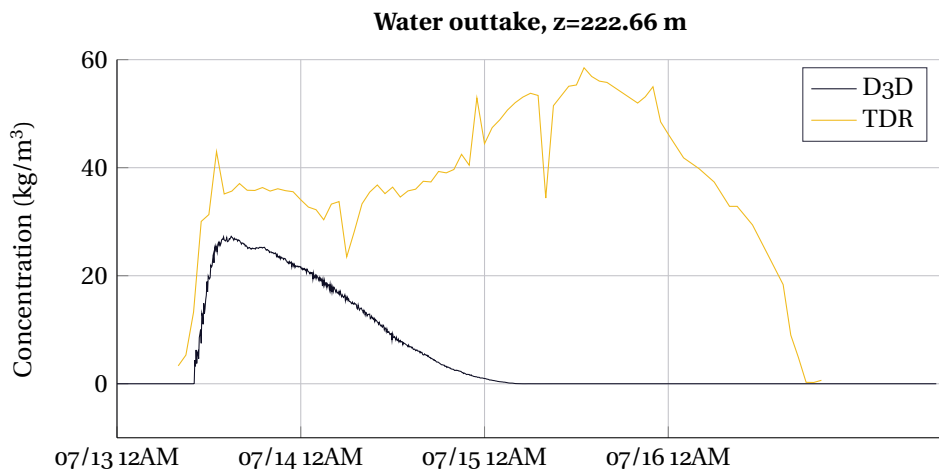


Figure C.4: TDR SSC versus SSC at the water out-take

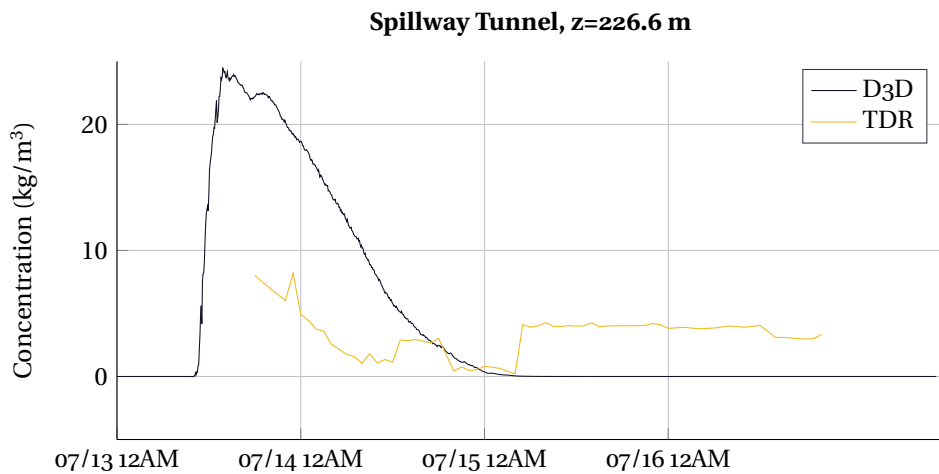


Figure C.5: TDR SSC versus SSC at the Tunnel Spillway

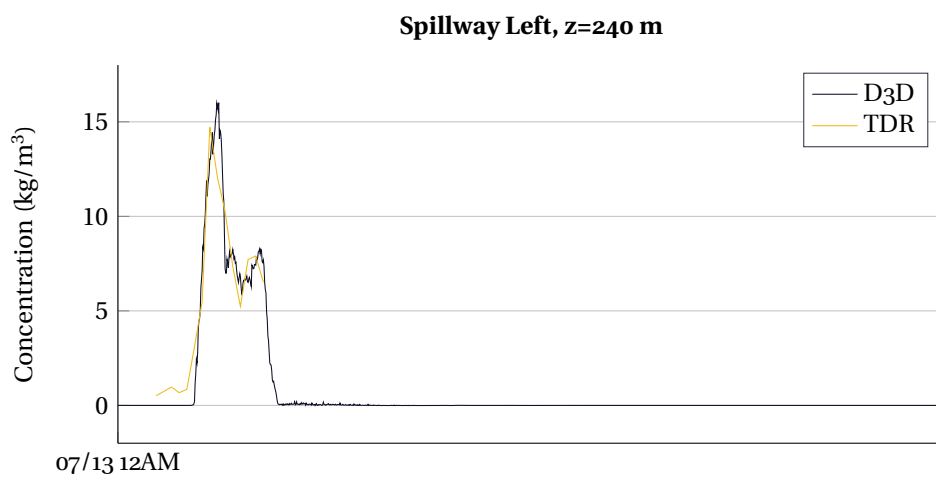


Figure C.6: TDR SSC versus SSC at the Spillway (left)

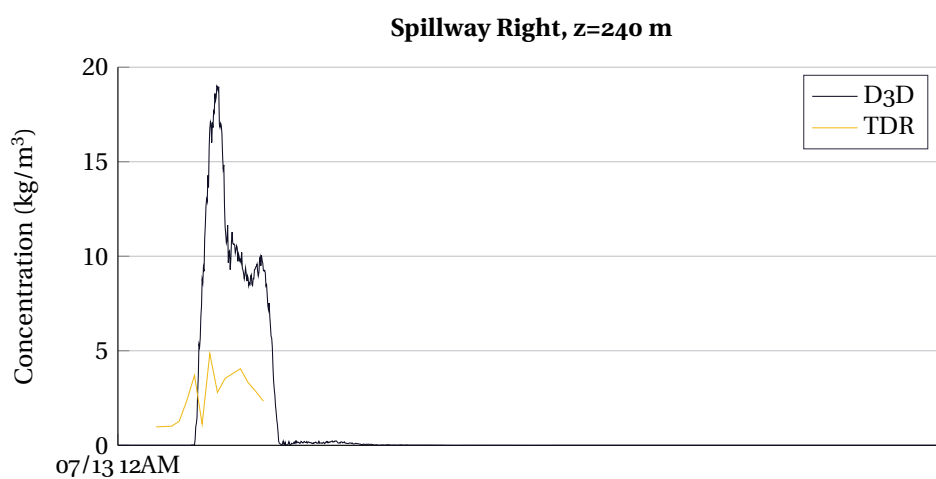


Figure C.7: TDR SSC versus SSC at the Spillway (right)

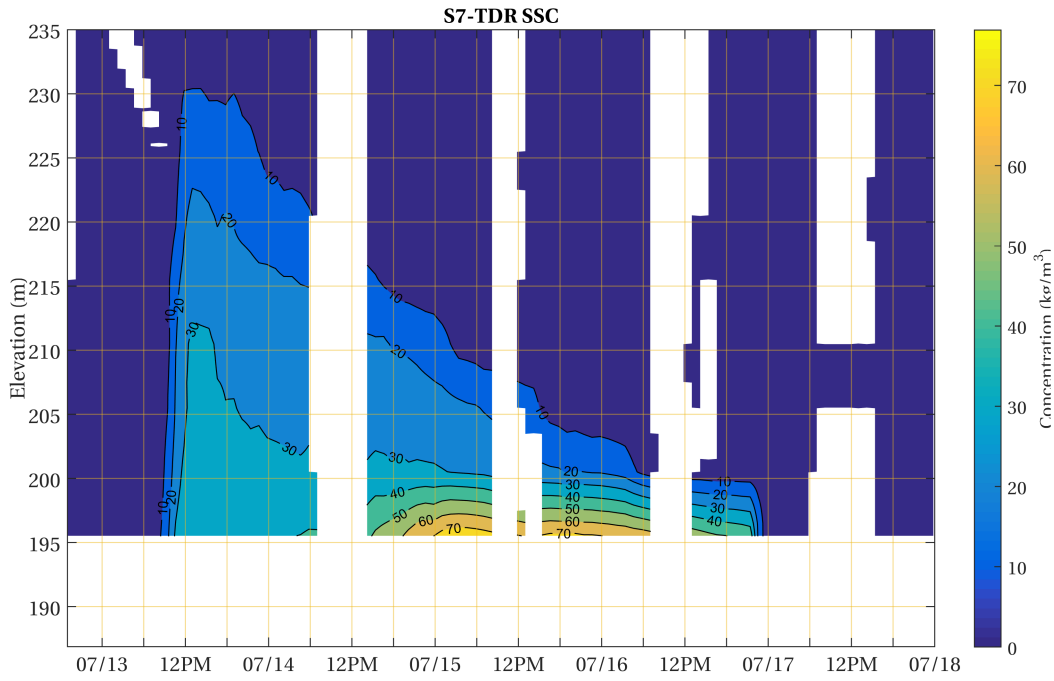


Figure C.8: Measured SSC from the TDR at cross-section 7.

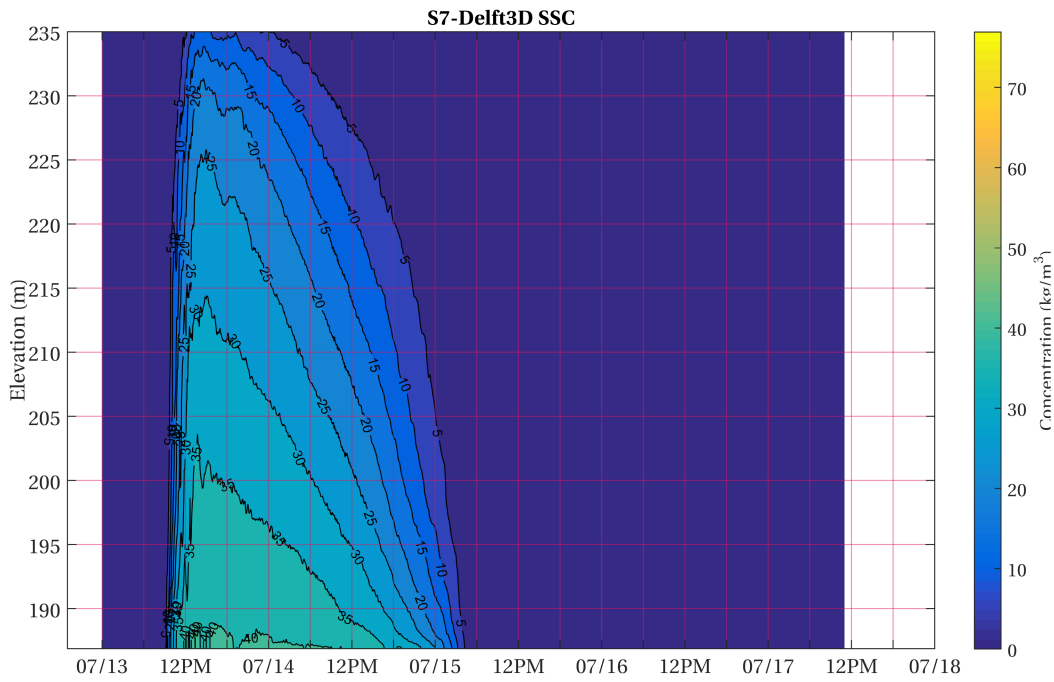


Figure C.9: Simulated SSC by at cross-section 7.

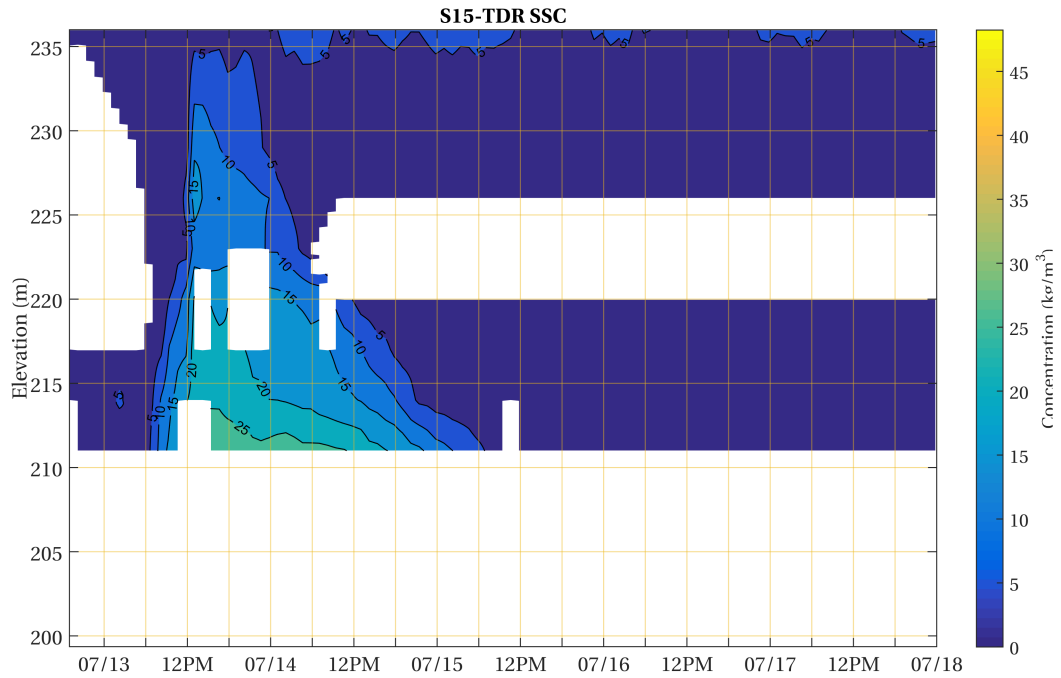


Figure C.10: Measured SSC from the TDR at cross-section 15.

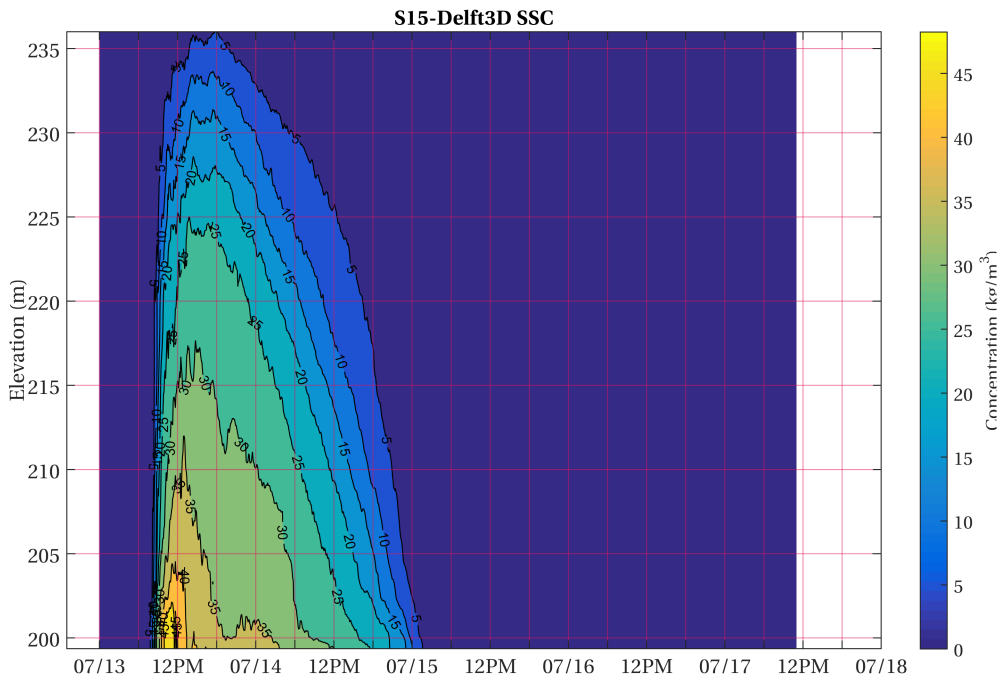


Figure C.11: Simulated SSC by at cross-section 15.

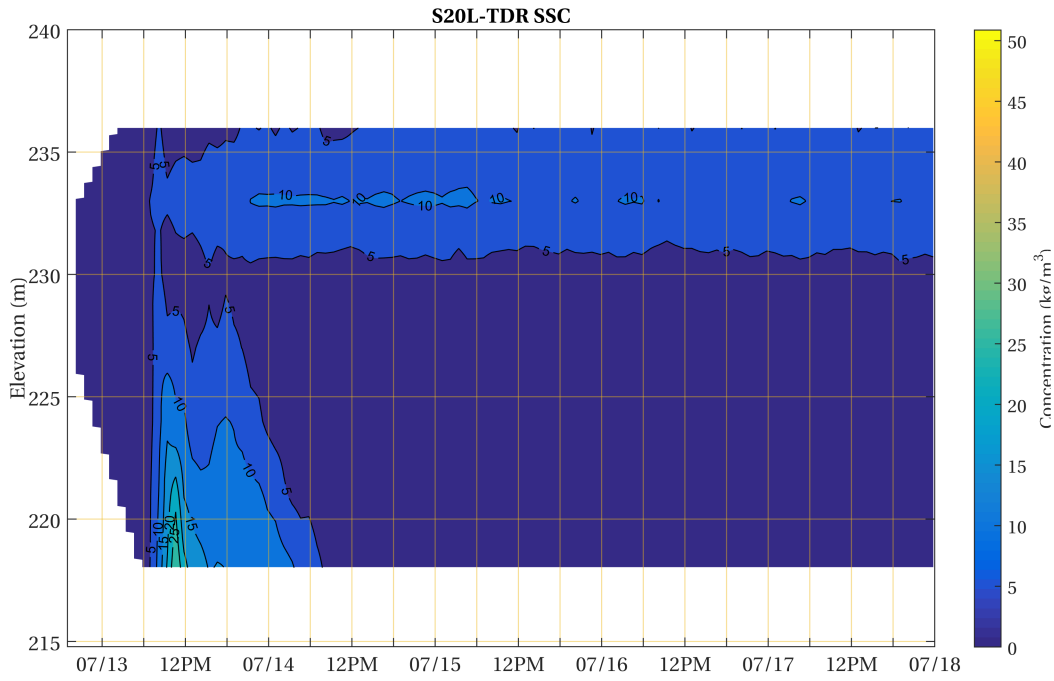


Figure C.12: Measured SSC from the TDR at cross-section 20 (left).

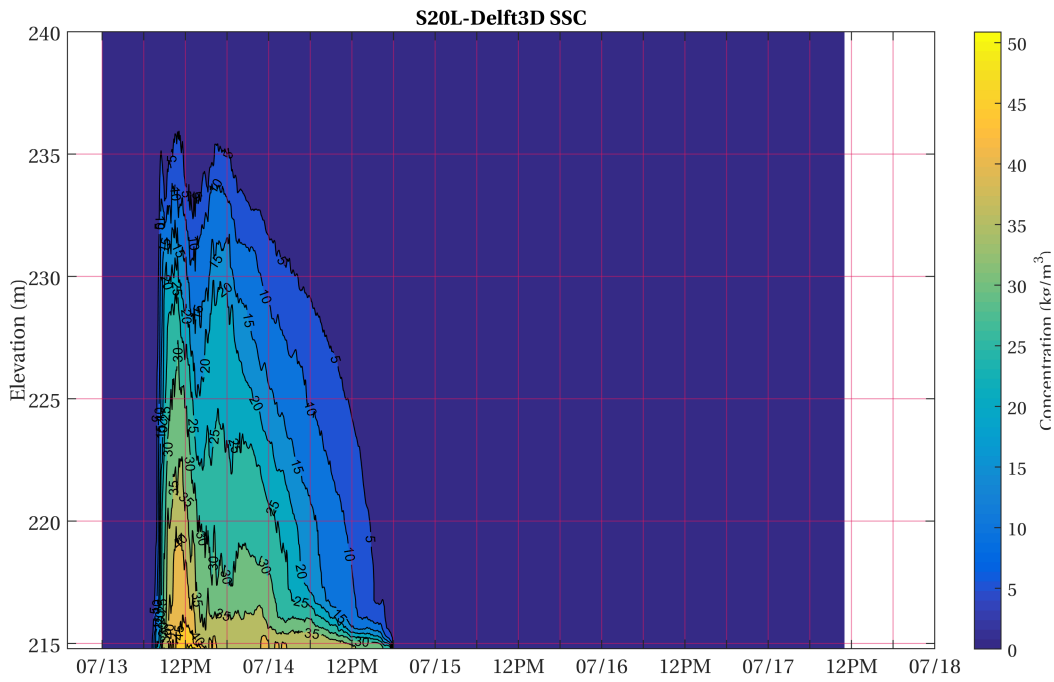


Figure C.13: Simulated SSC by at cross-section 20 (left).

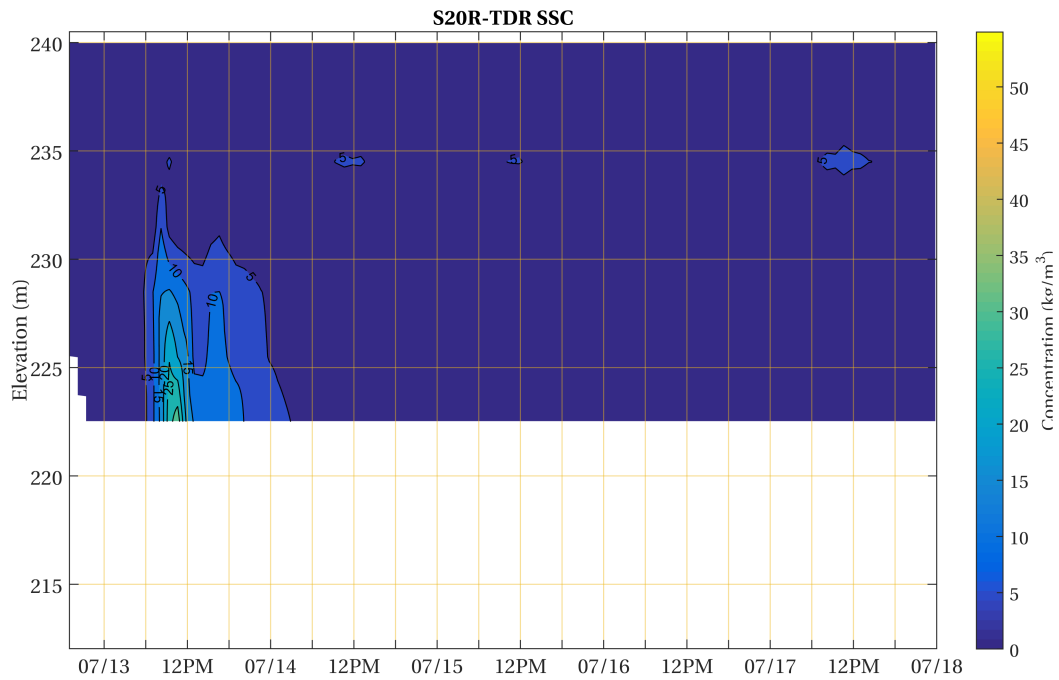


Figure C.14: Measured SSC from the TDR at cross-section 20 (right).

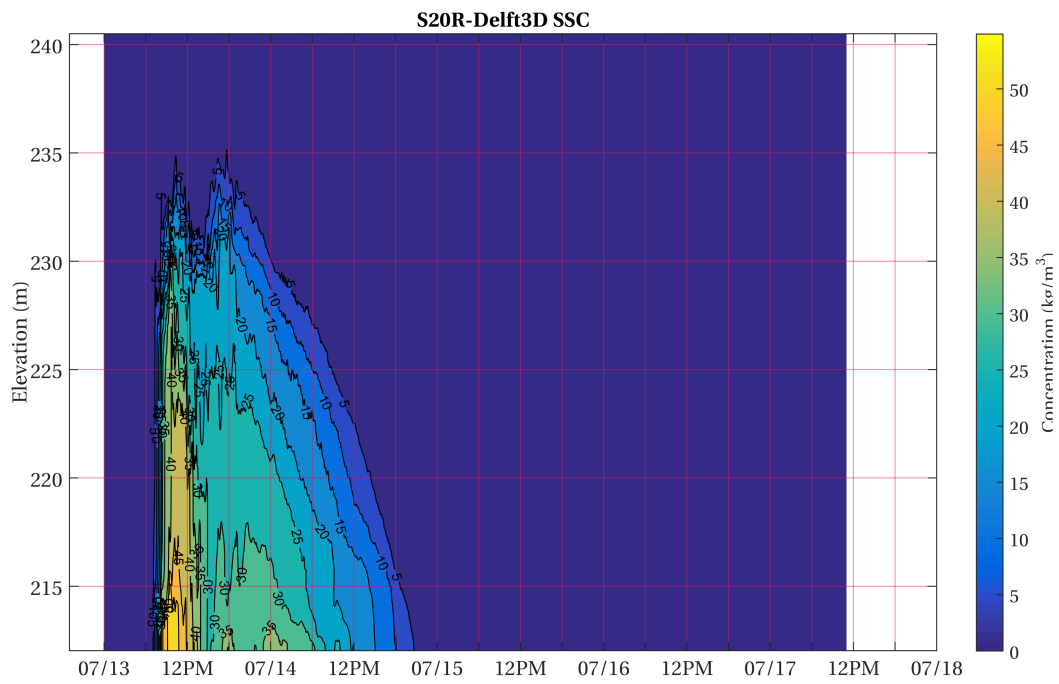


Figure C.15: Simulated SSC by at cross-section 20 (right).

Nomenclature

Sub-, superscripts and indexes used

- $\bar{\square}$ Averaged
- $\square^{(i)}$ Sediment fraction index
- \square' Fluctuation

Roman symbols used

A	Surface	$[\text{m}^2]$
B_s	Coefficient	$[-]$
C	Coefficient	$[-]$
c	Sediment concentration	$[\text{kg m}^{-3}]$
c_{gel}	Sediment gelling concentration	$[\text{kg m}^{-3}]$
c_{in}	Sediment concentration flowing in	$[\text{kg m}^{-3}]$
c_l	Velocity of light	$[\text{m s}^{-1}]$
c_{out}	Sediment concentration flowing out	$[\text{kg m}^{-3}]$
$c_\mu, C_{1\epsilon}, C_{2\epsilon}, C_{3\epsilon}$	Coefficients for the turbulent model	$[-]$
D_c	Dissipation due to consolidation-diffusion effects	$[\text{m}^2 \text{s}^{-1}]$
D_T^{D3D}	Eddy diffusivity in Delft3D	$[\text{m}^2 \text{s}^{-1}]$
$D(c)$	Total dissipation coefficient	$[\text{m}^2 \text{s}^{-1}]$
D_m	Dissipation due to molecular effects	$[\text{m}^2 \text{s}^{-1}]$
D_T	Dissipation due to turbulence effects	$[\text{m}^2 \text{s}^{-1}]$
D_T^H	Horizontal eddy diffusivity in Delft3D	$[\text{m}^2 \text{s}^{-1}]$
$D_T^{H;back}$	Horizontal background eddy diffusivity in Delft3D	$[\text{m}^2 \text{s}^{-1}]$
D_T^V	Vertical eddy diffusivity in Delft3D	$[\text{m}^2 \text{s}^{-1}]$
$D_T^{V;back}$	Vertical background eddy diffusivity in Delft3D	$[\text{m}^2 \text{s}^{-1}]$
e_w	Entrainment coefficient	$[-]$
g	Gravitational acceleration	$[\text{m s}^{-2}]$
G_s	Specific gravity of suspended sediment	$[-]$
h	Water depth	$[\text{m}]$
k	Turbulent Kinetic Energy	$[\text{m}^2 \text{s}^{-2}]$
k_s	Nikuradse height	$[\text{mm}]$
L	Length	$[\text{m}]$
l	Largest turbulent length scale	$[\text{m}]$
L_e	Electrical length	$[\text{m}]$
L_m	Monin-Obukhov turbulent length scale	$[\text{m}]$
L_{oz}	Ozmidov length scale	$[\text{m}]$
l_t	Prandtl's mixing length	$[\text{m}]$

m	Exponent coefficient	[-]
n	Manning's roughness coefficient	$[\text{m}^{1/3}\text{s}^{-1}]$
t	Time	[s]
p	Pressure	[Pa]
p_{atm}	Atmospheric pressure	[Pa]
q	Hydrodynamic pressure	[Pa]
Q_{in}	Discharge flowing in	$[\text{m}^3\text{s}^{-1}]$
Q_{out}	Discharge flowing out	$[\text{m}^3\text{s}^{-1}]$
SS	Volumetric sediment content	[-]
T	Temperature	[°C]
t_0	Time offset for the TDR device	[s]
u	Flow velocity in x -direction	$[\text{m s}^{-1}]$
u_{plunge}	Flow velocity after plunging	$[\text{m s}^{-1}]$
u_{rms}	Root mean square of \bar{u}'	$[\text{m}^2\text{s}^{-2}]$
u_*	Friction velocity	$[\text{m s}^{-1}]$
v	Flow velocity in y -direction	$[\text{m s}^{-1}]$
V_{eff}	Venting efficiency	[-]
w	Flow velocity in z -direction	$[\text{m s}^{-1}]$
w_{imm}	Immersed weight	[kg]
w_s	Settling velocity	$[\text{m s}^{-1}]$
w_{s0}	Settling velocity of a single particle	$[\text{m s}^{-1}]$
w_{sh}	Hindered settling velocity	$[\text{m s}^{-1}]$
W_{sk}	Total settling velocity function	$[\text{m s}^{-1}]$
x	Horizontal coordinate	[m]
x_{plunge}	Plunge point location	[m]
y	Horizontal coordinate	[m]
z	Vertical coordinate	[m]
z_0	Roughness height	[m]
z_{bot}	Fixed lowest elevation for z -grid	[m]
z_{top}	Fixed highest elevation for z -grid	[m]

Greek symbols used

α	Angle	[rad]
δ_{ij}	Kronecker delta	[-]
δ_l	Viscous boundary layer thickness	[m]
ω_j	Planetary vorticity	$[\text{rad s}^{-1}]$
Δt	Time step	[s]
$\Delta \tau$	TDR travel time	[s]
Δx	Grid size	[m]
ϵ_a	Apparent dielectric constant	[-]
ϵ_{ijk}	Cyclic permutation symbol	[-]
ϵ_{ss}	Dielectric constant of suspended sediment	[-]

ϵ_w	Dielectric constant of water	[-]
κ	Von Kármán constant	[-]
Φ	Sediment flux or density function ($\Phi = w_s c$)	[m s ⁻¹]
ϕ	Volumetric concentration of flocs ($\phi = (\rho_s - \rho)/(\rho_f - \rho)$)	[-]
ρ	Specific density of the fluid	[kg m ⁻³]
ρ_0	Reference density	[kg m ⁻³]
ρ_f	Density of floc	[kg m ⁻³]
ρ_0	Specific density of sediment	[kg m ⁻³]
ρ_w	Specific density of water	[kg m ⁻³]
σ'	Effective stress	[Pa]
σ	Normalised vertical coordinate in σ -grid	[-]
$\sigma_k, \sigma_\epsilon, \sigma_{SC}$	Turbulent Prandtl-Schmidt numbers	[-]
τ, τ_{ij}	Shear stress	[N m ⁻²]
τ_b	Shear stress at the bed	[N m ⁻²]
τ_{turb}	Turbulent shear stress	[N m ⁻²]
τ_{visc}	Viscous shear stress	[N m ⁻²]
μ	Dynamic viscosity of the fluid	[Pa s]
ν	Kinematic viscosity of the fluid	[m ² s ⁻¹]
ν_T	Turbulent eddy viscosity	[m ² s ⁻¹]
ν_T^H	Horizontal eddy viscosity in Delft3D	[m ² s ⁻¹]
$\nu_T^{H;back}$	Horizontal background eddy viscosity in Delft3D	[m ² s ⁻¹]
ν_T^V	Vertical eddy viscosity in Delft3D	[m ² s ⁻¹]
$\nu_T^{V;back}$	Vertical background eddy viscosity in Delft3D	[m ² s ⁻¹]
γ	Shear strain	[-]

Dimensionless numbers used

Re	Reynolds number	[-]
Re _*	Turbulent Reynolds number ($Re_* = \sqrt{k}l/\nu$)	[-]
Ri	Bulk Richardson number	[-]
Ri _g	Gradient Richardson number	[-]

Acronyms

2DV two-dimensional vertical

3D three-dimensional

DNS Direct Numerical Solving

DPWE Disaster Prevention & Water Environment Research Center

NCTU National Chiao Tung University

NTU Nephelometric Turbidity Unit

PRO permanent river outlet

RANS Reynolds averaged Navier-Stokes

RQ research question

SSC suspended sediment concentrations

TDR time domain reflectometry

TKE Turbulent Kinetic Energy

References

- Akiyama, J., & Stefan, H. G. (1984, April). Plunging Flow into a Reservoir: Theory. *Journal of Hydraulic Engineering*, 110(4), 484–499.
- Altinakar, M., Graf, W., & Hopfinger, E. (1996, September). Flow structure in turbidity currents. *Journal of Hydraulic Research*, 34(5), 713–718.
- Bell, H. (1942). *Stratified flow in reservoirs and its use in prevention of silting*.
- Britter, R. E., & Linden, P. F. (1980, April). The motion of the front of a gravity current travelling down an incline. *Journal of Fluid Mechanics*, 99(3), 531–543.
- Camenen, B., & van Bang, D. P. (2011). Modelling the settling of suspended sediments for concentrations close to the gelling concentration. *Continental Shelf Research*, 31(10 SUPPL.), S106–S116.
- Chung, C.-C., & Lin, C.-P. (2011, April). High concentration suspended sediment measurements using time domain reflectometry. *Journal of Hydrology*, 401(1-2), 134–144.
- Daly, R. (1936). Origin of submarine canyons. *American Journal of Science*, 186(6), 401–420.
- Dankers, P. J. T. (2006). On the hindered settling of suspensions of mud and mud-sand mixtures.
- Dankers, P. J. T., & Winterwerp, J. (2007). Hindered settling of mud flocs: Theory and validation. *Continental Shelf Research*, 27(14), 1893–1907.
- Deltares. (2014). *Delft3D Hydro-morphodynamics; user manual version: 3.15*. Delft, The Netherlands: Author.
- Ehlschlaeger, C. (1989). Using the AT Search Algorithm to Develop Hydrologic Models from Digital Elevation Data. *Proceedings of International Geographic Information Systems (IGIS), Symposium*, 275–281.
- Ellison, T., & Turner, J. (1959). Turbulent entrainment in stratified flows. *Journal of Fluid Mechanics*(February).
- Forel, F. A. (1880). L'Echo des Alpes. *La congelation des lacs Suisses et savoyards pendant l'hiver, 1879-1880*(3), 149–161.
- Forel, F. A. (1885). Les Ravins Sous-lacustres de Fleuves Glaciaires. *Comptes Rendus, Academie de Sciences, Paris*, 101, 725–728.
- García, M. (1993). Hydraulic jumps in sediment-driven bottom currents. *Journal of Hydraulic Engineering*, 119(10), 1094–1117.
- Gould, H. (1951). Some quantitative aspects of Lake Mead turbidity currents. *Society of Economic Paleontologists and Mineralogists*(2), 34–52.
- Grover, N. C., & Howard, C. S. (1938). The Passage of Turbid Water through Lake Mead. *Transactions of the American Society of Civil Engineers*, 103(1), 720–781.
- Hartel, C., Carlsson, F., & Thunblom, M. (2000). Analysis and direct numerical simulation of the flow at a gravity-current head. Part 2. The lobe-and-cleft instability. *Journal of Fluid Mechanics*, 418, 213–229.

- Härtel, C., Meiburg, E., & Necker, F. (2000). Analysis and direct numerical simulation of the flow at a gravity-current head. Part 1. Flow topology and front speed for slip and no-slip boundaries. *Journal of Fluid Mechanics*, 418, 189–212.
- Heezen, B., & Ewing, W. (1952). Turbidity currents and submarine slumps, and the 1929 Grand Banks earthquake. *American Journal of Science*, 250(12), 849–873.
- Hsu, P. (2013). The Development of A Sustainable Shihmen Reservoir. GT International.
- Johnson, D. (1939). The Origin of Submarine Canyons. A Critical Review of Hypotheses. *Columbia University Press*.
- Kneller, B., Bennett, S., & McCaffrey, W. (1999). Velocity structure, turbulence and fluid stresses in experimental gravity currents. *Journal of Geophysical Research*, 104, 5281–5291.
- Kneller, B., & Buckee, C. (2000). The structure and fluid mechanics of turbidity currents: a review of some recent studies and their geological implications. *Sedimentology*, 47, 62–94.
- Kranenburg, C. (1992). *Hindered settling and consolidation of mud* (Tech. Rep.). Delft, The Netherlands: Delft University of Technology, Department of Civil Engineering, Hydromechanics Section.
- Kuenen, P. (1938). Density currents in connection with the problem of submarine canyons. *Geological Magazine*, LXXV(VI).
- Kynch, G. J. (1952). A theory of sedimentation. *Transactions of the Faraday Society*, 48, 166.
- Lesser, G., Roelvink, J., van Kester, J. T. M., & Stelling, G. (2004). Development of a three-dimensional morphological model. *Coastal Engineering*, 51, 883–915.
- Liggett, J. A. (1994). *Fluid Mechanics*. McGraw-Hill.
- Mehta, A. J. (2014). *An Introduction to Hydraulics of Fine Sediment Transport*. World Scientific Publishing Co. Pte. Ltd.
- Meiburg, E., & Kneller, B. (2010, January). Turbidity Currents and Their Deposits. *Annual Review of Fluid Mechanics*, 42(1), 135–156.
- Merckelbach, L., & Kranenburg, C. (2004). Determining effective stress and permeability equations for soft mud from simple laboratory experiments. *Géotechnique*, 54(9), 581–591.
- Middleton, G. V. (1993). Sediment deposition from turbidity currents. *Annual Review of Earth and Planetary Sciences*, 21, 89–114.
- Morris, G. L., & Fan, J. (1998). *Reservoir sedimentation handbook*. New York: McGraw-Hill Book Co.
- Nasr-Azadani, M., & Meiburg, E. (2011, June). TURBINS: an immersed boundary, Navier-Stokes code for the simulation of gravity and turbidity currents interacting with complex topographies. *Computers & Fluids*, 45(1), 14–28.
- Parker, G. (2007). *Turbidity currents: Morphodynamics and deposits*.
- Parker, G., Garcia, M., Fukushima, Y., & Yu, W. (1987). Experiments on turbidity currents over an erodible bed. *Journal of Hydraulic Research*, 25(1), 123–147.
- Prandtl, L. (1952). *Essentials of Fluid Dynamics*. Hefner.

- Richardson, J., & Zaki, W. (1954). Sedimentation and fluidisation: Part I. *Trans. Inst. Chem. Eng.*, 32, 35–53.
- Rodi, W. (1984). *Turbulence models and their applications in hydraulics - a state-of-the-art review*. Delft, The Netherlands: IAHR monograph.
- Simonin, O., Uittenbogaard, R., Baron, F., & Viollet, P. (1989). Possibilities and limitations of the k-eps model to simulate turbulent fluxes of mass and momentum, measured in a steady, stratified mixing layer. In *Xxiii bi-annual congress* (pp. A55–A62).
- Simpson, J. (1997). *Gravity Currents second ed.*
- Simpson, J., & Britter, R. (1979). The dynamics of the head of a gravity current advancing over a horizontal surface. *Journal of Fluid Mechanics*, 94.
- Sloff, C. J. (1997). *Sedimentation of Reservoirs* (No. 97).
- Slørdal, L. H. v. (1997). The Pressure Gradient Force in Sigma-co-ordinate ocean models. *International journal for numerical methods in fluids*, 24(10), 987–1017.
- Toorman, E. A. (1996). Sedimentation and self-weight consolidation: general unifying theory. *Géotechnique*, 46(Volume 46, Issue 1), 103–113(10).
- Turner, J. (1973). *Buoyancy Effects in Fluids*.
- Uittenbogaard, R., & van Kester, J. T. M. (1992). *Implementation of three turbulence models in TRISULA for rectangular horizontal grids, including 2DV test cases* (Tech. Rep.). Delft, The Netherlands: Delft Hydraulics.
- Winterwerp, J. (1999). *On the dynamics of high-concentrated mud suspensions* (Tech. Rep.). Delft, The Netherlands: Delft University of Technology.
- Winterwerp, J. (2006). Stratification effects by fine suspended sediment at low, medium, and very high concentrations. *Journal of Geophysical Research*., 111(C5), C05012.
- Winterwerp, J., & van Kesteren, W. G. (2004). *Introduction to the Physics of Cohesive Sediment in the Marine Environment*. Elsevier.
- Wu, M. (2009). *The study on the clay of reservoir in Taiwan* (Tech. Rep.).
- Xu, J., Sequeiros, O. E., & Noble, M. a. (2014, July). Sediment concentrations, flow conditions, and downstream evolution of two turbidity currents, Monterey Canyon, USA. *Deep Sea Research Part I: Oceanographic Research Papers*, 89, 11–34.
- Yang, J.-C., Huang, A., Tsai, T.-L., & Chang, Y.-L. (2008). *A study on risk assessment of landslide and sediment deposition in Shihmen watershed* (Tech. Rep.). Hsinchu, Taiwan: DPWE.
- Yang, J.-C., Lin, C.-P., Hsu, Y.-C., Chung, C.-C., & Chang, Y.-L. (2014). *Taiwan's Shihmen Reservoir Restoration Framework* (Vol. 3).